

PL-TR-97-2162

SPACE SYSTEM ENVIRONMENT INTERACTIONS INVESTIGATION

**M. J. Mandell
G. A. Jongeward
R. A. Kuharski
V. A. Davis**

**Maxwell Federal Division, Inc.
Maxwell Technologies
8888 Balboa Avenue
San Diego, California 92123-1506**

December 1997

DTIC QUALITY INSPECTED 4

Scientific Report No. 2

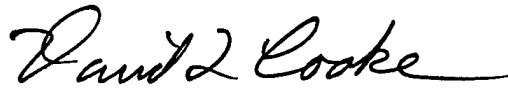
Approved for Public Release; Distribution Unlimited.



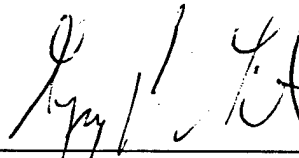
**AIR FORCE RESEARCH LABORATORY
Space Vehicles Directorate
29 Randolph Road
AIR FORCE MATERIEL COMMAND
HANSCOM AFB, MA 01731-3010**

1 9 9 9 0 2 1 9 0 7 9

"This technical report has been reviewed and is approved for publication"



DAVID L. COOKE
Contract Manager



GREG P. GINET
Branch Chief



DAVID A. HARDY
Division Director

This report has been reviewed by the ESC Public Affairs Office (PA) and is releasable to the National Technical Information Service (NTIS).

Qualified requestors may obtain additional copies from the Defense Technical Information Center (DTIC). All others should apply to the National Technical Information Service (NTIS).

If your address has changed, if you wish to be removed from the mailing list, or if the addressee is no longer employed by your organization, please notify AFRL/VSOS-IM, 29 Randolph Road, Hanscom AFB, MA 01731-3010. This will assist us in maintaining a current mailing list.

Do not return copies of this report unless contractual obligations or notices on a specific document requires that it be returned.

REPORT DOCUMENTATION PAGE			<i>Form Approved</i> OMB No. 0704-0188	
Public reporting burden for this collection of information is estimated to average 1 hour per response, including the time for reviewing instructions, searching existing data sources, gathering and maintaining the data needed, and completing and reviewing the collection of information. Send comments regarding this burden estimate or any other aspect of this collection of information, including suggestions for reducing this burden, to Washington Headquarters Services, Directorate for Information Operations and Reports, 1215 Jefferson Davis Highway, Suite 1204, Arlington VA 22202-4302, and to the Office of Management and Budget, Paperwork Reduction Project (0704-0188), Washington, DC 20503.				
1. AGENCY USE ONLY (Leave blank)		2. REPORT DATE December 1997	3. REPORT TYPE AND DATES COVERED Scientific Report No. 2	
4. TITLE AND SUBTITLE Space System-Environment Interactions Investigation			5. FUNDING NUMBERS PE 63410F PR S327 TA 01 WU AA F19628-91-C-0187	
6. AUTHOR(S) M. J. Mandell, G. A. Jongeward, R. A. Kuharski, V. A. Davis				
7. PERFORMING ORGANIZATION NAME(S) AND ADDRESS(ES) Maxwell Federal Division, Inc. Maxwell Technologies 8888 Balboa Avenue San Diego, California 92123-1506			8. PERFORMING ORGANIZATION REPORT NUMBER MFD-DTR-97-15961	
9. SPONSORING/MONITORING AGENCY NAME(S) AND ADDRESS(ES) Air Force Research Laboratory 29 Randolph Road Hanscom AFB, MA 01731-3010 Contract Manager: David Cooke/GPSG			10. SPONSORING/MONITORING AGENCY REPORT NUMBER PL-TR-97-2162	
11. SUPPLEMENTARY NOTES				
12a. DISTRIBUTION/AVAILABILITY STATEMENT Approved for public release; distribution unlimited.			12b. DISTRIBUTION CODE	
13. ABSTRACT (Maximum 200 words) This report describes work conducted to support research into the interactions of space systems with the space environment. This report covers theoretical and calculational research in support of the SPEAR 3 program using the EPSAT and DynaPAC computer codes. Analysis of CHAWS and PASP Plus flight data is discussed.				
14. SUBJECT TERMS Spacecraft, Space Environment, SPEAR, EPSAT, DynaPAC, CHAWS, PASP Plus, Solar Arrays, Wakes, Parasitic Current Collection			15. NUMBER OF PAGES 106	
			16. PRICE CODE	
17. SECURITY CLASSIFICATION OF REPORT UNCLASSIFIED	18. SECURITY CLASSIFICATION OF THIS PAGE UNCLASSIFIED	19. SECURITY CLASSIFICATION OF ABSTRACT UNCLASSIFIED	20. LIMITATION OF ABSTRACT SAR	

TABLE OF CONTENTS

Section	Page
1. Introduction	1
2. EPSAT Calculations in Support of Maintaining a High Apogee for SPEAR-3	4
3. DynaPAC Calculations for SPEAR-3 Floating Potentials and Currents	7
4. DynaPAC Calculations for ESA Currents and Angles.....	14
5. Neutral Densities Produced by the NGRS (Neutral Gas Release System).....	21
6. NGRS-Induced Breakdown of the SPEAR-3 Negative Body Sheath	27
6.1 Three-Dimensional Considerations	27
6.2 Two-Dimensional Breakdown Calculation.....	32
6.3 Continuous Slowing Down Approximation.....	37
7. SPEAR-3 Mockup Analysis - Floating Potential	42
7.1 Plasma Differences	44
7.2 Chamber Size Effects.....	46
7.3 Ionization Effects.....	47
7.4 Sheath Breakdown.....	47
7.5 Breakdown Quenching by the Disruptor Plate.....	50
8. Statistical Analysis of CHAWS data	52
8.1 Relevant Parameters.....	52
8.2 Parameters Available From Models.....	53
8.3 Measured Quantities	59
8.4 Derived Parameters.....	73

TABLE OF CONTENTS (continued)

Section	Page
8.5 Current Measurements	74
8.6 Fitting.....	86
8.7 Comparison with Calculation.....	91
8.8 Probe in Ram Measurements	92
8.9 WSF in Shuttle Wake.....	93
8.10 Additional Material.....	94
9. References	100

1. INTRODUCTION

This report is a summary of technical work performed from inception (December 1991) through November 1997 on Contract F19628-91-C-0187 titled "Space System-Environment Interactions Investigation." It is the twelveth of a series of interim reports produced every six months, and is published as Scientific Report #2. Each report includes an update of the material of the previous report, deleting obsolete material, and adding the work performed during the two most recent quarters. In that way, a single volume always suffices as a technical summary of the work.

The objectives of this contract are to support, with theoretical and modeling studies, research into the interactions of space systems with the space environment that are of interest to the Air Force. During this period work was performed in support of the SPEAR-III rocket flight experiment, the PASP Plus orbital experiment, the CHAWS shuttle experiment, and the SPREE shuttle experiment.

SPEAR III

Dr. Myron J. Mandell and Dr. Gary A. Jongeward made presentations at the following conferences and SPEAR-III project meetings:

Meeting Name	Location	Date
Science Meeting	Arlington, VA	17-18 December 1991
Mid-Point Review	Logan, UT	14-16 January 1992
CDR	Logan, UT	14-16 April 1992
Science Meeting	Sandusky, OH	9-10 July 1992
Mock-up Data Review	Arlington, VA	2 September 1992
AGU Fall 1992	San Francisco, CA	7-11 December 1992
High Voltage Workshop	Dayton, OH	20-21 October 1992
SPEAR-III Data Review	Logan, UT	20-21 April 1993
IEEE Plasma Physics	Vancouver, B.C.	7-9 June 1993

In addition, SPEAR-III information was exchanged by telephone and telefax. The presentations at these meetings, along with some telephone and telefax information, have been reorganized into chapters titled:

2. EPSAT Calculations in Support of Maintaining a High Apogee for SPEAR-III.
3. DynaPAC Calculations for SPEAR-III Floating Potentials and Currents.
4. DynaPAC Calculations for ESA Currents and Angles
5. Neutral Densities Produced by the NGRS (Neutral Gas Release System)
6. NGRS-Induced Breakdown of the SPEAR-III Negative Body Sheath
7. Modeling of SPEAR III Mock-up.

The quarterly reports for this contract contain the actual presentation material.

A review of our examination of the SPEAR-III flight data has been accepted for publication by the *Journal of Geophysical Research*.

CHAWS

We did a statistical analysis of CHAWS data from the flights of the Wake Shield Facility (WSF). The analysis is described in Chapter 8 of this report.

We did a preliminary calculation of the current collected by CHAWS while WSF was in the wake of the shuttle. This involved making a geometric model of the WSF and shuttle system.

We made a presentation on comparing calculations with experiment values of the wake side currents from the CHAWS experiment at the Spring AGU meeting in May 1996.

The presentation is included in the quarterly report for the appropriate period.

We will submit a paper summarizing our analysis of the CHAWS flight experiment and our simulations to the *Journal of Geophysical Research*.

SPREE

We made a geometric model of SPREE in the shuttle bay. We did reverse trajectory calculations with and without the stowed TSS sphere.

PASP Plus

We presented the paper "Parasitic Collection by PASP-Plus Solar Arrays" at the Space Photovoltaic Research and Technology 1995 Conference. The paper prepared for this conference is Reference 4.

Our paper "Modeling of Parasitic Current Collection by Solar Arrays in Low Earth Orbit" appeared in *Physics of Plasmas*, Reference 5.

We made a presentation at the Space Power Workshop in Manhattan Beach, CA. The presentation is included in the quarterly report for the appropriate period.

We wrote a paper on PASP Plus current collection flight data for presentation at the 31st Intersociety Energy Conversion Engineering Conference in August. This paper appears as Reference 6. A revised version of the paper has been accepted for publication in February 1998 by *IEEE Transactions on Plasma Science*.

We completed our examination of the PASP Plus flight data. The details will appear as Chapter 6 of the PASP Plus Final Report to be published by Phillips Laboratory.

PUBLICATIONS

Several publications have been supported by this contract. The Maxwell contribution to the SPEAR-II products report received its final set of revisions under this contract, and appeared in Reference 1. A paper based on a presentation on the DynaPAC computer code at the DNA Numerical Methods Symposium (Menlo Park, April 1992) was published in the conference proceedings, Reference 2. A paper describing our review of the SPEAR III flight data was prepared for the AIAA Aerospace Sciences Meeting in Reno, Nevada and appears as Reference 3. A paper on our review of the SPEAR-3 flight data will appear in *the Journal of Geophysical Research*, Reference 7.

A paper describing our preliminary review of the PASP Plus data and included in the SPRAT XIV Conference, Reference 4. The paper "Modeling of Parasitic Current Collection by Solar Arrays in Low Earth Orbit" appeared in *Physics of Plasmas*, Reference 5. We wrote a paper on PASP Plus current collection flight data for presentation at the 31st Intersociety Energy Conversion Engineering Conference in August. This paper appeared in the conference proceedings, Reference 6. Our describing our analysis of the PASP Plus flight has been accepted for publication in February 1998 by *IEEE Transactions on Plasma Science*, Reference 8. A more complete description of this work will appear in the Phillips Laboratory PASP Plus Final Report.

We will submit a paper summarizing our analysis of the CHAWS flight data and our simulations to the *Journal of Geophysical Research*, Reference 9.

2. EPSAT CALCULATIONS IN SUPPORT OF MAINTAINING A HIGH APOGEE FOR SPEAR-3

In January 1992, as the SPEAR-3 payload had grown in length and weight, concern was expressed that its apogee would fall well below the desired 300 km altitude. A presentation based on EPSAT calculations was given, showing that the mission objectives would be severely impacted should the apogee fall well below 300 km.

Figure 1 shows the trajectories for 250, 300, and 350 km apogees, assuming rocket burnout at about 125 km. As the apogee drops, the time above a given altitude decreases. The figure indicates that the time above 200 km is 200, 280, and 350 seconds for the three orbits.

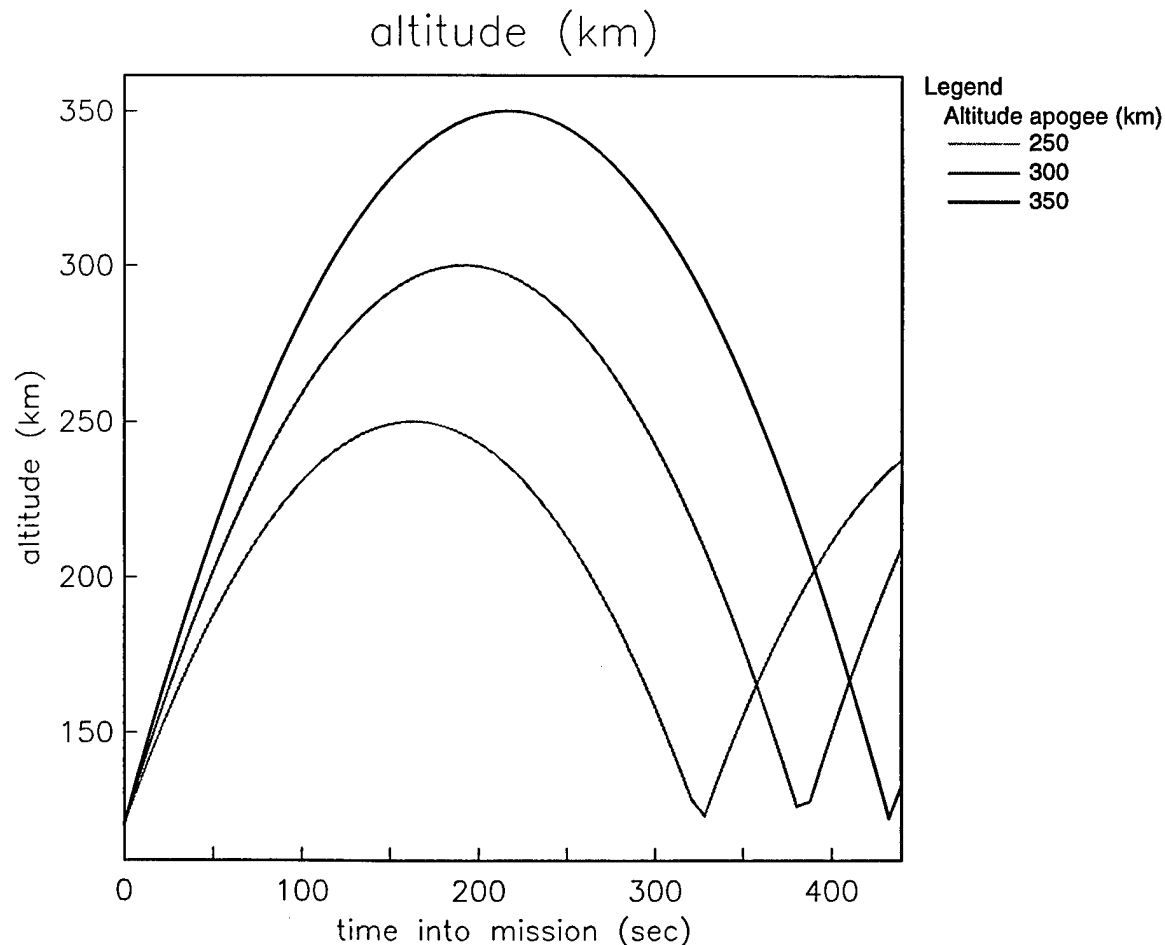


Figure 1. SPEAR-3 trajectories for 250, 300, and 350 km apogee missions.

Figure 2 shows the IRI model plasma density for the same three orbits. For the 300 and 350 km orbits there is an extended period of roughly constant plasma density. For the 250 km orbit the peak density is never reached, the plasma density is usually varying fairly rapidly, and the higher plasma densities occur early in the flight, when outgassing may not be complete.

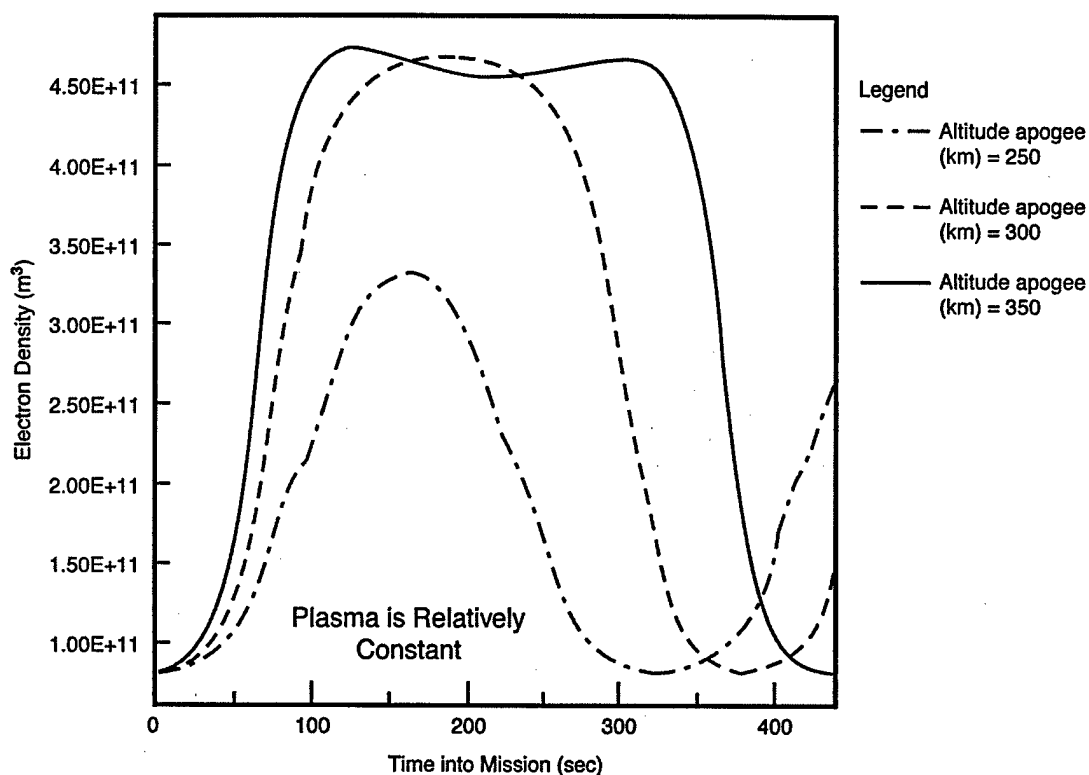


Figure 2. IRI model plasma density profiles for three SPEAR-3 orbits.

It is important to reach a high plasma density to avoid spontaneous breakdown. Figure 3 shows that the sheath radii about the sphere and the rocket increase sharply below 200 km, increasing ionization paths and enhancing the likelihood of spontaneous breakdown.

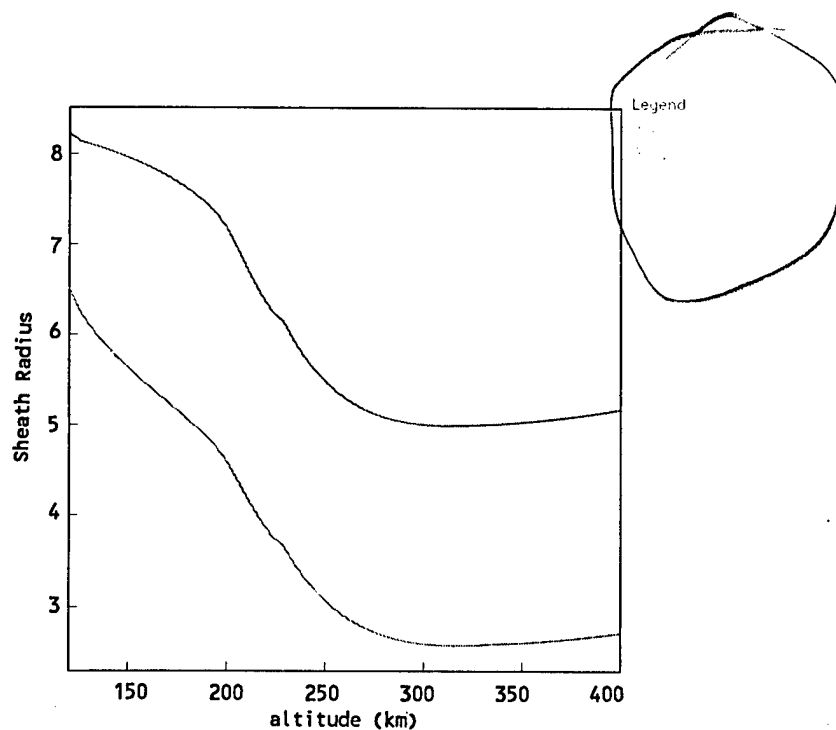


Figure 3. Sheath radii about the SPEAR-3 sphere and body, calculated using IRI predicted plasma density at specified altitude.

Figure 4 shows the MSIS86 predicted neutral densities for the three orbits. We expect breakdown to be likely when the ambient density exceeds a few times 10^{16} m^{-3} . Again, for the 250 km orbit we fall well below this threshold for a shorter time than would be the case for a higher orbit.

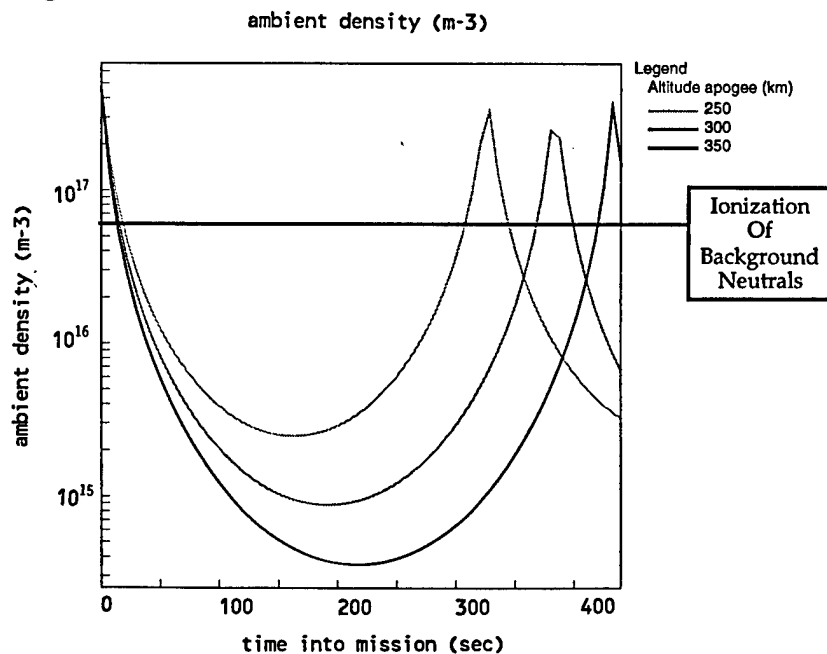


Figure 4. MSIS86 neutral density profiles for the three SPEAR-3 orbits.

3. DYNAPAC CALCULATIONS FOR SPEAR-3 FLOATING POTENTIALS AND CURRENTS

The floating potential of SPEAR-3 results from a balance between electron current collected on the positively biased sphere and secondary-electron-enhanced ion current collected by the negative rocket body. Simple models, which assume Parker-Murphy collection by the sphere and Langmuir-Blodgett collection by the rocket, generally predict that the bulk of the applied voltage will appear on the negative body. Results of these simple models are incorrect because (1) they neglect the effects of the interaction between the sphere and body sheaths, and (2) neither a sphere nor a cylinder gives a satisfactory estimate for the body sheath current.

Experience in calculating the floating potential of SPEAR-I gives us confidence that we know how to proceed. NASCAP/LEO calculations for SPEAR-I calculated floating potentials and currents by tracking ions and electrons in an assumed constant magnetic field and non-self-consistent potentials in which space charge is estimated by a nonlinear analytic screening formula. Using DynaPAC gives results with higher confidence levels because electrons will not be scattered by discontinuous electric fields.

Figure 5 shows the DynaPAC model for SPEAR-3. In addition to the essential cylinder-boom-graded boom-sphere configuration, the model includes the floating probe and its boom, the solar cell experiment, and some additional flush-mounted experiments. For the calculations of this chapter, all the experiments are assumed to be at rocket body potential, the plastic boom is assumed to be a plasma potential (despite having a grounded cable shield running along the outside), and the graded boom is in four sections biased at $1/8$, $3/8$, $5/8$, and $7/8$ of the capacitor voltage.

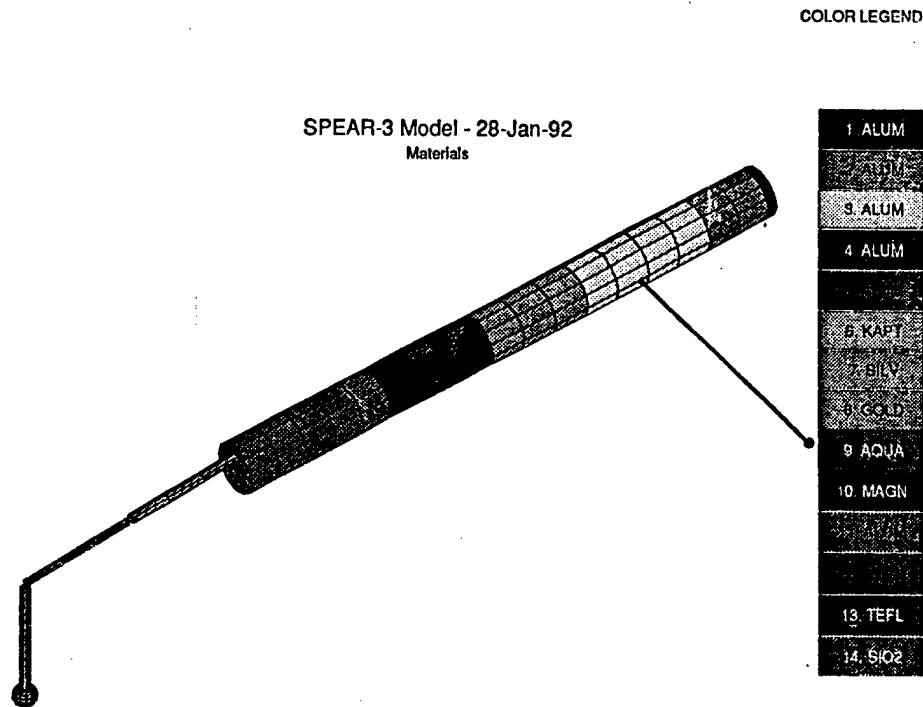


Figure 5. DynaPAC geometrical model for SPEAR-3.

The ionosphere model used in this chapter is given in Table 1.

Table 1. Ionospheric plasma properties assumed in this chapter.

Plasma Property	Value
Maximum Density	$2 \times 10^{11} \text{ m}^{-3}$
Minimum Density	$1 \times 10^9 \text{ m}^{-3}$
Plasma Temperature	0.1 eV
Magnetic Field	0.4 gauss
Ion Species	O^+

The effect of the sheath overlap differs depending on whether the overlap is weak or strong. Figure 6 shows a weak overlap case. Electrons that $\mathbf{E} \times \mathbf{B}$ drift along the sheath contour into the high electric field overlap region receive a waiver from the regulations of Parker and Murphy, so that they can contribute to the collected electron current. This effect is strongest when the magnetic field is normal to the plane of the figure (Science Attitude 1), and weakest when the

minimizes the intersection of the drift orbits with the sheath overlap region). The collected electron current exceeds the Parker-Murphy bound for all three magnetic field orientations.

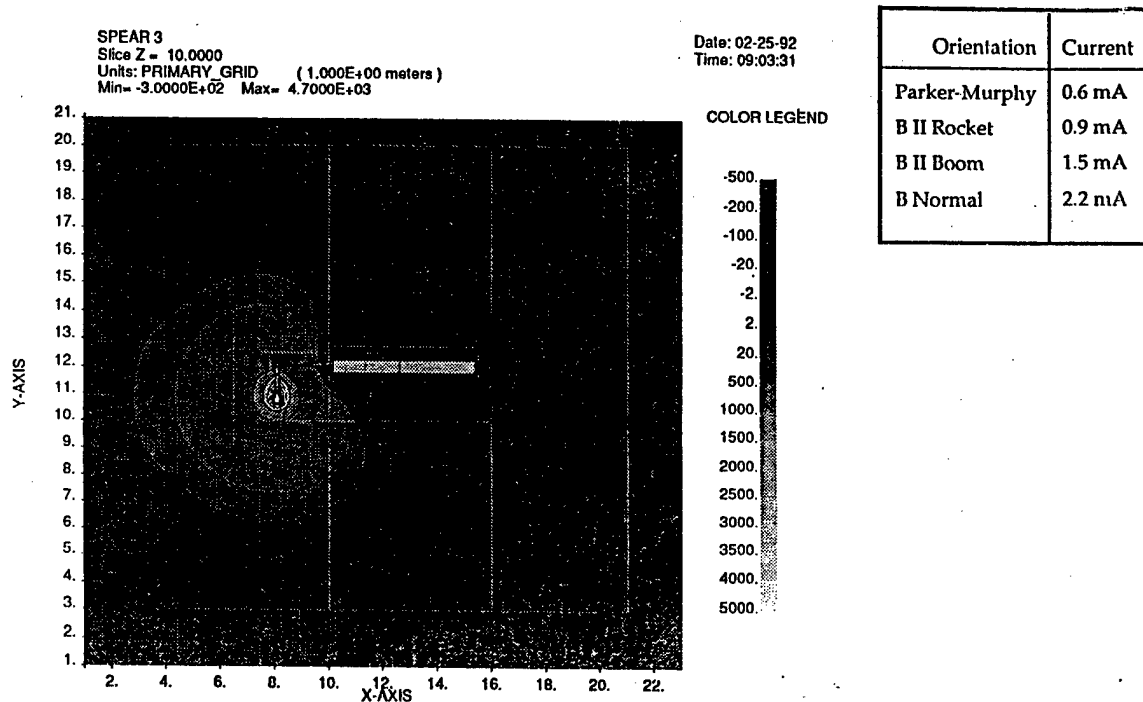


Figure 6. DynaPAC calculated electrostatic potentials about SPEAR-3, illustrating a case of weak sheath overlap.

Figure 7 illustrates the case of strong sheath overlap. Here, the body sheath nearly overwhelms the sphere sheath, which is both reduced in size and partially blocked by the immense negative potential region. This reduces the collected electron current well below the Parker-Murphy bound. The highest current now occurs when the magnetic field is parallel to the rocket body, since these experience the least blockage by electrostatic barriers.

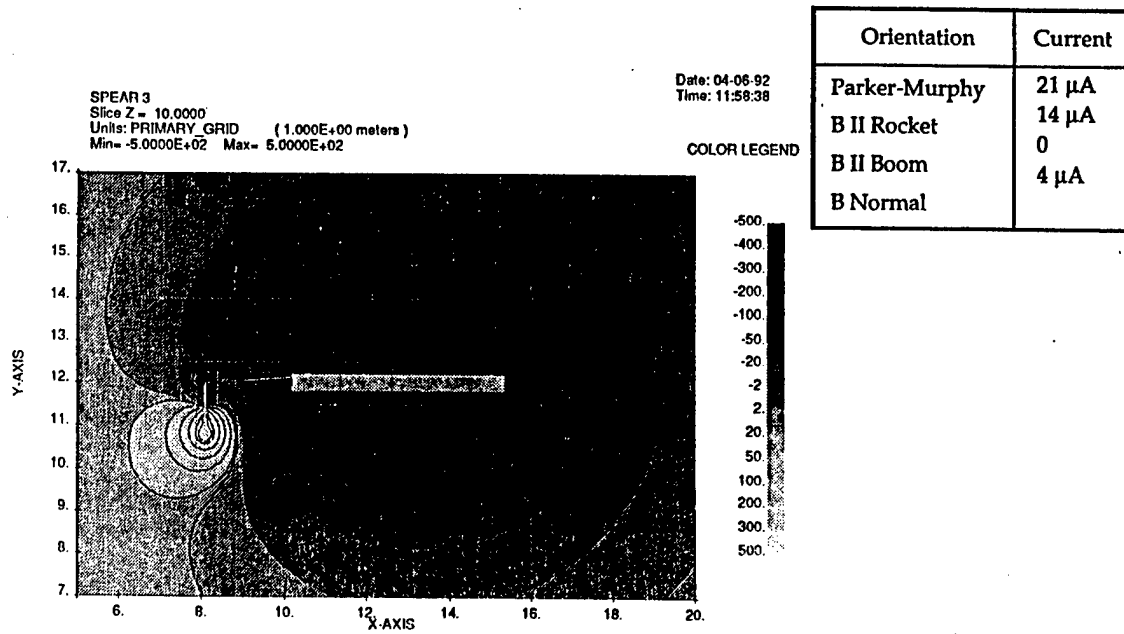


Figure 7. DynaPAC calculated electrostatic potentials about SPEAR-3, illustrating a case of strong sheath overlap.

Figure 8 shows the current variation as a function of assumed floating potential for the case of 16 kV capacitor voltage and $2 \times 10^{11} \text{ m}^{-3}$ plasma density. It is fairly typical that the floating potential occurs near the switch from weak-to-strong sheath overlap, so that there is only a weak dependence of floating potential and circuit current on magnetic field.

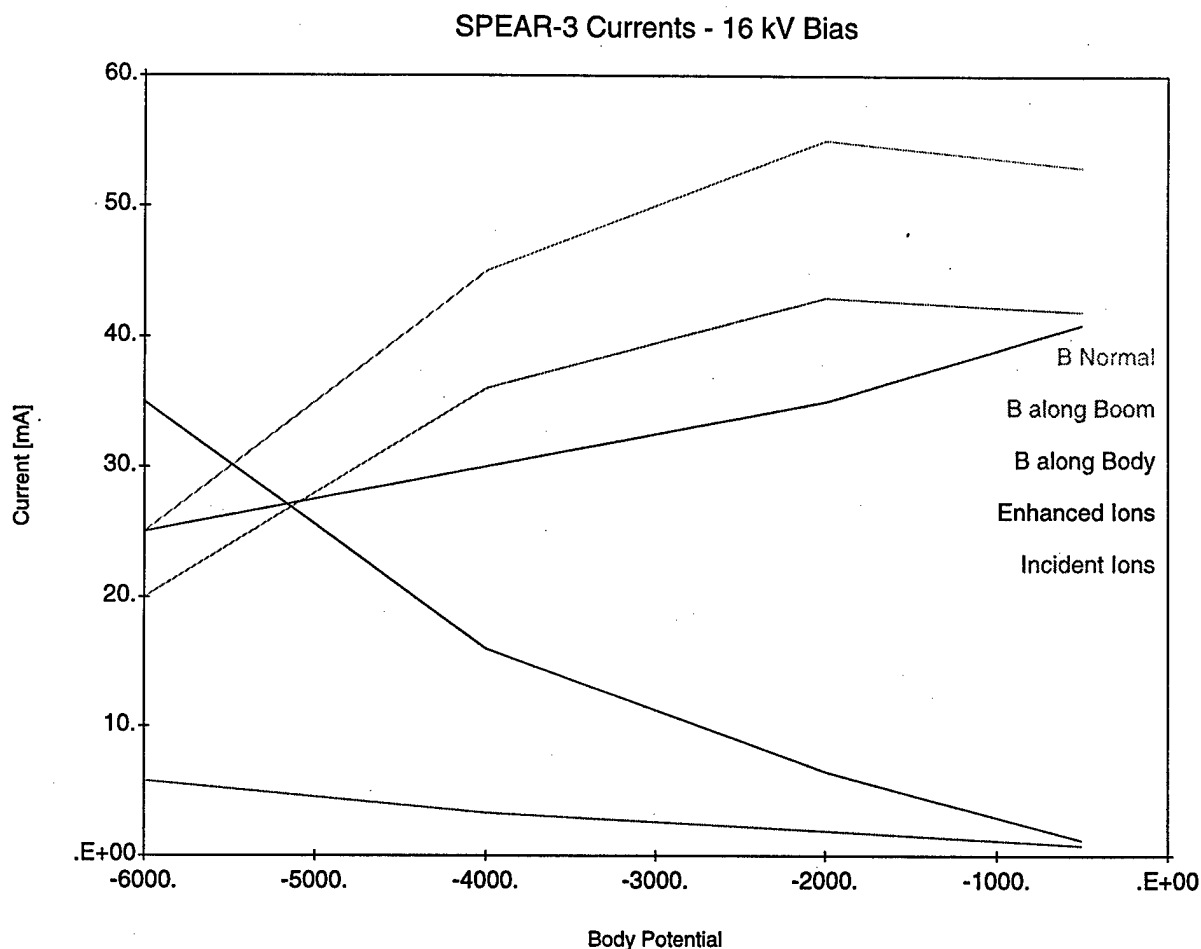


Figure 8. Variation of sphere and body currents as a function of assumed floating potential for 16 kV capacitor voltage, $2 \times 10^{11} \text{ m}^{-3}$ plasma density, and various magnetic field orientations.

Figure 9 shows a list of calculations performed with capacitor voltages of 1, 5, 10, and 16 kV, plasma densities in the range indicated in Table 1, and various assumed body potentials. Floating potentials inferred from these calculations are replotted in Figure 10 in terms of the fraction of the applied voltage which appears on the body. We see that this fraction decreases with applied voltage, and increases with plasma density. For high applied voltages ($> 5 \text{ kV}$) about one-third of the voltage typically appears on the body. At lower applied voltages ($\sim 1 \text{ kV}$) this fraction rises to one-half or more. Figure 11 shows the same floating potential information, but with circuit current values (milliamperes) indicated. We expect currents in the 10 milliampere range at the high end of the plasma density range, and in the 0.1 milliampere range at the lowest plasma densities.

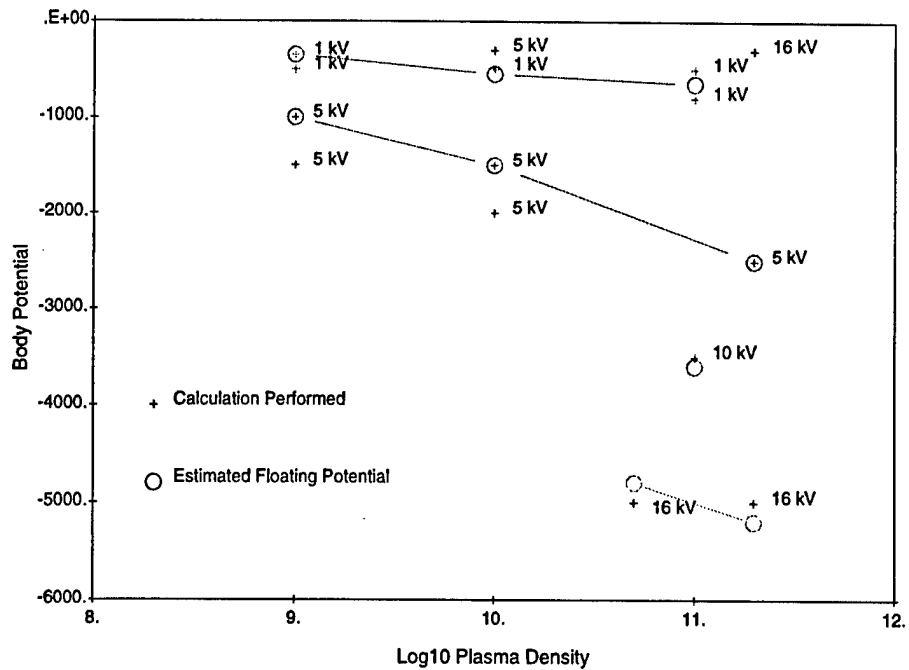


Figure 9. DynaPAC calculations performed ("+") for various capacitor voltages (noted on figure), plasma densities, and assumed body potentials. Circles represent estimated floating potentials.

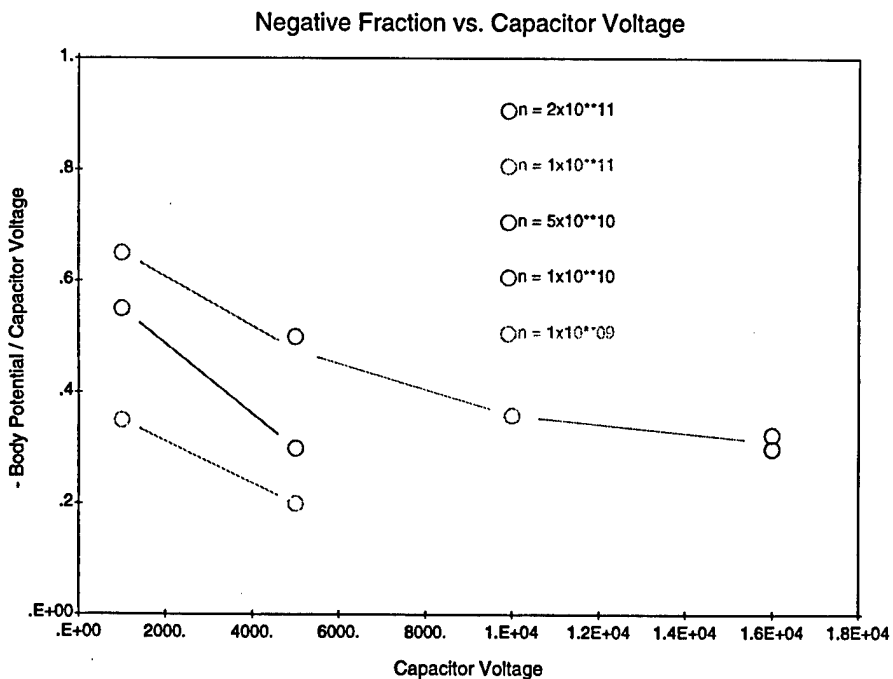


Figure 10. SPEAR-3 predicted floating potentials (expressed as the fraction of capacitor voltage appearing on the body) for various plasma densities. The lines represent plasma densities of 10^{11} m⁻³ (top), 10^{10} m⁻³ (middle), and 10^9 m⁻³ (bottom).

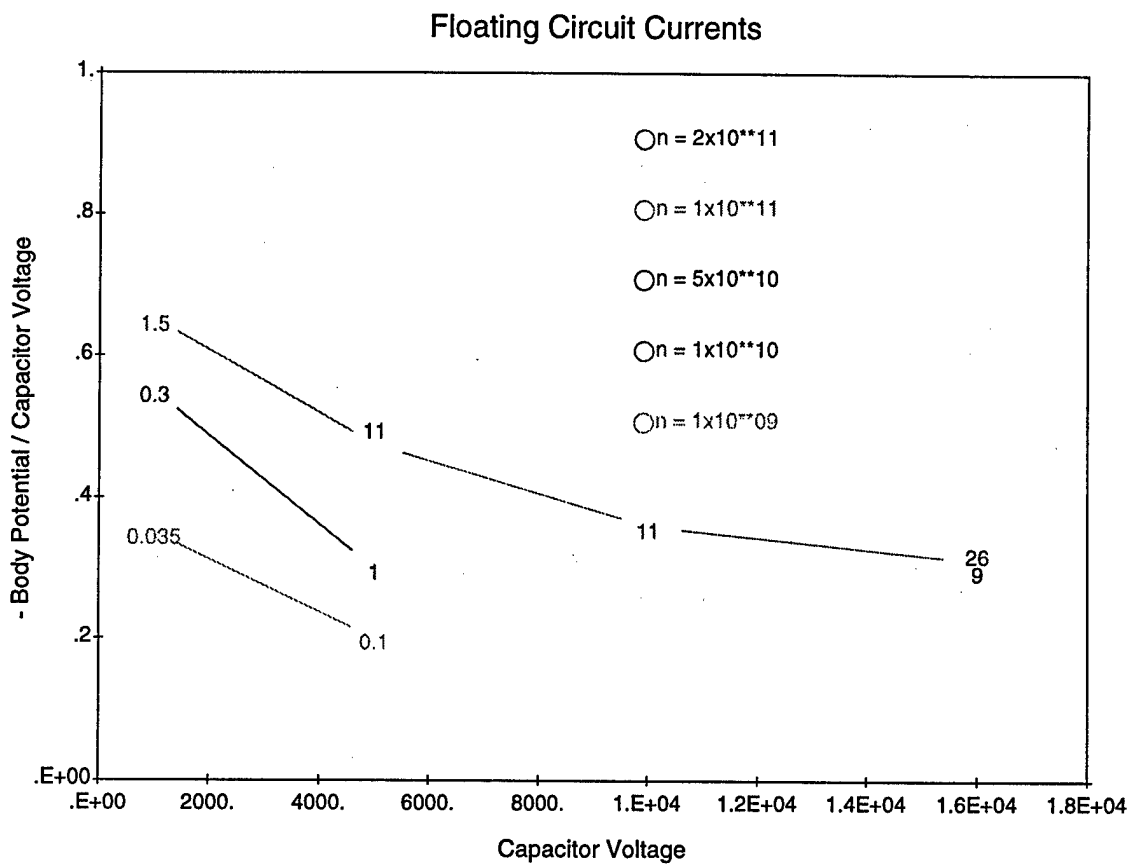


Figure 11. SPEAR-3 predicted plasma currents (milliamperes) in the same format as Figure 10.

4. DYNAPAC CALCULATIONS FOR ESA CURRENTS AND ANGLES

The DynaPAC calculations described in the previous chapter also allow us to calculate the distribution of sheath ion current over the body. This is important in order to be sure that there are sheath ions impacting the location of the Electrostatic Analyzer (particle detector), and to estimate the ion current and angular distribution to the detector in order to optimize the detector sensitivity.

Figure 12 shows a typical selection of ion trajectories from a sheath contour to the rocket. The first point to notice is that some portions of the rocket skin receive no ions, as they are totally electrostatically shadowed by the sphere sheath. The shadowed region typically covers nearly one-half of the boomward side of the rocket, and one-fourth to one-third of the side opposite the boom. The ESA is located just above the middle of the rocket (approximately 0.57 of the way from the bottom of the adapter ring to the top of the high voltage module) on the side opposite the boom. In no case of interest have we observed electrostatic shadowing of the particle detector position.

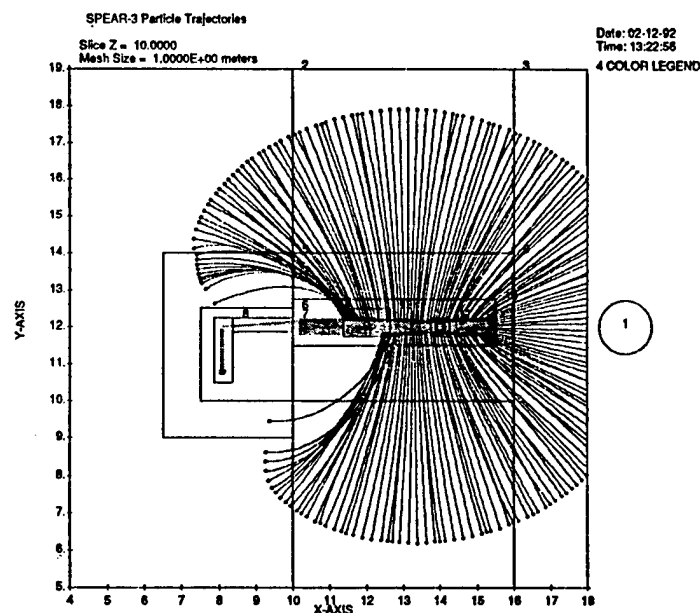


Figure 12. Typical ion trajectories from a sheath contour to the SPEAR-3 rocket body.

The second point to notice on Figure 12 is that the first several trajectories to the anti-boom side of the rocket cross, indicating focusing to a "hot spot". Figure 13 shows the flux to the entire rocket surface (for plasma density $1 \times 10^{11} \text{ m}^{-3}$, 5 kV capacitor voltage, and -1.5 kV body potential). Over most of the rocket (excluding the electrostatically shadowed portion) the ion flux (for this case) is about 0.1 milliamperes per square meter, but a hot spot with flux of 0.3 milliamperes per square meter is clearly seen near the transition from the electrostatically shadowed region.

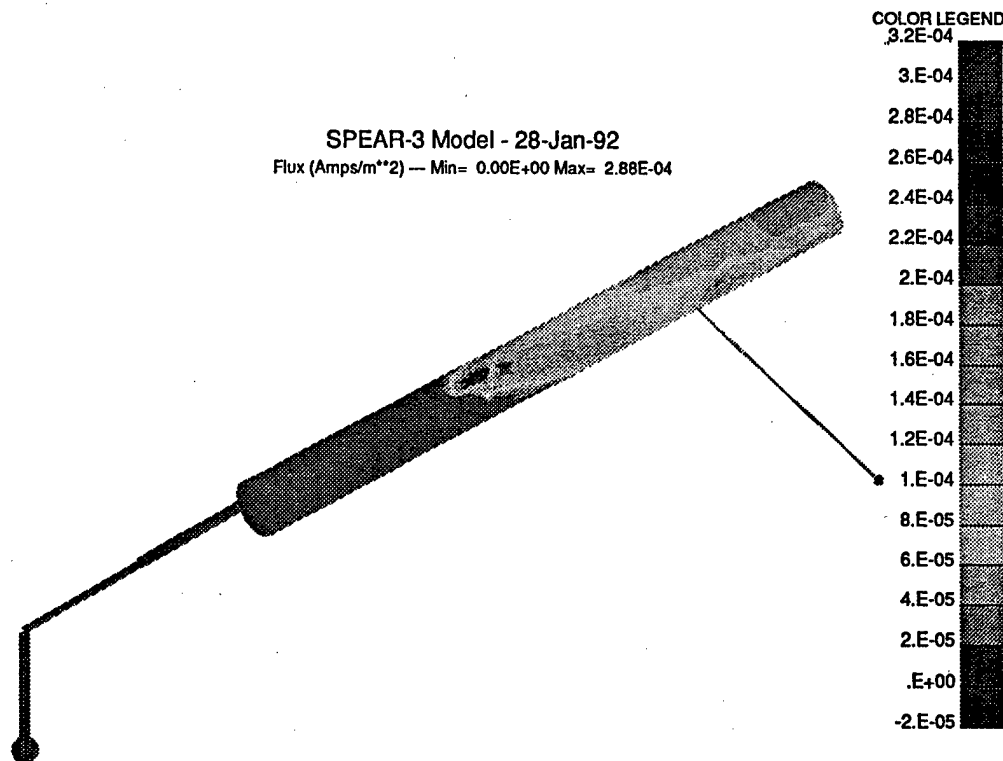


Figure 13. Ion flux density to the SPEAR-3 rocket surface.

Figure 14 shows the calculated current densities at the ESA location for the calculations indicated in Figure 9. The predicted current densities range over nearly two orders of magnitude (from nearly one milliampere per square meter down to about 10 microamperes per square meter), and correlate strongly with plasma density and less strongly with body potential. There is also appreciable variation due to the strong gradients of flux density (due to focusing effects) near the ESA location.

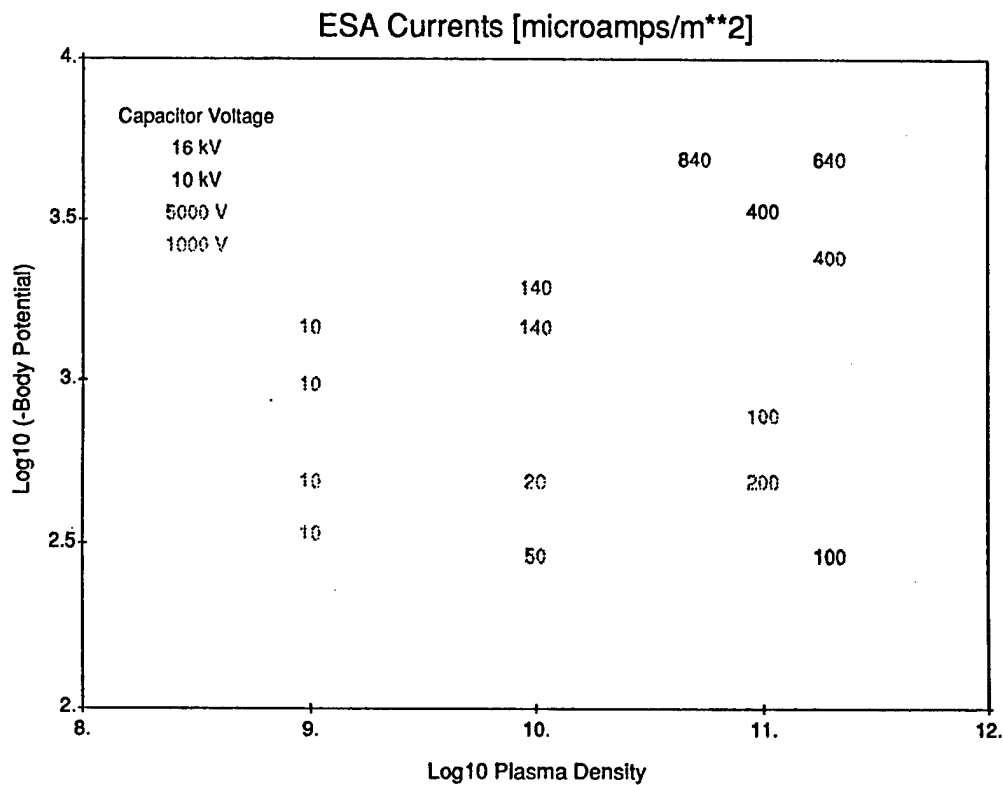


Figure 14. DynaPAC calculated flux densities to the ESA location for various plasma densities, body potentials, and capacitor voltages.

The angle of incidence of sheath ions to the particle detectors is also of concern, since the ESA's have limited angular range, and the proposed instruments do not scan in angle. Previous calculations (reverse trajectory calculations with DynaPAC) showed that the velocity component normal to the rocket axis was broadly distributed, corresponding to a broad distribution of the corresponding angle. However, the velocity component along the rocket axis was narrowly distributed, suggesting an angular distribution spanning only a few degrees.

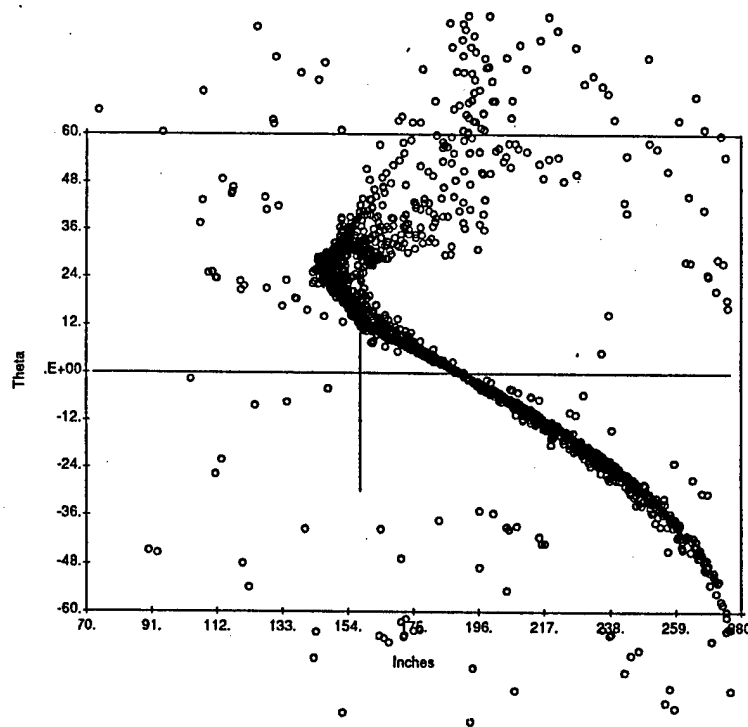


Figure 15. Incident angle (relative to surface normal) of ions striking the anti-boom side of the SPEAR-3 rocket body.

Figure 15 shows the incident angle of ion macroparticles impacting the anti-boom side of the rocket (as a function of position on the rocket) for the same case as Figure 13. At the particle detector position (vertical line) the incident angle of the main beam is seen to be about 12 degrees off normal. (Note also the vertical distribution just above the particle detector position, indicating focusing to the hot spot.) Figure 16 shows the incident angles (as a function of plasma density and body potential) according to the same scheme as Figure 14. In general, the predicted angle increases with increasing sheath size, i.e., with more negative body potential or with lower plasma density.

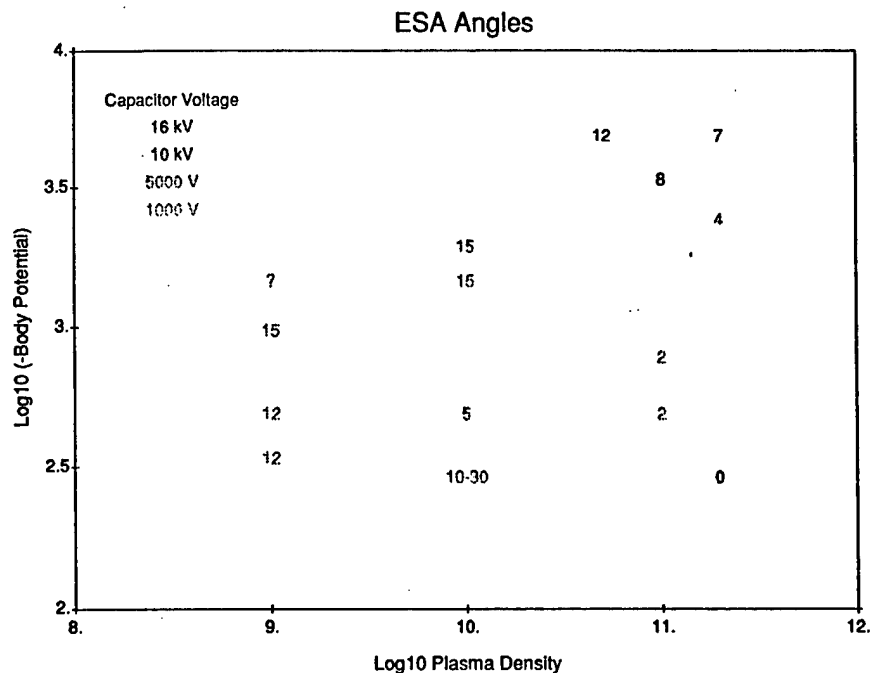


Figure 16. DynaPAC calculated incident angles at the ESA location for various plasma densities, body potentials, and capacitor voltages.

To compare with these predictions, Dr. R. C. Olsen (Naval Postgraduate School) reviewed the measurements by the ESA's on SPEAR-I. The SPEAR-I measurements indicated that the incident ions were broadly distributed in both energy and angle. The integrated current corresponded, at least roughly, to DynaPAC predictions. The energy distribution was a constant count rate up to the inferred spacecraft potential, with a high energy falloff characterized by a temperature of about one-tenth the inferred spacecraft potential. There was little angular dependence, except that, where charging peaks did occur, they tended to be at angles where DynaPAC would have predicted no incident flux. No plausible physical mechanisms have been proposed for degrading the sharp peak in energy and angle predicted by simple theory to the broad distribution observed by SPEAR-I.

On the basis of the DynaPAC calculations, we recommended ESA aperture diameters as shown in Table 2. The recommendations take into account the detector saturation at 1.6 picoamperes, and assume that one-fourth of the flux enters the detector (due to limited range in azimuthal angle). The recommended aperture diameter is then given by

$$d = 2.85 \times 10^{-6} J^{-1/2}$$

where J is the expected current density. Because the SPEAR-I results indicated a broad distribution of incident current, larger apertures (corresponding to 10^{14} and $10^{12} \text{ ster}^{-1} \text{ cm}^{-2} \text{ s}^{-1} \text{ E}^{-1}$) were adopted.

Table 2

Energy Range	Flux Range	Design Flux	Aperture Diameter	
			[microns]	[inches]
High	High	$1 \times 10^{-3} \text{ Am}^{-2}$	90	0.0035
High	Low	$3 \times 10^{-5} \text{ Am}^{-2}$	520	0.020
Low	High	$2 \times 10^{-4} \text{ Am}^{-2}$	200	0.008
Low	Low	$1 \times 10^{-5} \text{ Am}^{-2}$	900	0.035

Finally, it was suggested that ions produced in the sphere sheath might be seen in the particle detector measurements. Figure 17 shows trajectories of ions generated within the sphere sheath. Most are rapidly expelled from the spacecraft vicinity. While a minor fraction of the ions from the sphere sheath did impact the rocket body, none reached the particle detector location. This leads to the preliminary result that ions produced in the sphere sheath should not cause any problem for the ESA's.

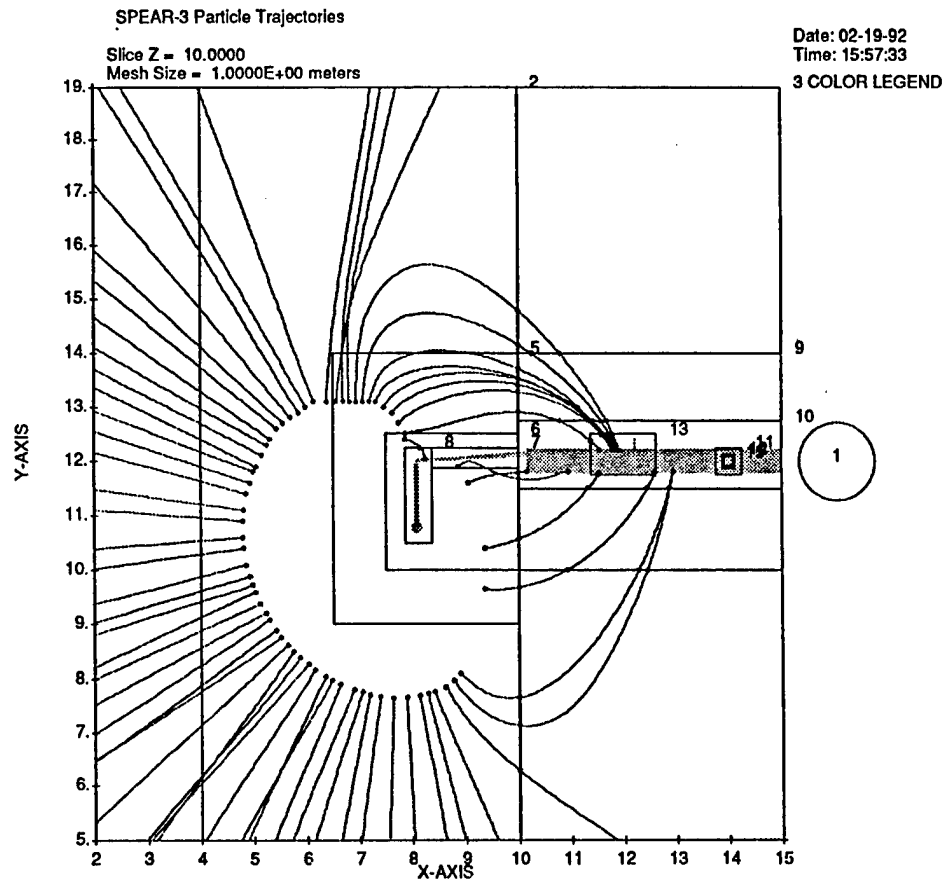


Figure 17. Trajectories of ions generated within the sphere sheath.

5. NEUTRAL DENSITIES PRODUCED BY THE NGRS (NEUTRAL GAS RELEASE SYSTEM)

The EPSAT model for nozzle plume and backflow density are being used under this contract to provide neutral densities to be used to calculate grounding of the rocket by the NGRS. Table 3 shows the input parameters for the nozzle as modeled by EPSAT.

Table 3 Nozzle Parameters

Nozzle length	.001
Exit radius	.00274
Exit mach #	7
Stagnation temp	.0223
Stagnation press	2×10^6
Throat radius	2.685×10^{-4}
Thrust	0.782
Area ratio	104
Number flow rate	2.16×10^{22}
Mass flow rate	1.005×10^{-3}
Gamma	1.4
Species	N2

A coarse plot of the effluent densities around the rocket is shown in Figure 18. The high voltage sphere is in the region of the nozzle backflow. We see that there is a substantial region near the nozzles with density exceeding 10^{19} m^{-3} , but the density falls to $3 \times 10^{16} \text{ m}^{-3}$ in the neighborhood of the sphere. This neutral density is probably low enough to avoid sphere breakdown, but with less safety margin than would be desirable.

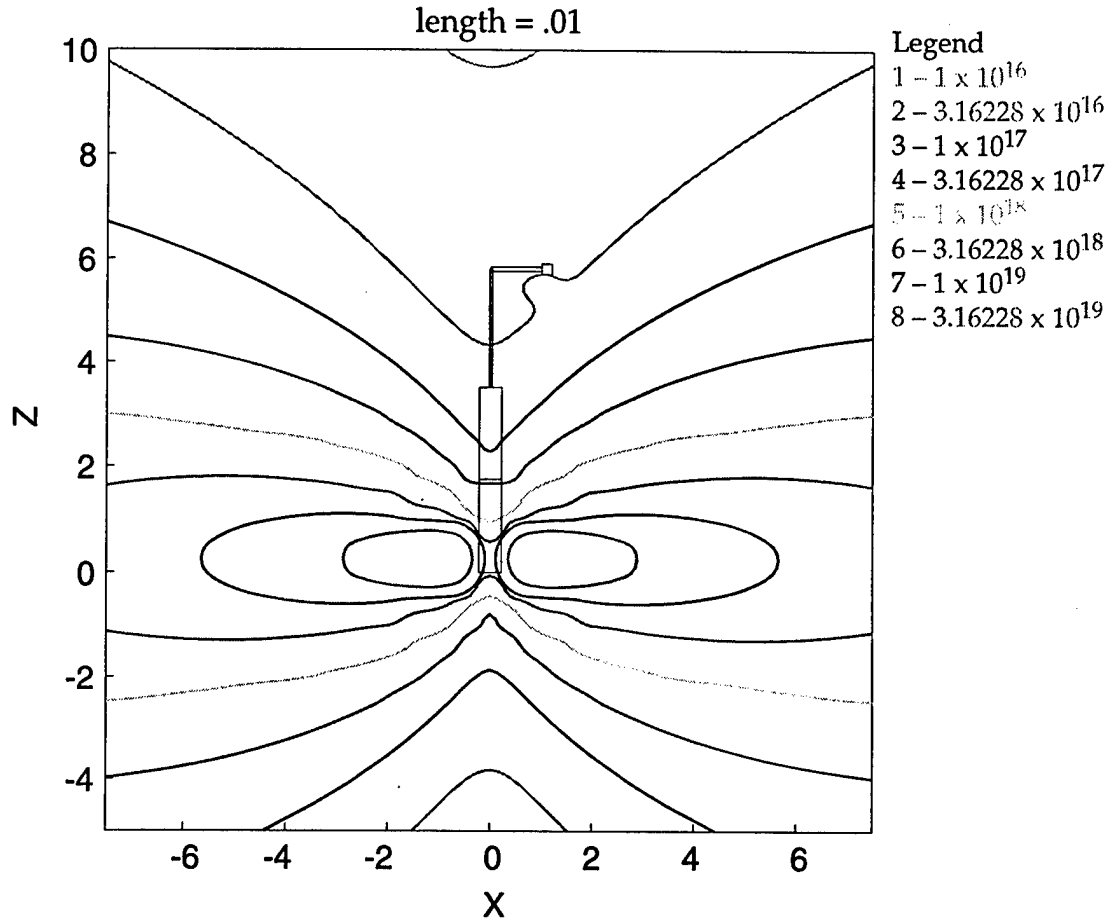


Figure 18. EPSAT plot of neutral density [m^{-3}] about SPEAR-3 resulting from four nozzles.

Figure 19 shows the density at three positions on the rocket as a function of flow rate, with the breakdown regime indicated to begin at a density of 10^{17} m^{-3} . The high voltage sphere appears to be safe for flow rates below ten grams per second, but the safety factor is not high. Increasing the mach number of the flow should improve the situation with regard to sphere breakdown.

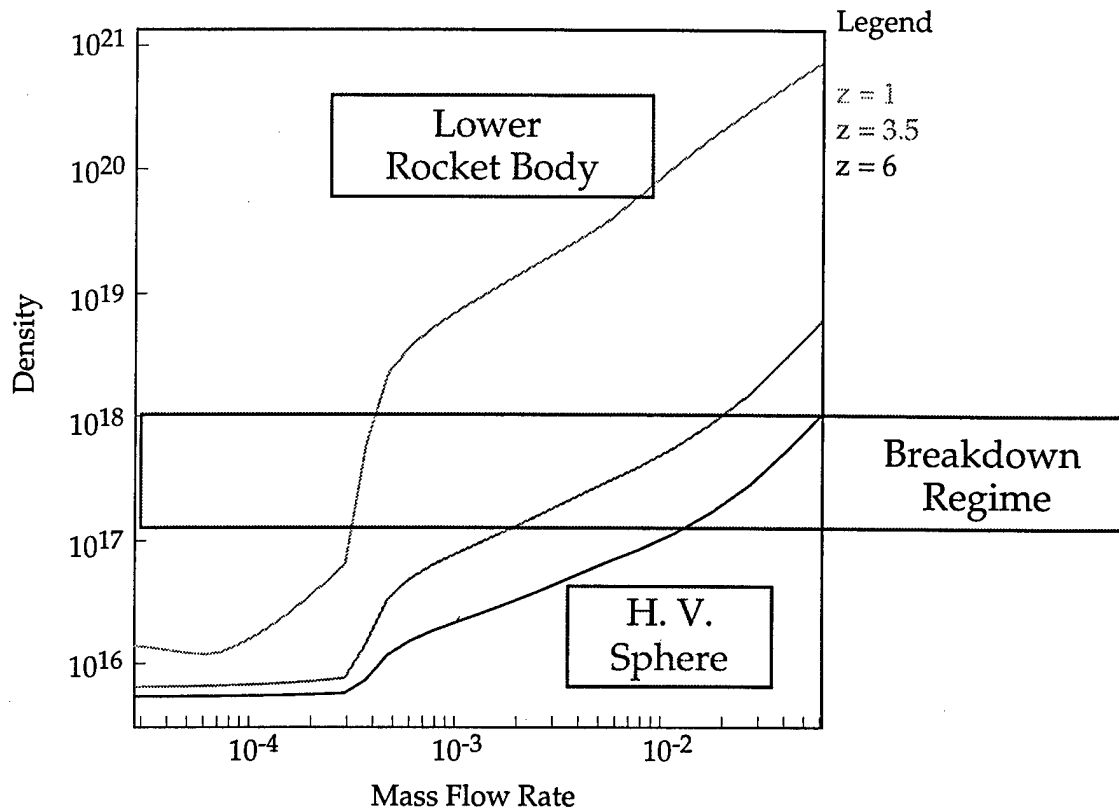


Figure 19. EPSAT-calculated neutral densities near the lower rocket body, top of rocket body, and high voltage sphere. Sphere breakdown is expected for densities above about 10^{17} m^{-3} .

The EPSAT generated density field has been incorporated into DynaPAC for use in three-dimensional calculations. Figures 20 (a and b) show two views of the density field plotted using DynaPAC software. The highest densities occur at the nozzle, but radial paths pass quickly through these very high densities. On the other hand, radial paths along the nozzle direction see modest densities for very long distances.

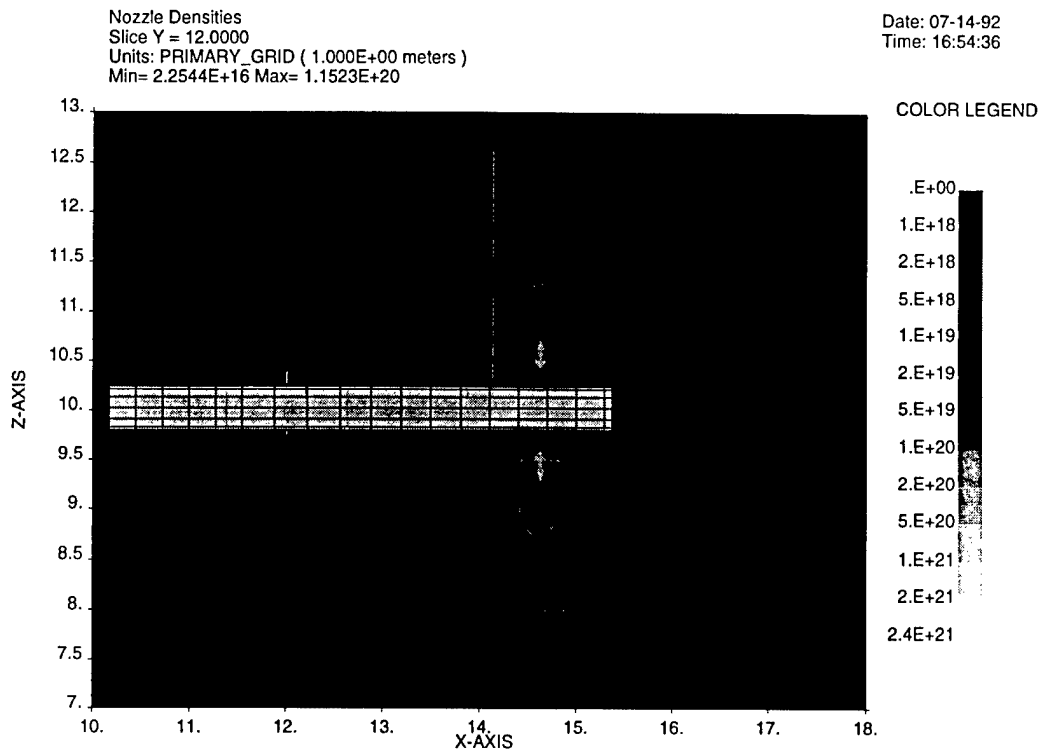


Figure 20. (a) EPSAT-calculated neutral density about SPEAR-3 plotted using DynaPAC: (a) Plane containing rocket axis and nozzle flow direction.

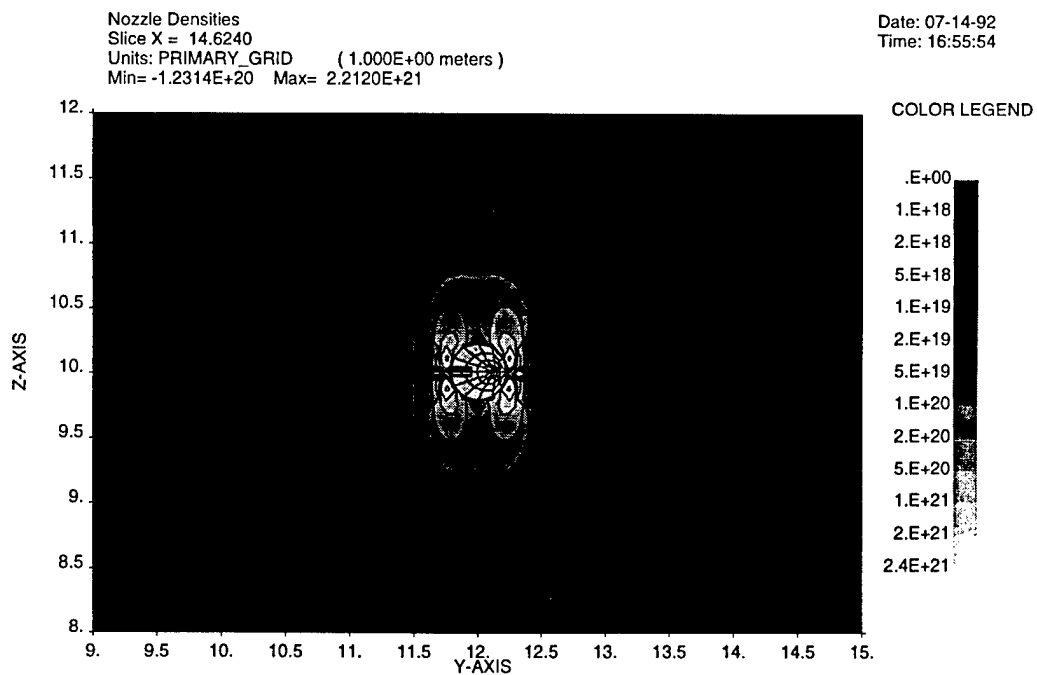


Figure 20. (b) Plane normal to rocket axis at nozzle location.

This is further illustrated in Figures 21 (a and b), with show column densities and linear gains along radial paths. Conventional phenomenology (Paschen curves) suggest that breakdown takes place along paths with column densities of one half to one torr-cm. The torr-cm plot shows that most paths satisfying this criterion occur not at the nozzle location, but 45 to 90 degrees away, passing either along the plume or obliquely through the plume. The "linear amplification" plot delineates the number of secondary electrons produced by the process of an electron leaving the rocket surface, producing ions without slowing down, and having those ions return to the rocket without charge exchanging. The regions of high gain match well the regions where column density is well-suited to breakdown.

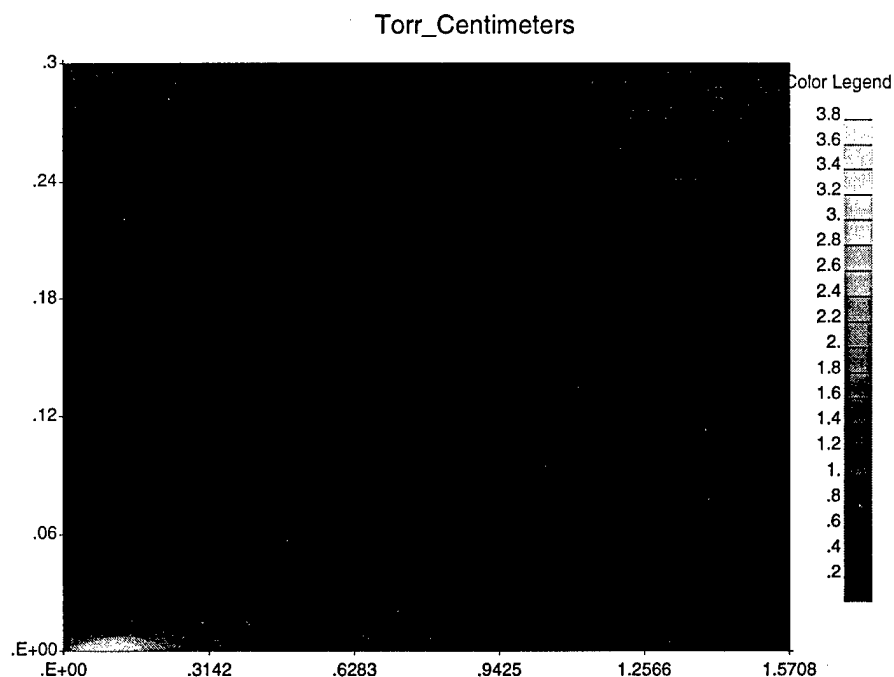


Figure 21. (a) Properties of the plasma plume obtained by integrating along a radial path. On the left side of the figure, the path passes through the nozzle location normal to the flow direction. On the right side of the figure the path parallels the flow direction. (a) Integral of neutral density (column density) expressed in units of torr-cm.

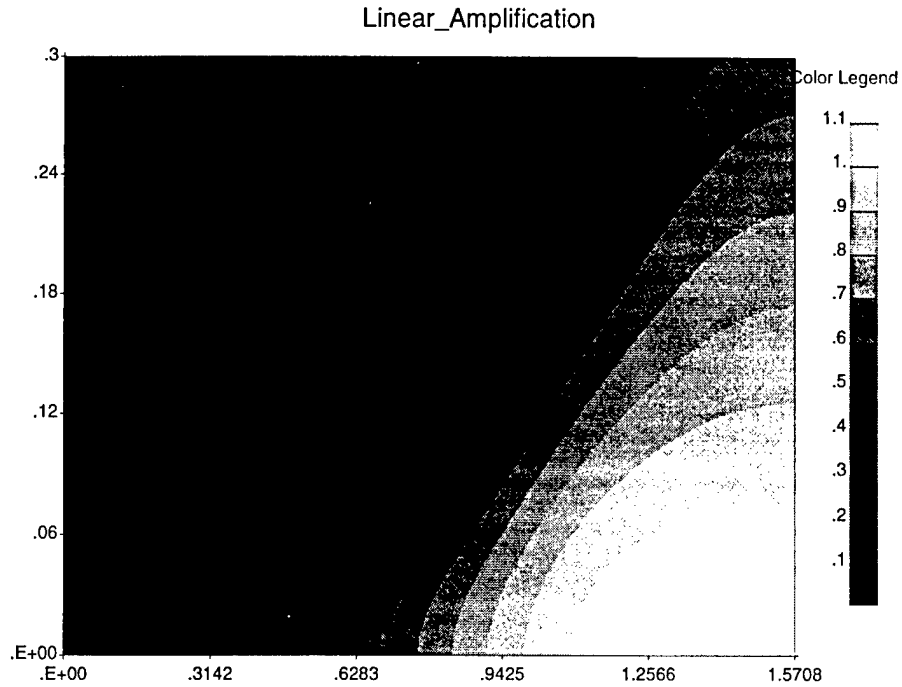


Figure 21. (b) Integral of neutral density time ionization cross-section times secondary emission coefficient.

This analysis depends on conventional phenomenology, which deals with constant densities and electric fields. Also, the importance of charge exchange remains to be assessed. Three-dimensional trajectory effects may also impact the likelihood of breakdown. This work will progress in the next period.

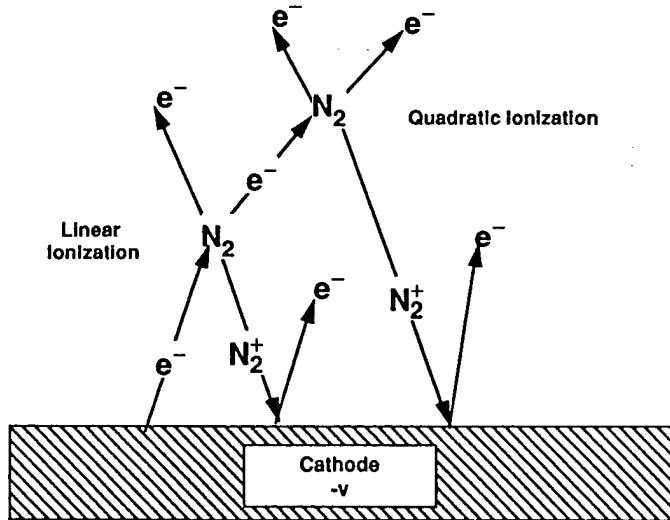
6. NGRS-INDUCED BREAKDOWN OF THE SPEAR-3 NEGATIVE BODY SHEATH

This chapter describes preliminary three-dimensional considerations for NGRS-induced breakdown calculated using DynaPAC, and a dynamic, two-dimensional breakdown calculation using Gilbert. In this chapter we consider the neutral species to be molecular nitrogen, although argon will actually be used in the SPEAR-3 NGRS. These results were presented at NASA Plum Brook Station in July, 1992.

6.1. Three-Dimensional Considerations

Figure 22 illustrates the processes of ionization breakdown for negative potentials. An electron leaving the surface interacts with a neutral to yield an ion and an electron. The ion is accelerated back to the surface and creates secondary electrons. This process scales linearly with the neutral density. The newly created electron may interact with another neutral. Because two neutral collisions are involved, the number of secondary electrons produced as a result of second collisions scales quadratically with the neutral density. While we consider primarily the linear order processes in this chapter, higher order processes are important in achieving breakdown.

**Breakdown Is Initiated When:
Each Electron Emitted From Surface
Produces At Least One New Electron
From The Surface**



- Each electron Generates
 $\Gamma \approx e^{(\rho \sigma \ell)} - 1$ Ions

- Each generated ion produces γ surface secondary electrons

- When $\gamma\Gamma = 1$ the system is unstable and an exponential buildup of ionization occurs

Positive Feedback , $\gamma\Gamma \geq 1$,
Causes Breakdown Initiation

Figure 22. Breakdown initiation process for a negatively biased system.

Suppose that the dominant collisions occur more than one radius from the rocket. Ionizing electrons have then been accelerated to nearly the full rocket potential, and returning ions gain this energy as well. The number of secondary electrons is proportional to the ionization cross-section for this energy times the ion-induced secondary yield. These two functions, with their product, are shown in Figure 23. The product rises sharply in the 500 to 1000 volt range, suggesting that a stable breakdown phase can occur. This is valid only for low gas densities, as we have neglected the effects of charge exchange.

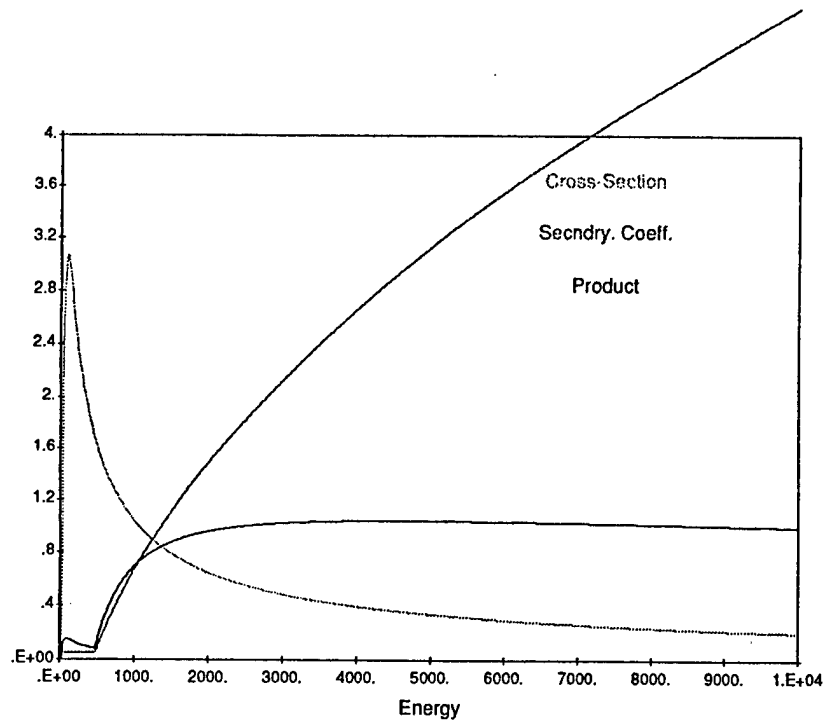


Figure 23. Ionization cross-section (for electrons on N_2), ion-induced secondary emission coefficient, and their product.

We set out to calculate the linear amplification process for actual SPEAR-3 potentials and nozzle densities. The potential field used is shown in Figure 24. It corresponds to 10 kV capacitor potential and a plasma density of $1 \times 10^{11} \text{ m}^{-3}$, at the estimated floating potential of -3.5 kV. Electrons were tracked outward from the center of each surface cell on the rocket model. Ions were created in proportion to the ionization cross-section for the electron energy times the neutral density. The created ions were then tracked back to the rocket where they created secondary electrons. Electron energy loss mechanisms were neglected (under the assumption that the number of ions per electron would be small). Ion charge exchange was neglected (under the assumption of small neutral density).

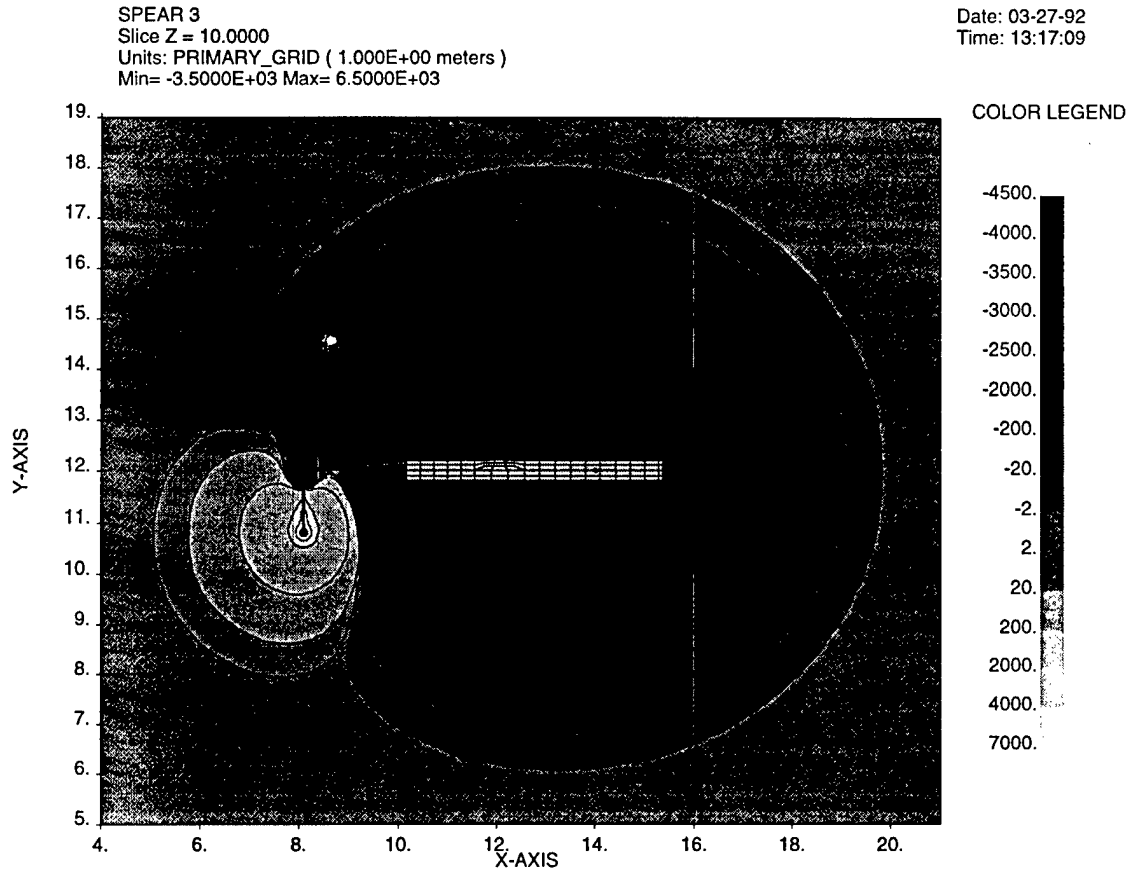


Figure 24. Potential field used for three-dimensional ionization calculations, corresponding to 10 kV capacitor voltage, -3.5 kV body potential, and 10^{11} m^{-3} plasma density.

In order to sustain breakdown, the secondary electrons must be created at the approximate location where the primary was emitted. As a first cut, we take this to mean the same surface cell of the DynaPAC model. Figure 25 shows the number of secondary electrons produced (by the process described above) at the same cell as the emitted primary. The cells with substantial values are in the neighborhood of the nozzles, and face the nozzle flow direction. The maximum of this diagonal secondary production term was 0.91. Some of the properties of the trajectory having this maximum are shown in Table 4.

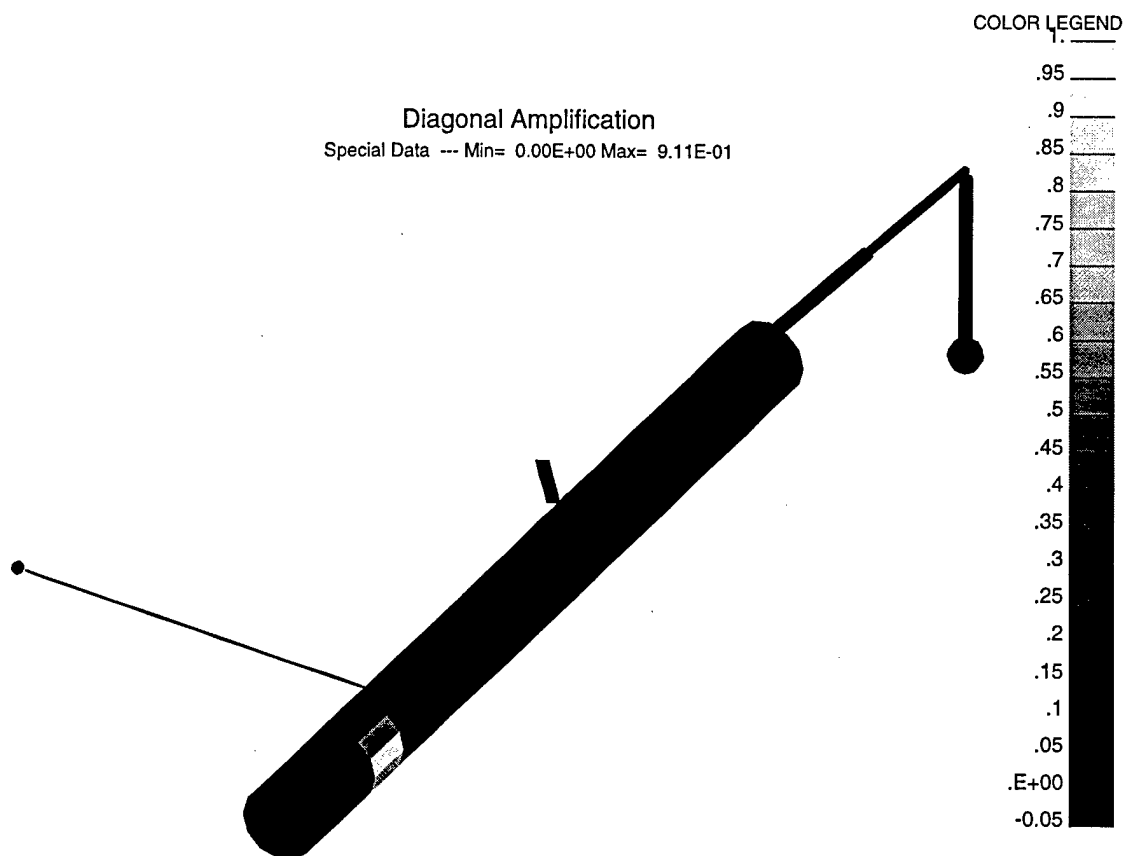


Figure 25. Secondary electron production resulting from primary electron emitted from same cell.

Three-dimensional effects tend to reduce the diagonal amplification. Because emitted electrons receive their initial acceleration near the rocket, where fields are radially outward, their trajectories are approximately radially outward. Ions, however, are created far from the rocket, where electric fields have a substantial component toward the rocket center. This causes an incipient electron avalanche to migrate toward the rocket center, where it fizzles for lack of neutral density. However, the magnetic field can play a role in reducing this effect. In the case of the cell with maximum diagonal secondary production, the magnetic field (for science attitude 1) deflects electrons toward the rear of the rocket. Still, on average, secondary electrons are produced nearly five inches from the site of primary emission. For a neighboring cell located similarly and symmetrically, but for which magnetic deflection is toward the top of the rocket, displacement of secondary production grows to seven inches.

For the most interesting surface cell, we also calculated the quadratic ion production, i.e., ions produced by ionization-produced electrons. The number of quadratic ions (see Table 4) was, for this density, greater than the number of first generation ions.

Table 4

For cell with maximum likelihood of breakdown:	
Direction	Nearly along flow direction
First generation ions	1.36
First generation sec. electrons	1.2
Diagonal sec. electrons	0.91
Mean ion impact distance	5.5 cm
Mean secondary production	11.7 cm
Second generation ions	1.75
For neighboring cell (magnetic field effect)	
Mean ion impact distance	8.85 cm
Mean secondary production	17.7 cm

6.2. Two Dimensional Breakdown Calculation

Two-dimensional calculations of breakdown induced by nozzle flow were done using the Gilbert code. The purpose of these calculations was to develop the experience, techniques, and expertise needed to successfully attack the three-dimensional problem.

The rocket was represented as a sphere with radius 0.57 cm. The neutral density was obtained by taking densities corresponding to the 1 gram per second flow rate nozzle firing tangentially to the sphere, and rotating the densities (in the plane formed by the nozzle axis and the sphere center) about the sphere diameter (passing through the nozzle). (Angle-averaging the density provided by two such nozzles gave insufficient neutral density to cause breakdown.) The neutral species was N₂. Electrons were taken with their true mass and with mass enhanced by 100, and runs were done with initial potentials of -3.5 kV and -2 kV.

Two new features were introduced for these calculations. First, an energy-dependent slowing down field (for electrons) was developed in order to reproduce the high density side of a Paschen curve. The slowing-down field is

$$E_{\text{slow}} = B N / \log (A / \sigma (\epsilon))$$

where

$$N = \text{Neutral Density [m}^{-3}\text{]}$$

$$A = 3.43 \times 10^{-20} \text{ m}^2$$

$$B = 1 \times 10^{-18} \text{ volt} \cdot \text{m}^2$$

$$\epsilon = \text{electron energy}$$

$$\sigma = \text{ionization cross-section}$$

The second improvement was to introduce an implicit algorithm (similar to those which have appeared in the literature) capable of handling very high plasma densities. The algorithm replaces Poisson's equation with

$$-\text{div} [1 + 1/2 (\omega_p (r) \delta t)^2] \text{grad } \phi = \rho_A / \epsilon_0$$

where ρ_A is the "free streaming" charge density, i.e., the charge density calculated after moving particles at constant velocity for δt . (The plasma frequency is also calculated using the free-streaming densities.) The algorithm consists of (1) doing the free-streaming pre-push, (2) solving for the implicit potentials, and (3) performing the actual particle push. It is not necessary to ever solve for the actual potentials. Particle deposition must be accounted for in the pre-push, but particle emission need not be done in the pre-push.

Table 5 shows the time dependence of the discharge. (Times up to 12 μs are for real mass electrons. The heavy electron run behaved similarly, but with some modest changes in the dynamics.) The run was started with the sphere at -3500 volts and emitting a small current of seed electrons. Significant ion return began at about two μs , and the ion-generated secondaries soon dominated the problem. A peak potential of -120 volts was reached but could not be sustained. The final steady state oscillated about a potential of -850 volts, with excursions of $\pm 200 \text{ V}$ and a frequency of about 20 kHz.

Table 5

Time [μ s]	
0	Sphere at -3500 volts
2	Significant ion return current begins
6	Total space charge peaks
7	Steady ion return current of 20 mA reached
8	Peak ion space charge
9	Ion current begins to drop
9	Peak electron space charge
11	Peak secondary electron current
12	Peak potential of -120 volts
20-60	Mean ion return current of 2.5 mA
25	Total space charge has minimum
70	Equilibrium reached at -850 volts
	Mean secondary emission coefficient ~ 0.15
>100	Oscillations ± 200 V, ~ 20 kHz

As we expected for the three-dimensional case, discharge was predominantly along a path passing obliquely through the nozzle plume. A quasi-neutral, dense plasma region was formed where the greatest ionization took place. Figures 26 show the electrostatic potential, ion density, and electron density during the discharge. The regions of high electron and ion density coincide, and a cathode fall region, with increased electric field, is created between the sphere surface and the quasi-neutral region.

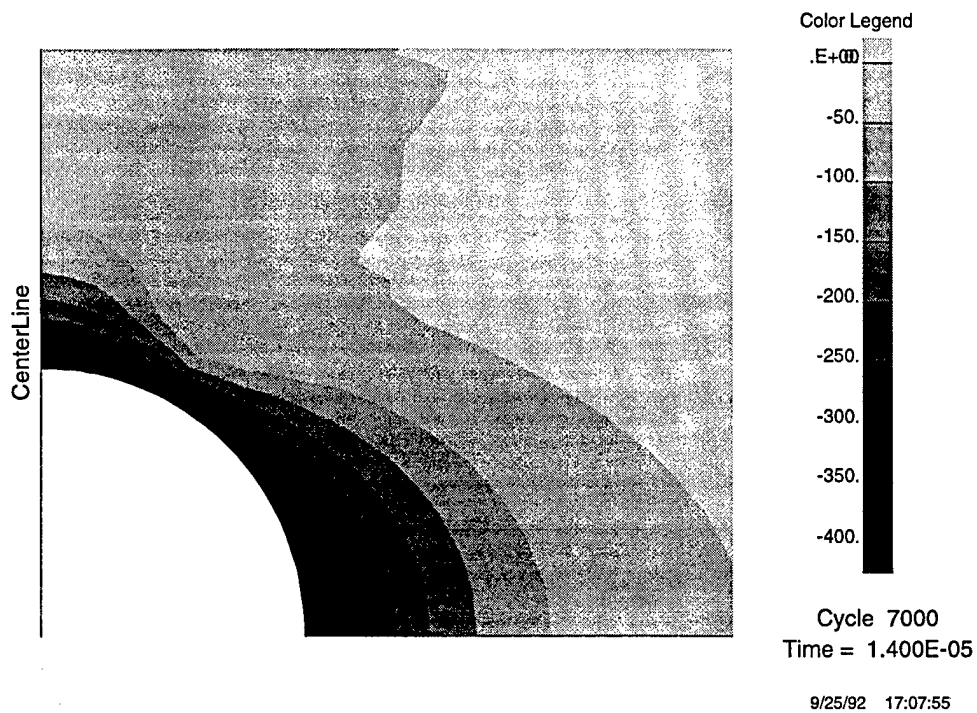


Figure 26. (a) Electrostatic potentials during breakdown, showing localized cathode fall region.

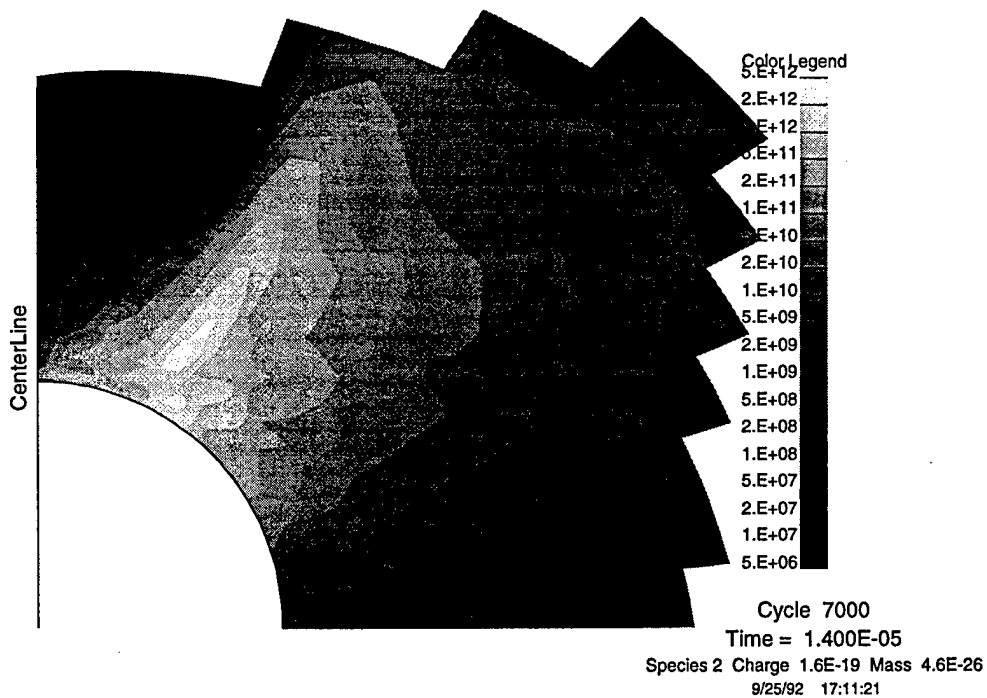


Figure 26. (b) Plasma ion density during breakdown, showing formation of a high density region at an oblique angle to the nozzle flow.

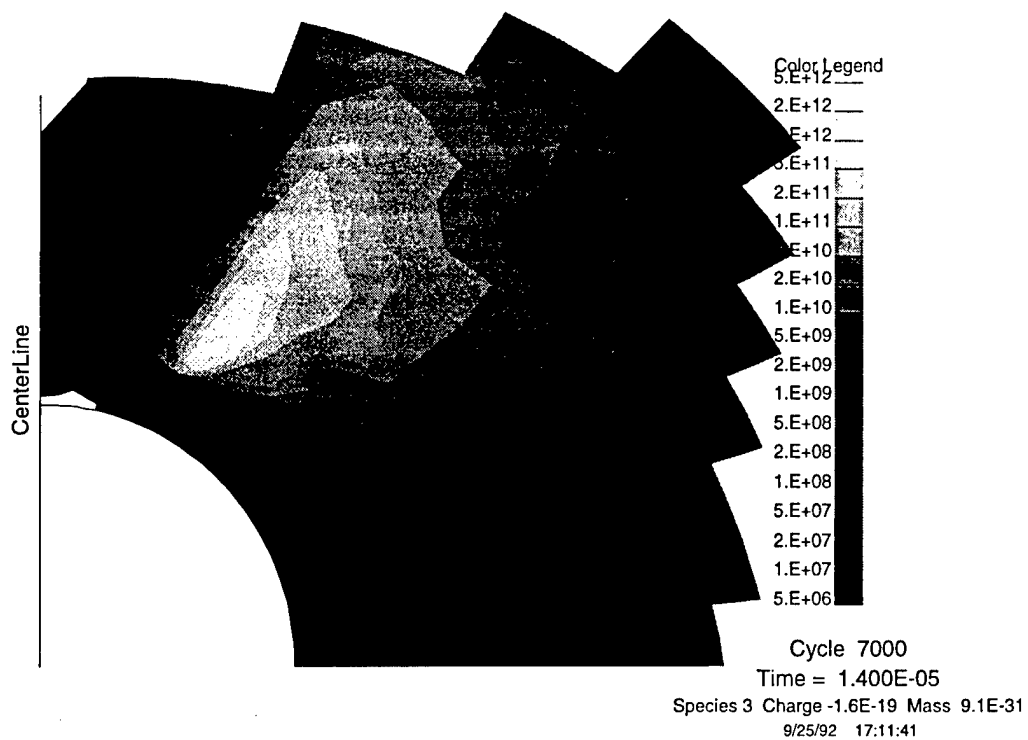


Figure 26. (c) Plasma electron density during breakdown, showing high electron density coincident with the ion density.

6.3. Continuous Slowing Down Approximation

The importance of estimating the required gas flow for the SPEAR-3 neutral gas release system led us to pursue yet another approach to calculating breakdown in the neutral plume (shown in Figure 20). This approach was to calculate the number of electron-ion pairs produced as a result of one electron emitted from the rocket and traveling a radial path (i.e., following the electric field) through the three-dimensional gas plume. The ions produced return to the rocket at low energy due to charge exchange, and thus have a secondary electron coefficient in the range 0.05 to 0.1. If their number is sufficient to reproduce the original electron by secondary emission, breakdown will occur.

Analytic formulas were fit to published cross-section and energy loss data for electron impact on neutral Argon. The ionization cross section fit is

$$\sigma(E) = 1.1 \times 10^{-16} \frac{E - 15.8}{(100 + E)^2} \text{ m}^2$$

The energy loss fit is

$$L(E) = 4 \times 10^{-16} \frac{E - 12}{100 + E} \text{ V m}^2$$

The electron macroparticles generate electron-ion pairs and loose energy independently.

This approach reproduces the Paschen curves for parallel plate geometry. Figure 27 shows the inverse of the second Townsend coefficient as a function of the the voltage and the column density for the parallel plate geometry.

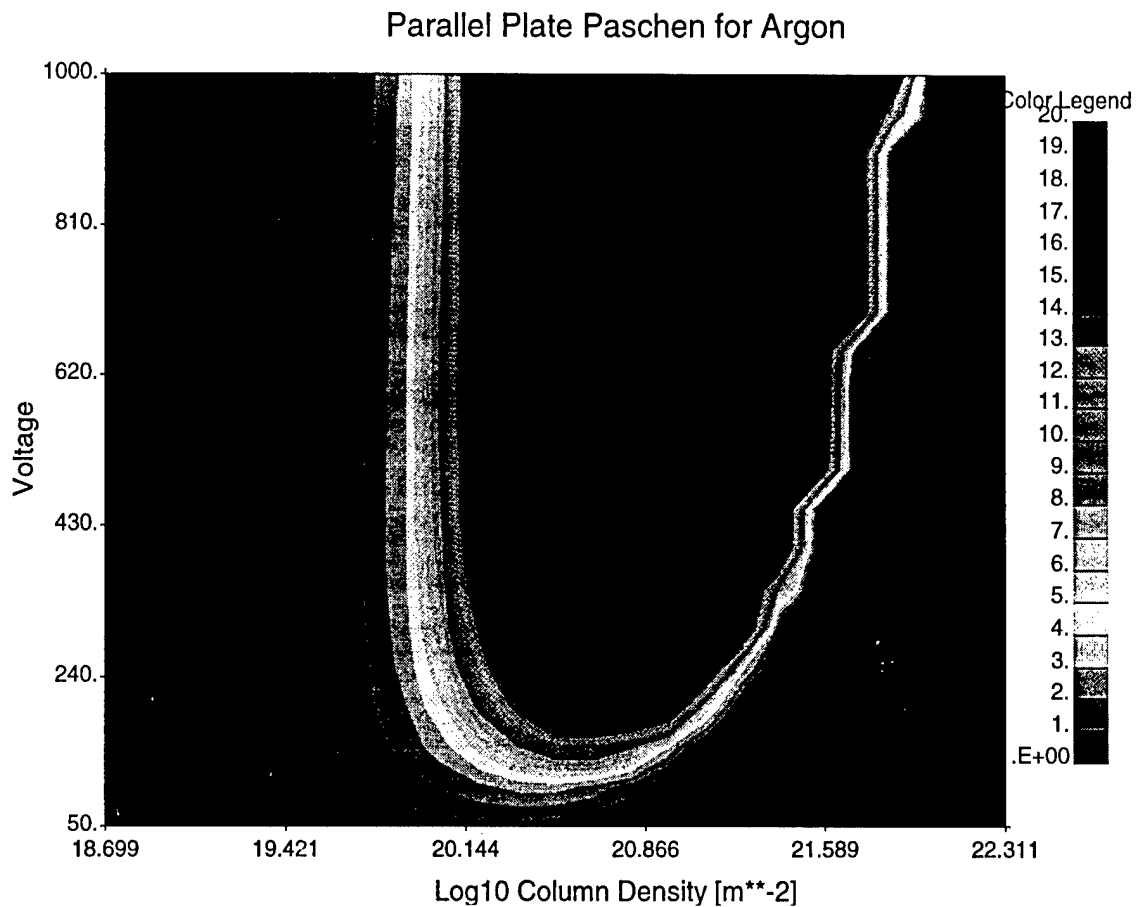


Figure 27. Argon Paschen Profile for the parallel plate geometry using the continuous slowing down approximation.

Using this approach, the second Townsend coefficient was computed for radial electron paths outward from the SPEAR 3 rocket body for various flow rates. The inverse of the second Townsend coefficient for nozzle flow rates of 0.25, 1, and 2 grams per second are shown in Figure 27 as a function of direction and potential.

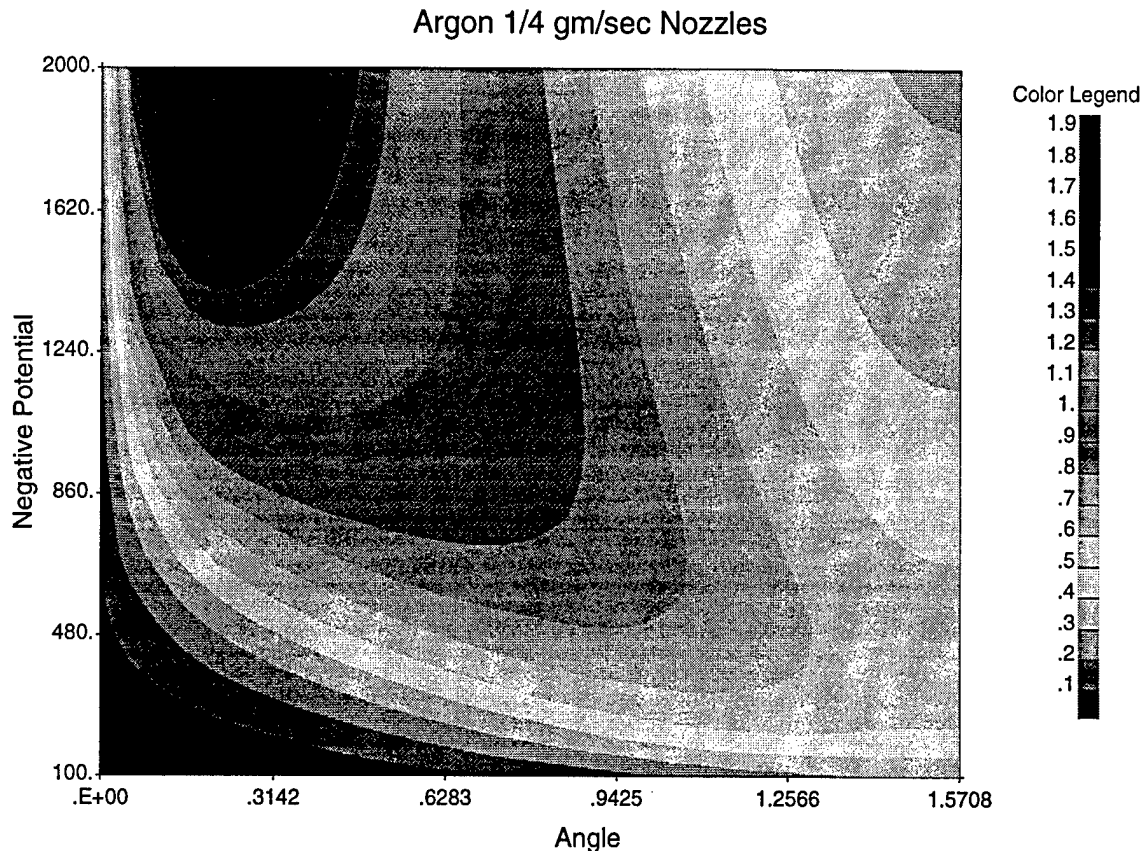


Figure 28. (a) Inverse of the second Townsend coefficient for a nozzle flow rate of 0.25, 1, and 2 grams per second as a function of the angle from the nozzle location and the potential of the body with respect to the plasma.

The conclusions of these calculations were that (a) A nozzle flow of 2 grams per second per nozzle would be required to produce breakdown and ground the rocket. (b) During such grounding the rocket potential would be held to about 200 volts negative. (c) The breakdown path would occur 90 degrees from the nozzle location, in the direction of the gas flow.

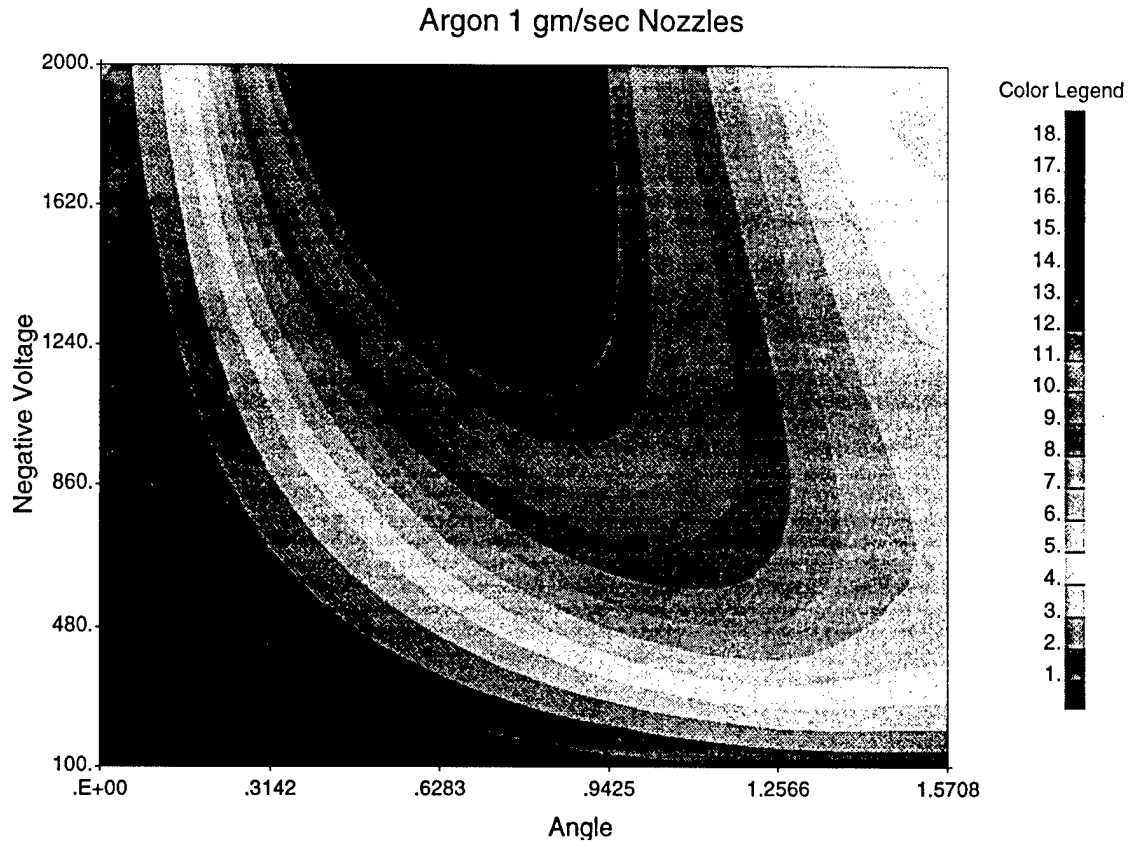


Figure 28. (b) Inverse of the second Townsend coefficient for a nozzle flow rate of 0.25, 1, and 2 grams per second as a function of the angle from the nozzle location and the potential of the body with respect to the plasma.

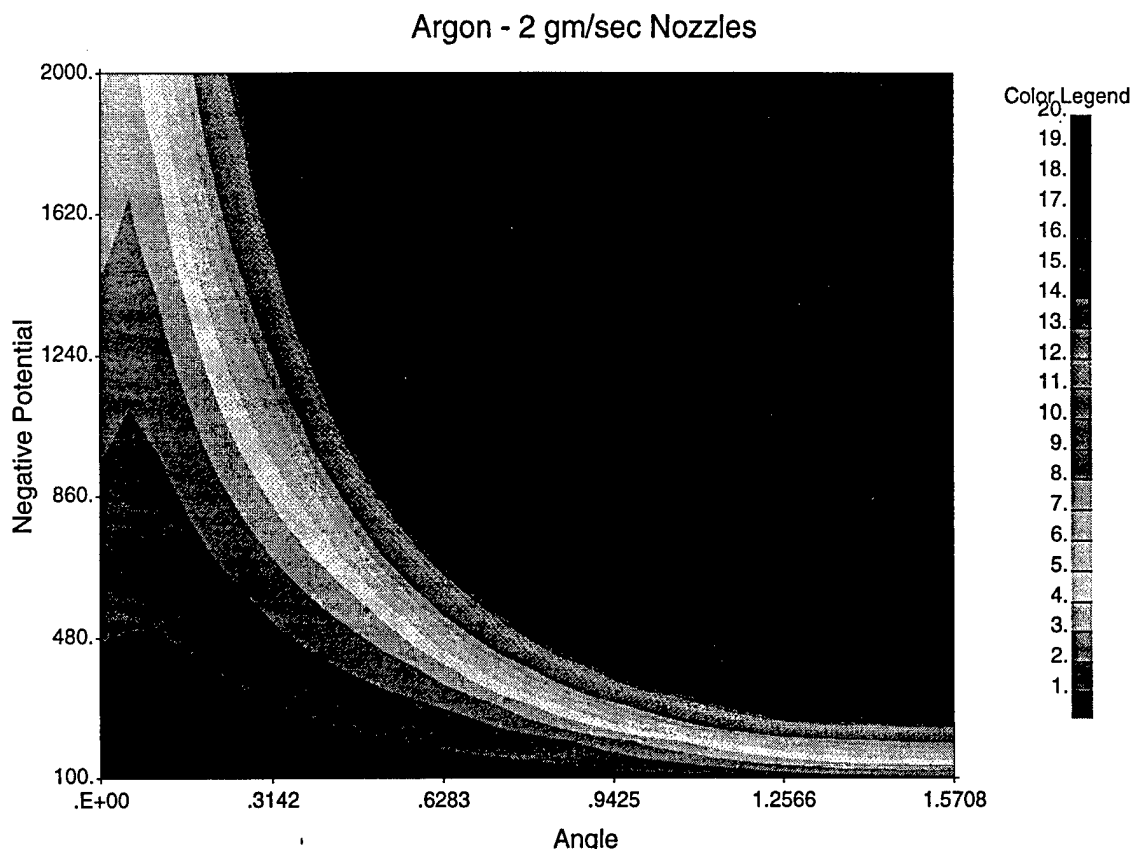


Figure 28 (c) Inverse of the second Townsend coefficient for a nozzle flow rate of 0.25, 1, and 2 grams per second as a function of the angle from the nozzle location and the potential of the body with respect to the plasma.

These results were presented at the SPEAR-3 Mockup Review Meeting, Arlington VA, 2 September 1992, and later at the 1992 American Geophysical Union (AGU) Fall Meeting, San Francisco CA, December 1992. It was strongly recommended that the flow rate be increased from the then baselined 0.5 grams per second per nozzle to 2 grams per second per nozzle. At the project meeting, similar recommendations on the flow rate were made by E. E. Kunhardt (on theoretical grounds), and by J. Antoniadis (based on Mockup Test results). The higher flow rate was adopted by the project.

7. SPEAR-3 Mockup Analysis - Floating Potential

The SPEAR-3 Mockup tests took place at Plum Brook Station, Sandusky, Ohio during July, 1992. The material in this chapter was presented at the Mockup Data Review in Arlington, VA, 2 September 1992.

DynaPAC calculations for the SPEAR-3 floating potential in space predict that about 40 percent of the bias potential applied to the sphere will appear (in a negative sense) on the rocket body (Figure 29). We have confidence in these results because the same techniques were able to match the floating potential of SPEAR-I (Figure 30). By contrast, the floating potentials observed in the Plum Brook chamber, in the presence of plasma, were typically near 70 percent of the applied potential (Figure 31). To maintain confidence in the DynaPAC predictions for the space environment, we must identify the factors causing the Mockup test results to be considerably more negative.

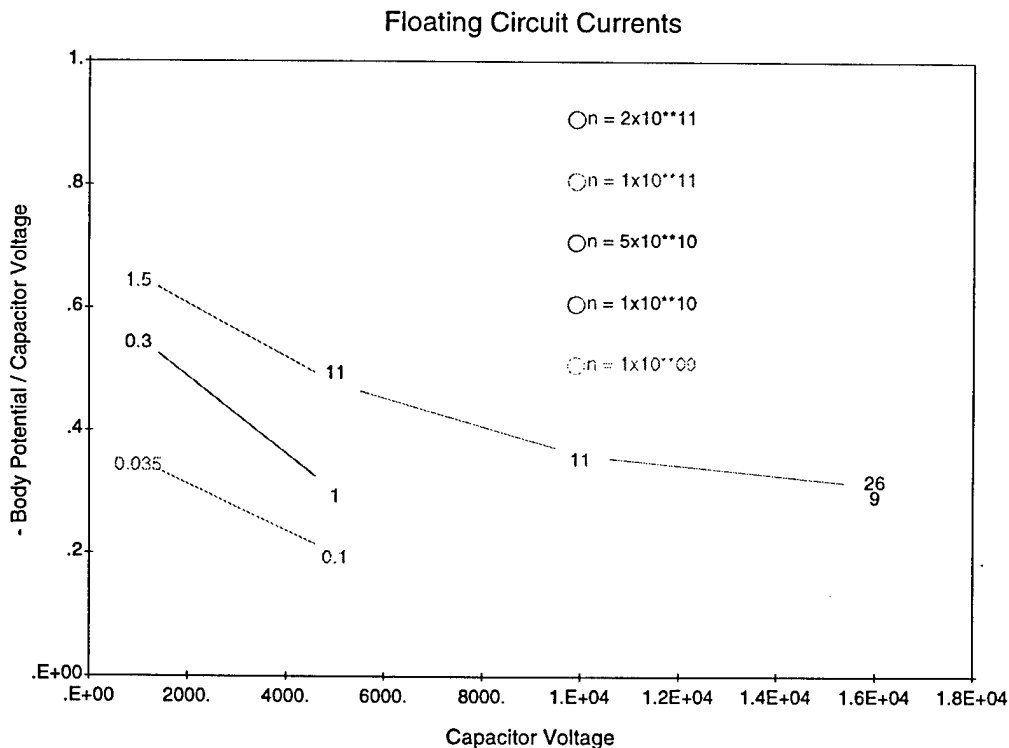


Figure 29. Floating circuit currents.

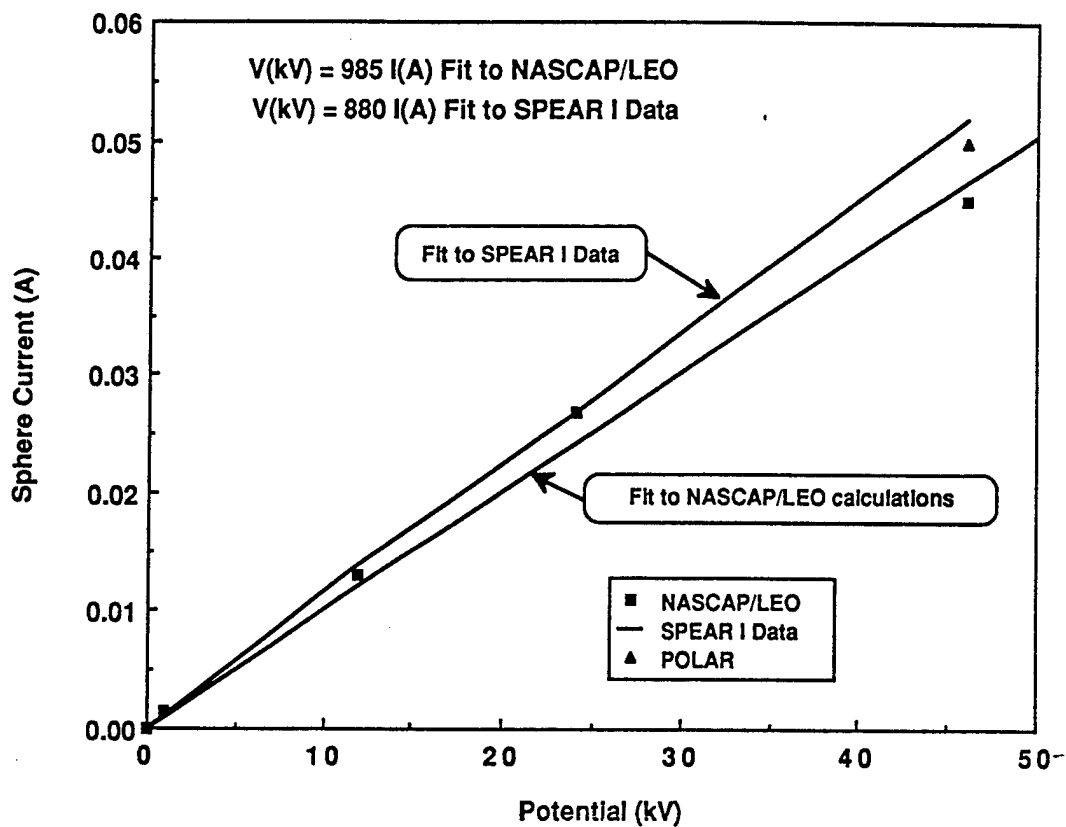


Figure 30. SPEAR I data.

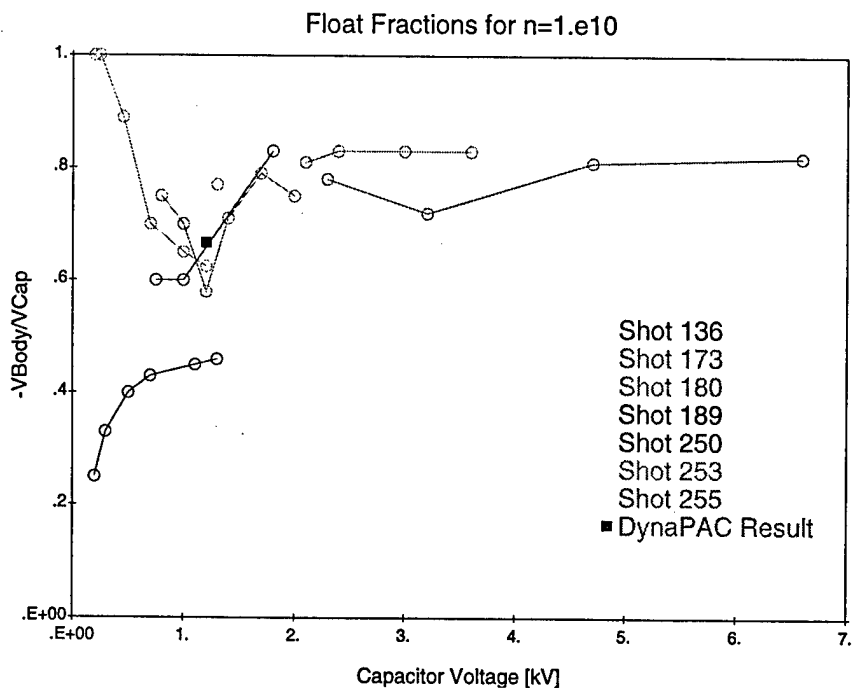


Figure 31. Float functions of 10^{10} m^{-3} .

7.1. Plasma Differences

The chamber plasma density was representative of space conditions, but was considerably warmer and had heavier ions (Table 6). We can identify three effects directly leading to a more negative floating potential:

Table 6

	Chamber	Space
Plasma Density [m^{-3}]	$10^{10} - 10^{11}$	(comparable)
Plasma Temperature	1 eV	0.1 eV
Ion Mass	40 amu	16 amu

- (a) The increased ion mass directly reduces incident ion current (by a factor of 1.6), so that the model must go more negative to increase ion current and decrease electron current to meet the floating condition.
- (b) The increased ion mass also reduces the velocity of ions striking the rocket surface, resulting in lower secondary electron emission.
- (c) The increased temperature results in higher current density. Since space charge density (at a given potential) is proportional to current density times the square root of mass, the space charge is increased (relative to space) by the square root of the temperature (a factor of 3). This reduces the size of the ion sheath. The smaller ion sheath directly reduces the ion current. Even more important, the smaller ion sheath is less effective at blocking electron flow into the sphere sheath. Both effects lead to a more negative floating potential.

Table 7 shows four DynaPAC calculations performed with only the plasma conditions changed relative to space.

Table 7.

Sphere Voltage	Body Voltage	Density	Sheath Radius	Current for B			Ion Current
				Body	Boom	Normal	
400	-800	1×10^{11}	0.7	6.8	1.9	6.0	0.9
2000	-4000	1×10^{11}	1.0	5.7	3.4	3.4	3.9
400	-800	1×10^{11}	0.8	0.40	0.21	0.35	0.3
1500	-4500	1×10^{11}	0.5	0.0	0.0	0.0	0.85

In the first three cases, the results indicate that an assumed floating potential of two-thirds negative is plausible, and this is reasonably close to the chamber results and considerably more negative than the space results. For the fourth case (which was experimentally nearly 80 percent negative), the calculation indicates a floating fraction considerably less than the assumed 75 percent. For this case (but not the other three), the ion sheath (Figure 32) is extremely large and totally chokes off the electron sheath.

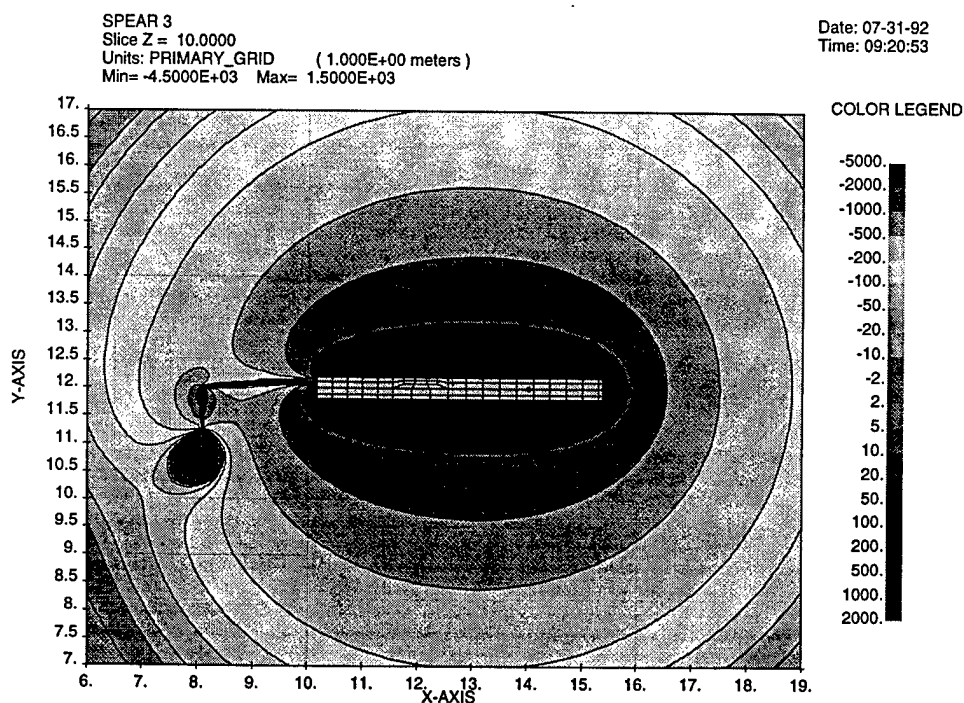
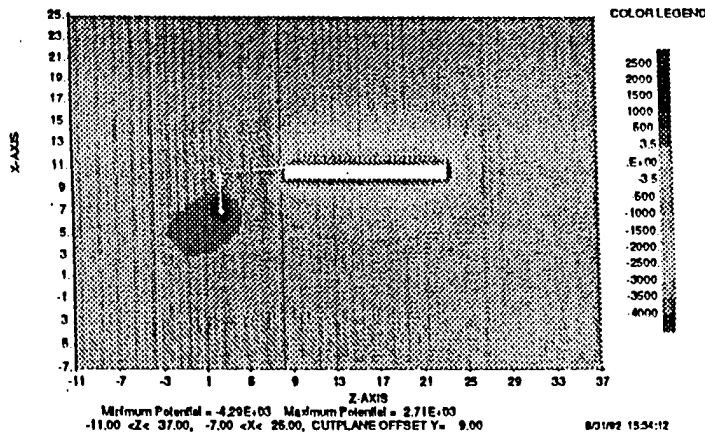


Figure 32. Ion sheath suppresses electron current.

7.2 Chamber Size Effects

The key to the fourth case listed above is that the ion sheath exceeds the size of the chamber. The metal chamber walls serve to confine the ion sheath so that it does not choke off the electron sheath. Figure 33(a and b) shows two NASCAP/LEO sheath calculations for potentials comparable to the fourth case above. With the chamber wall removed (b) the ion sheath engulfs the electron sheath. When the ion sheath is constrained by chamber walls (a) there is ample path for collection of electrons. This means that a more negative (relative to space) floating potential is needed to suppress electron collection by the sphere.

SPEAR 3 Sheath
Plumbrook Chamber B



SPEAR 3 Sheath
Without Chamber Wall

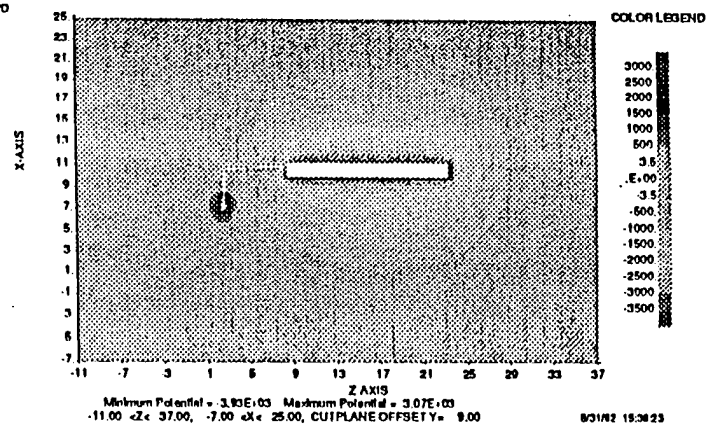


Figure 33. SPEAR 3 sheath with and without chamber wall.

7.3 Ionization Effects

At the vacuum level achieved in the Mockup tests (2×10^{-5} torr) ionization in the electron sheath can cause considerable increase in the sheath size. One-dimensional (radial) calculations show that, for parameters characteristic of the tests and realistic ionization cross-sections, ionization can roughly double the sheath radius, even if the ionization-enhancing effect of a magnetic field is neglected. The calculations indicate that the effect would be negligible if the neutral density were a factor of four lower. This ionization effect provides yet another factor making the Mockup floating potential more negative.

7.4 Sheath Breakdown

Prior to installation of the "Disruptor Plate" the sphere sheath invariably broke down when high voltage was lied under plasma conditions. A DynaPAC simulation was performed to simulate the time development of the breakdown. In the simulation, a 1200 volt bias was lied to the sphere at time zero, leading to a body potential (as in vacuum) of -80 volts. The potential then developed in accordance with collection from a plasma with density $1 \times 10^{10} \text{ m}^{-3}$. The body collected ions in the usual way. The sphere (and boom) collected (a) electrons tracked inward (in the presence of a 0.55 gauss magnetic field) from the sphere sheath, and (b) electrons created by ionization within the sheath (collected instantly). The space charge in the sphere sheath consisted of the tracked electrons and the slowly outward moving ions created within the sheath.

Figure 34 shows the time development of the body potential, which increased roughly linearly in time to nearly -800 volts at 80 microseconds. Figure 35 shows the time development (plotted as a function of body potential) of the components of current to the rocket. The sheath electron current decreases roughly linearly as the rocket goes negative, decreasing the sphere potential. However, the rate of ion production increases nonlinearly after an initial drop. This is because the sphere sheath, which was initially fairly compact (Figure 36a) due to screening by the circulating electrons (Figure 37), is swelled by the presence of slow ions (Figure 36b).

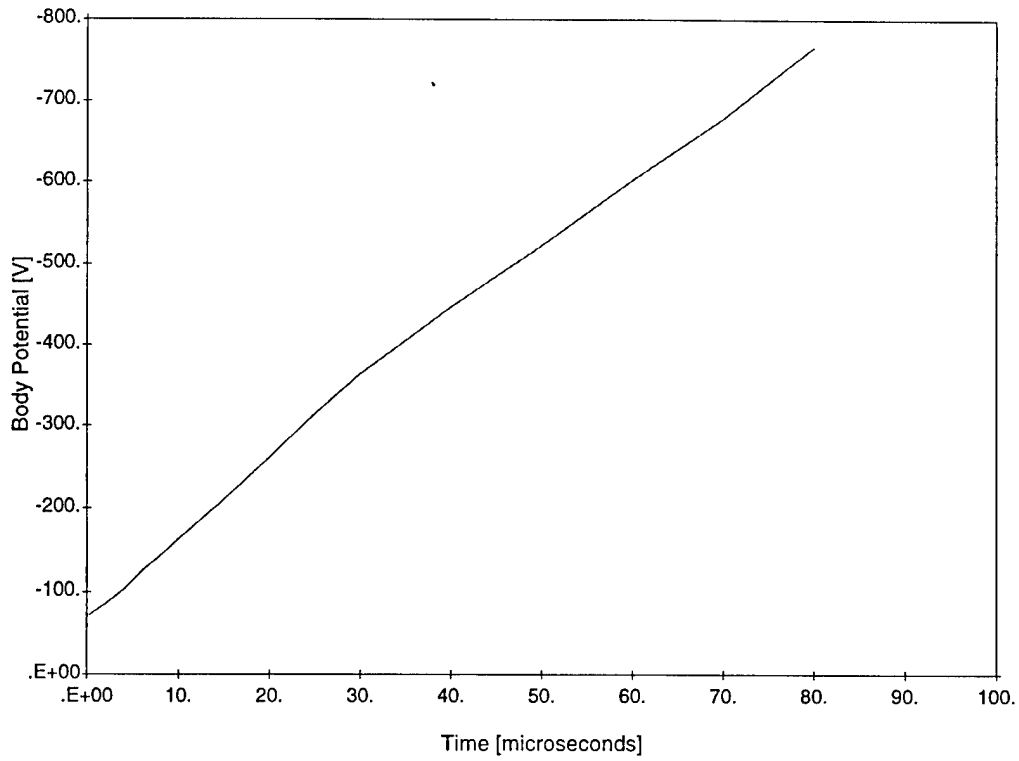


Figure 34. Body potential versus time.

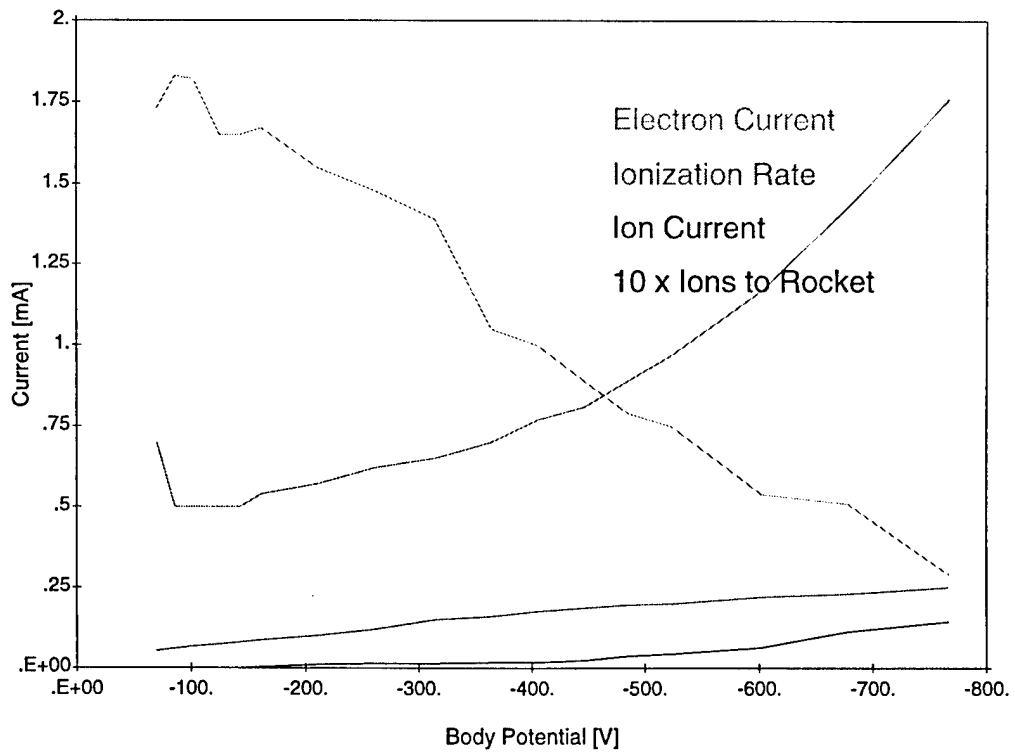


Figure 35. Current voltage relations.

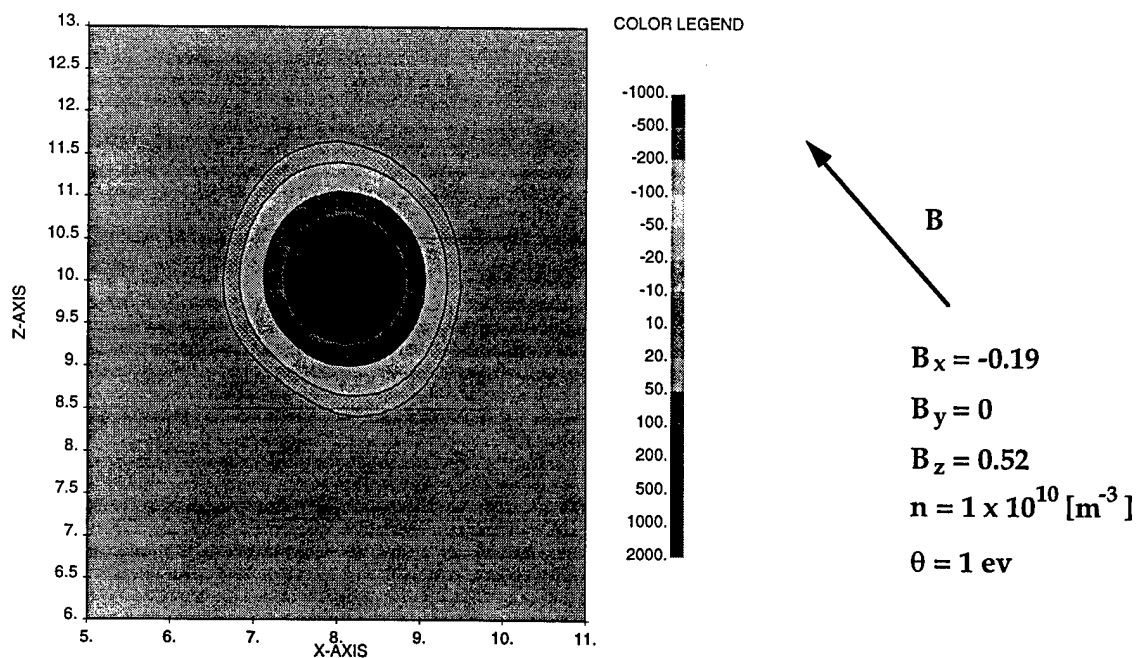


Figure 36a. Initial sphere sheath.

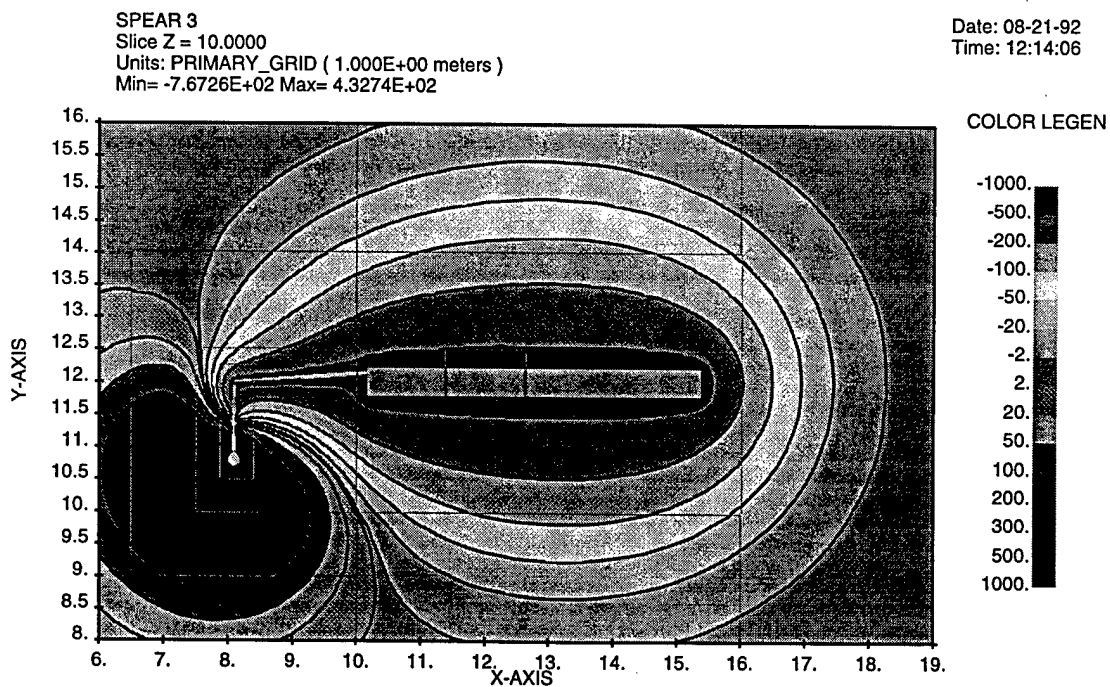


Figure 36b. Ion and electron sheaths.

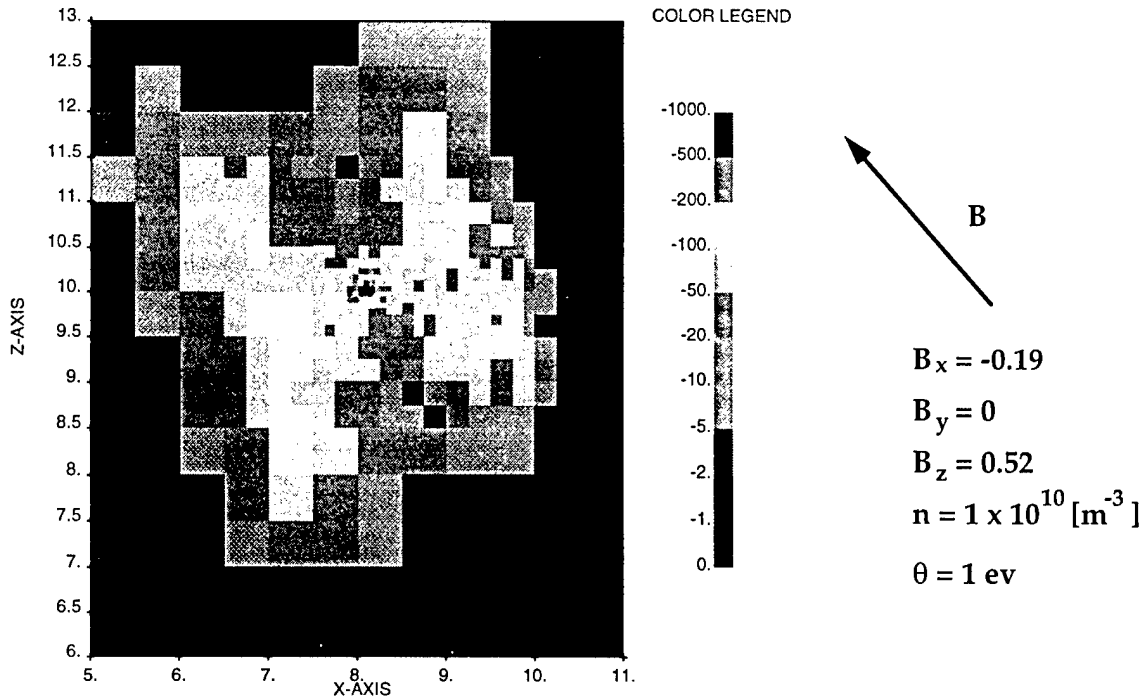


Figure 37. Circulating electrons.

While there is much to criticize about the way this calculation was done, we feel that it provides good insight into the breakdown invariably observed in the chamber. The breakdown mechanism is swelling of the sphere sheath due to ionization of the ambient neutrals by accelerated plasma electrons. If the chamber vacuum were an order of magnitude better, these breakdowns would not have taken place.

7.5 Breakdown Quenching by the Disruptor Plate

The artifice which brought success to the Mockup tests was placing a grounded "Disruptor Plate" in the path of the circulating electrons. The rationale was that electrons would no longer make many $E \times B$ orbits, reducing the rate of ion production.

We performed DynaPAC and NASCAP/LEO calculations, with and without the disruptor plate, to examine the mechanism of discharge suppression. We were led to the conclusion that the proposed mechanism was not valid because:

- (a) Few electrons made multiple $\mathbf{E} \times \mathbf{B}$ orbits in any case;
- (b) Many electron orbits missed the disruptor plate;
- (c) By Gauss's law, the total sheath electron charge could not be much affected by interruption of the $\mathbf{E} \times \mathbf{B}$ orbits;
- (d) Calculations showed that the initial rate of ion production was not significantly affected by the presence of the disruptor plate.

We then proposed that the primary mechanism of discharge quenching by the disruptor plate was purely electrostatic. The plate provided a ground plane near the outer edge of the sheath, which prevented the sheath from swelling, as the ions would be neutralized by image charges on the disruptor plate. Calculations indicated that the disruptor plate reduced the effective charge of ions by about two-thirds.

We also noted that vacuum conditions were apparently better during the test series with the plate, as evidenced by improvement in the vacuum breakdown behavior of the body sheath (which cannot be attributed to the plate's presence).

We concluded that the suppression of sphere breakdown was due primarily to the electrostatic effect of the plate in preventing the sheath from swelling, secondarily to improvement in vacuum conditions, and only in a minor way to perturbation of electron orbits by the plate.

8. Statistical Analysis of CHAWS Flight Data

The purpose of the CHAWS experiment is to determine the current to a high potential object in the wake of another object. The collected current depends on the geometry of the two objects, the distribution of potentials on the two objects, the plasma environment, the orientation of the objects with respect to any motion of the plasma, and the presence and direction of sunlight. Our hope is that an examination of the role of each of these parameters in the WSF/CHAWS system will provide insight into the role of these parameters in other systems.

8.1 Relevant Parameters

First, we consider how many of the above parameters are directly measured and how the rest are related to directly measured quantities.

The geometry of the CHAWS system is fixed and known.

The distribution of potentials depends on the applied bias, the floating potential of WSF, and the magnitude of $\mathbf{v} \times \mathbf{B} \cdot \mathbf{L}$ at each location referenced to WSF. The applied bias is directly measured. The floating potential at the location of the CHAWS ram side detector along with the plasma environment and the WSF orientation determine the distribution of counts in energy in the ram side detectors. The energy at which one-half of the incoming particles are rejected can be used to estimate the floating potential. The floating potential is determined by $\mathbf{v} \times \mathbf{B} \cdot \mathbf{L}$ referenced to the shuttle, the plasma environment, the presence and direction of sunlight, the applied bias, and the attitude of WSF and the shuttle. The most important parameter in determining the floating potential is $\mathbf{v} \times \mathbf{B} \cdot \mathbf{L}$ referenced to the shuttle. This quantity is computed from the known shuttle velocity, the measured magnetic field, and the vector distance from WSF to the engine bells. While other surfaces may contribute to current collection, it is assumed that the one value adequately estimates the average. Variations in $\mathbf{v} \times \mathbf{B} \cdot \mathbf{L}$ across WSF are small enough that they can be ignored.

The plasma environment consists of several flowing low-temperature ionic components, low temperature electrons, possible high energy contributions at the highest magnetic latitudes, and ions created in the shuttle environment. No

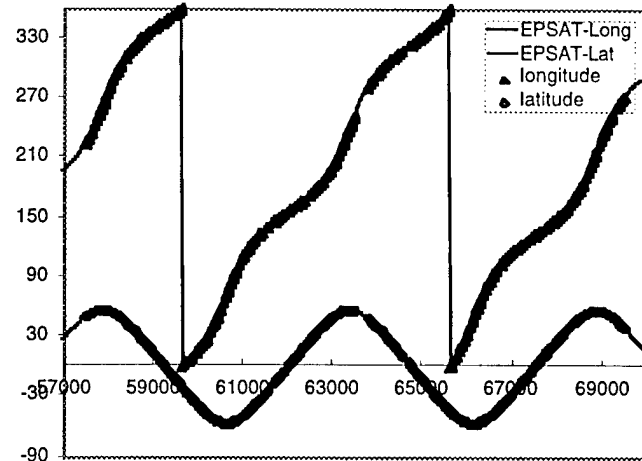
obvious auroral events were observed. It would be desirable to have separate measurements of the ionospheric O⁺, ionospheric H⁺, and shuttle generated plasma components. At present, the only parameter consistently available from the ram side detectors is the overall plasma density. The plasma temperature is available for a large fraction of the measurements, but is ignored in the least square fit as it is not available for a significant fraction of the measurements.

The orientation of the system components with respect to the ram direction is known. The most important quantity is the tilt of WSF with respect to the ram direction. This is the angle about the axis through the center of WSF perpendicular to the axis that passes through CHAWS. During one period, the wag (the angle about the axis through the center of WSF that passes through CHAWS) becomes significant. Note that the shuttle orientation plays a role in the determination of $\mathbf{v} \times \mathbf{B} \cdot \mathbf{L}$. We ignore other orientational information as less important.

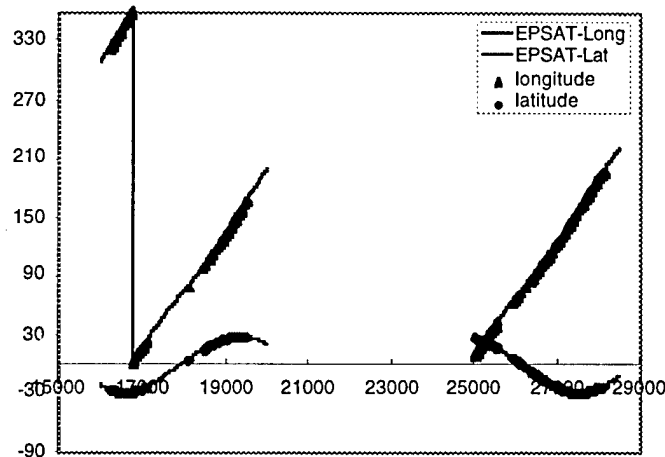
When the CHAWS probe is sunlit and negatively biased, an electron photocurrent on the order of microamperes is generated. For present purposes, we use the sun-WSF angle and eclipse times to estimate the influence of photocurrent.

8.2 Parameters Available From Models

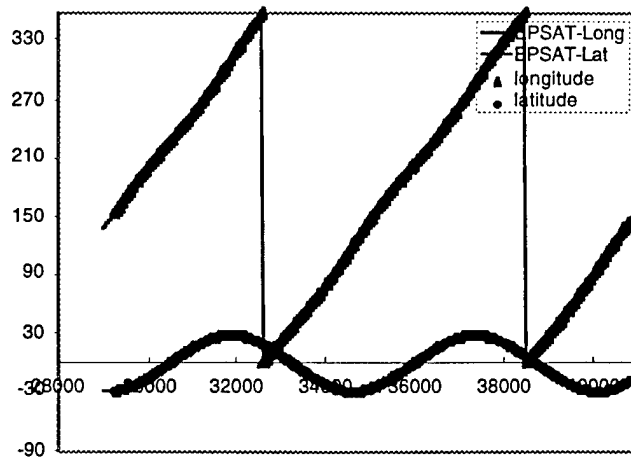
We use the EPSAT computer code to reinforce our confidence in measured quantities and to estimate quantities that are not measured or are difficult to determine from the flight data. Figure 38 compares the spacecraft location as measured and as determined by EPSAT's orbit generator. The orbit parameters used are given in Table 8. The model orbit adequately follows the actual orbit. Figures 39 through 41 show the ionospheric plasma environment as computed by EPSAT using the IRI-90 model extended to higher altitudes. Figures 41 and 42 compare the model plasma density and temperature with the measured plasma density and ion temperature. Figure 42 shows the spacecraft geomagnetic attitude. Auroral charging is expected only above 65° geomagnetic latitude.



GMT on day 39 of 1994 (sec)



GMT-53000 on day 256 & GMT on day 257 of 1995 (sec)



GMT on day 258 of 1995 (sec)

Figure 38. Spacecraft location as measured and as determined by EPSAT's orbit generator.

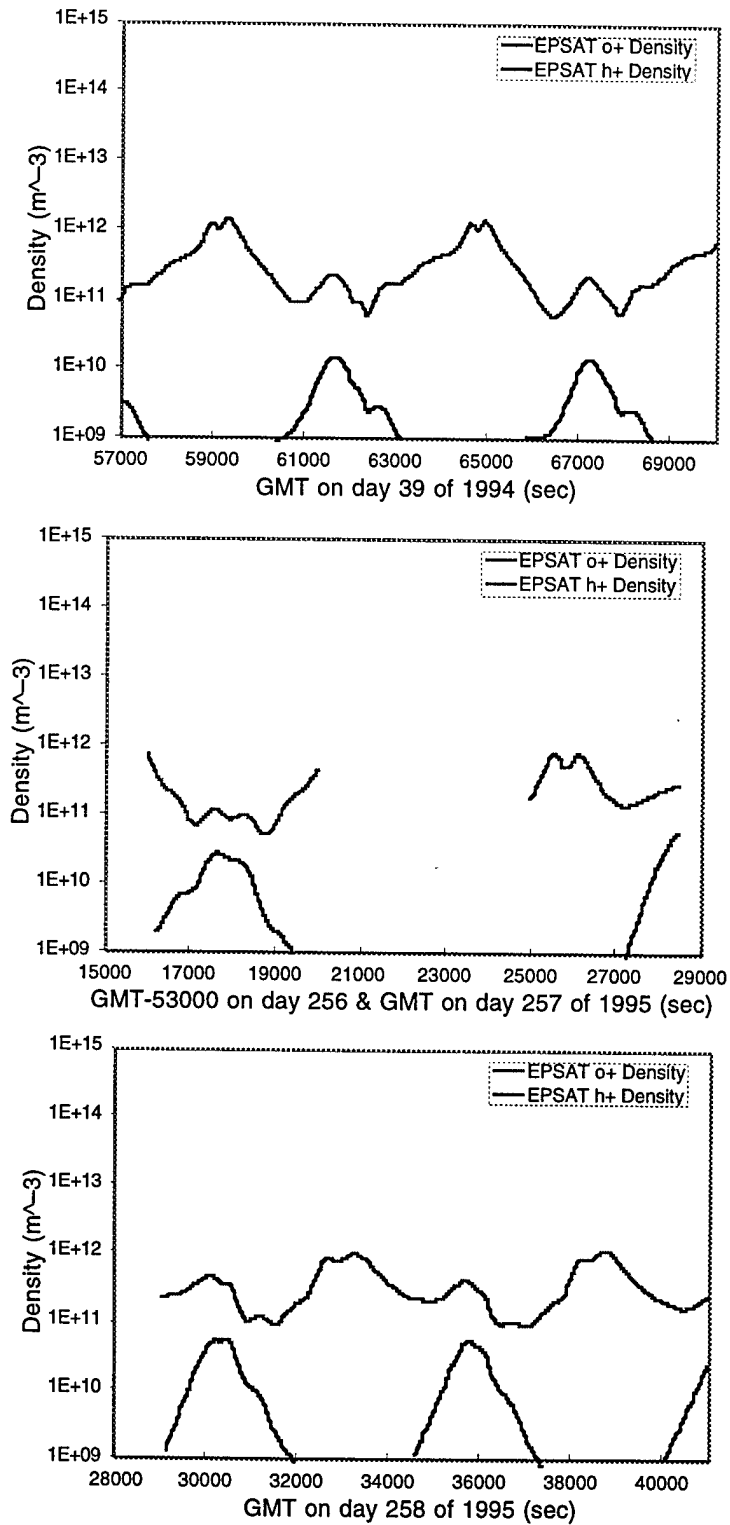


Figure 39. Ionospheric plasma environment. Densities of the two major constituents as computed by EPSAT from the IRI-90 model.

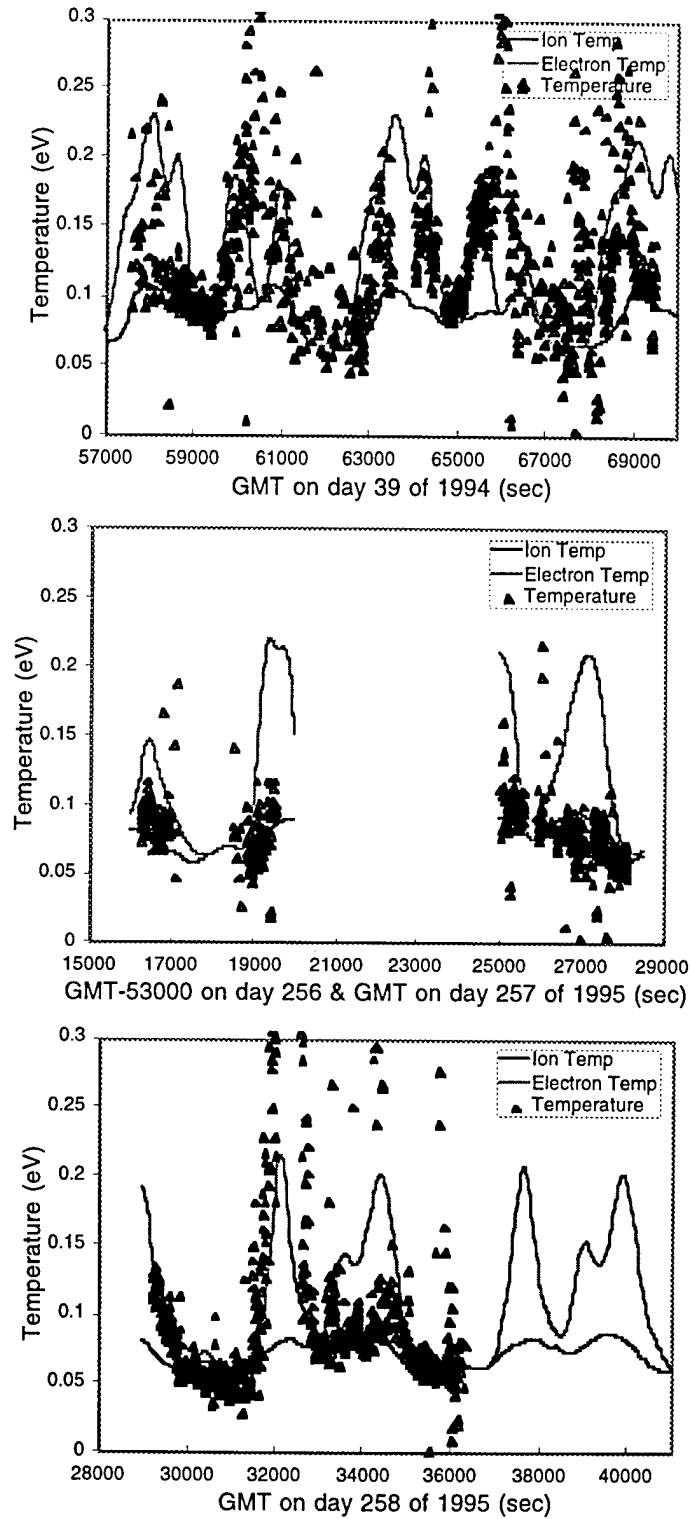


Figure 40. Ionospheric plasma environment. Component temperatures as computed by EPSAT from the IRI-90 model.

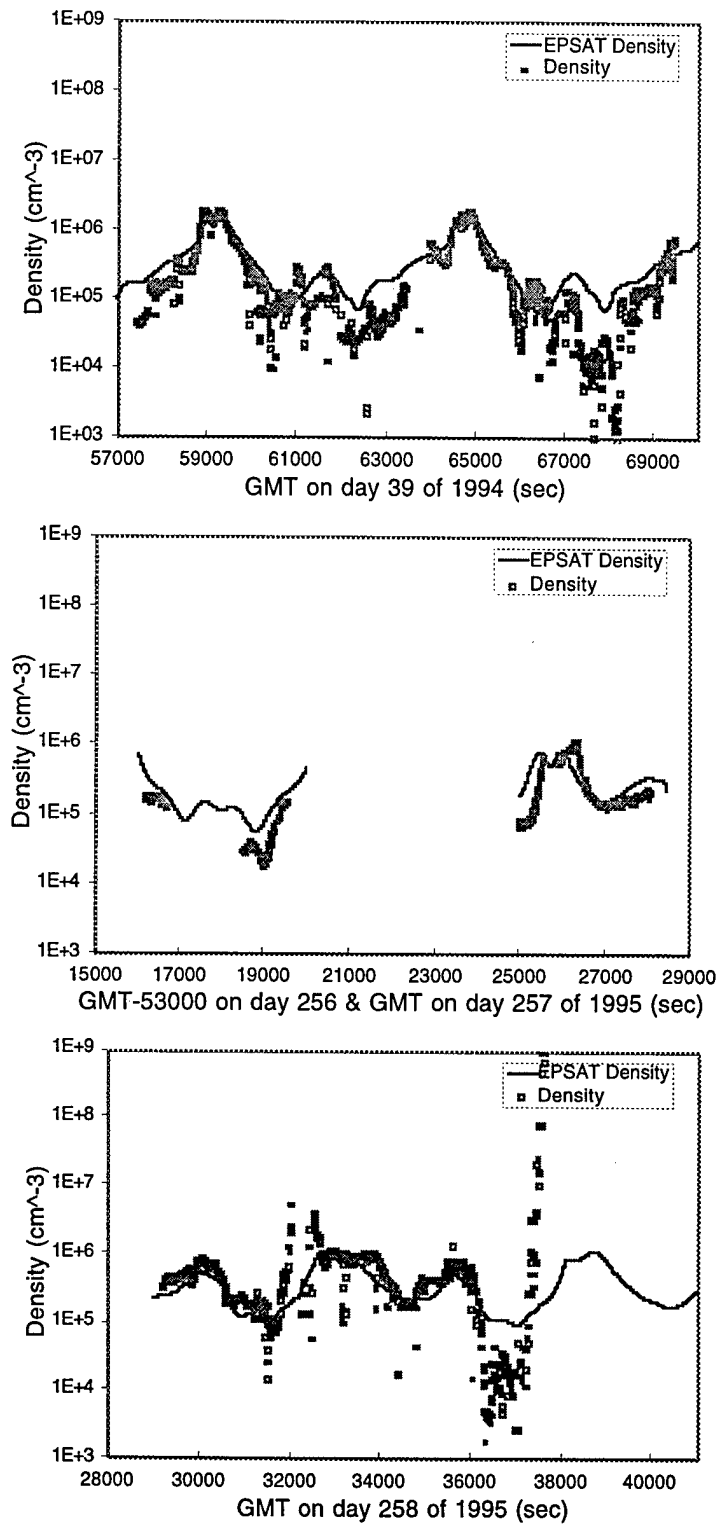


Figure 41. Ionospheric plasma environment. Density as determined from the IRI model with the ram density as measured by the ram side CHAWS detectors.

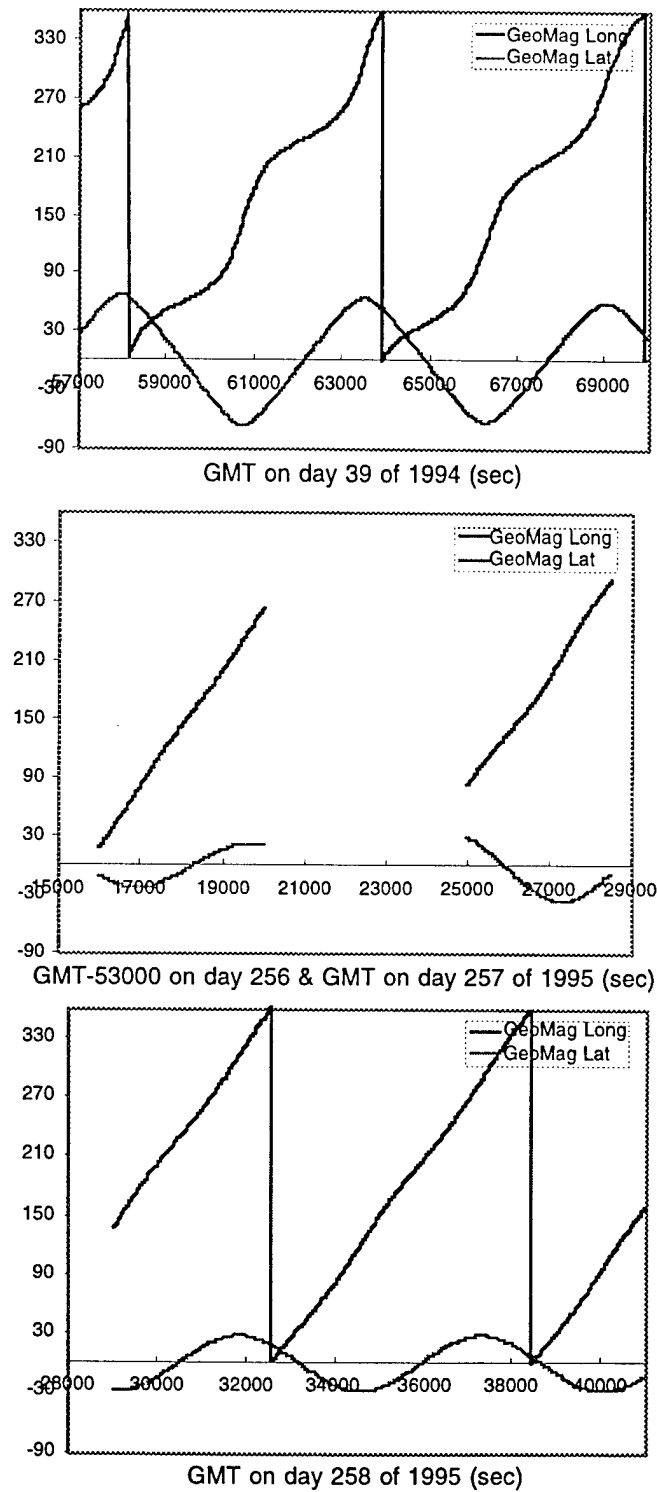


Figure 42. Geomagnetic latitude and longitude of the shuttle. Auroral currents are most likely at the highest geomagnetic latitudes.

Table 8. Model Orbit Parameters

	Flight 1	Free Flight	Flight 2
Effective Time	1994, Day 39 04:03:10	1995, Day 256 10:28:25	1995, Day 258 06:00:37
Apogee	360	409	352
Perigee	345	401	342
Inclination	56.99	28.47	28.47
Mean Anomaly	217.28	63.52	217.08
Right Ascension	195.16	2.5	349.51
Argument of Perigee	275.40	295.51	281.36

8.3. Measured Quantities

We used the chunks program to determine a number of quantities for the time period of interest. We show data for four different time periods. The first time period is Day 39 of 1994 from 57300 s to 70000 s GMT, dedicated CHAWS time during Flight 1. The second time period is Day 256 of 1995 from 69200 s to 72600 s GMT, during free flight. The third time period is Day 257 from 25000 s to 28200 s GMT, during free flight. The second and third time periods are shown together. The fourth time period is Day 258 from 29000 s to 41000 s GMT, dedicated CHAWS time during Flight 2.

The data extracted from the databases is shown in Figures 43 through 54. This includes some not used in the following analysis. The process used to extract this information is described in the Appendix.

Figure 43 shows the Orbiter attitude for Flight 1 and the attached portion of Flight 2. The Orbiter attitude was used to control the attitude of WSF. Note that the pitch over maneuver from 63000 s to 63500 s during the first flight changed the WSF floating potential by about 4 V. The maneuver at 32000 s during the second flight placed the wake side probe in the ram. The maneuver at 37000 s placed the WSF in the wake of the shuttle. The RMS arm was used to move WSF into the ram flow for measurements taken after 40000 s.

Figure 44 shows the WSF attitude. The ram angle is the unsigned angle between the ram direction and the normal to the WSF disk. The tilt is the primary indicator of how much the probe is tilted into the ram flow. Non-zero wag values indicate an increase of exposure to the ram flow. Even at the largest excursions of 10 degrees, this is a secondary effect as indicated by the fact that the ram angle and the absolute value of the tilt closely track. During the free flight period the WSF orientation was nearly constant.

Figure 46 shows the value of $\mathbf{v} \times \mathbf{B} \cdot \mathbf{L}$ for Flight 1 and the attached portion of Flight 2. The value of $\mathbf{v} \times \mathbf{B} \cdot \mathbf{L}$ varies by 16 V during the measurement periods. When $\mathbf{v} \times \mathbf{B} \cdot \mathbf{L}$ is positive, we expect the engine bells to remain grounded and the disk to be negative with respect to the plasma. When $\mathbf{v} \times \mathbf{B} \cdot \mathbf{L}$ is negative, we expect WSF to remain within a volt of plasma ground and the shuttle to be negative with respect to the plasma.

The potential at which one-half of the incident ram ions are repelled, shown in Figure 47, is an indication of the disk potential at the location of the CHAWS ram side detectors. The energy determined from the inboard and outboard detectors is different from that determined from the center detectors, due to orientation effects. The half-point energy roughly follows $\mathbf{v} \times \mathbf{B} \cdot \mathbf{L}$. The peak in $\mathbf{v} \times \mathbf{B} \cdot \mathbf{L}$ at about 61000 s is matched by a comparable rise in the ram half-point energy, while the energy measurement is only modestly affected by the strong dip in $\mathbf{v} \times \mathbf{B} \cdot \mathbf{L}$ at 63000 s. The rise in $\mathbf{v} \times \mathbf{B} \cdot \mathbf{L}$ from 0 to 5 volts following 67000 s is well matched by a rise in ram half-point energy from about 3 to 8 volts. The variation during free flight may reflect small variations in the potential across the disk or, more likely, is related to how variation in orientation changes the measurement. The variation during the third time period does not track $\mathbf{v} \times \mathbf{B} \cdot \mathbf{L}$ as well. The two figures for each time period use different vertical axis scales. The full scale figures in Figure 48 are included to illustrate the difficulty of interpreting this measurement.

The estimated floating potential, shown in Figures 49 and 50, is the nominal drift energy of oxygen minus the half-point potential shown in Figures 47 and 48. The nominal drift energy is 4.57 eV times the square of the cosine of the ram angle of the WSF disk.

For the fitting calculations and Figures 41 and 42, the floating potential (Figures 49 and 50), plasma density (Figure 51), and ion temperature (Figure 52) calculated from the detector most nearly aligned with the ram direction is used.

The currents, shown in Figure 54, are determined by CHUNKS using a stencil. For each step, current measurements made by the appropriate channels are averaged. Measurements are included only if there are more than six consecutive good frames where a good frame is one with two or more steps with the voltage over 2.5 V and the voltage is increasing from step to step.

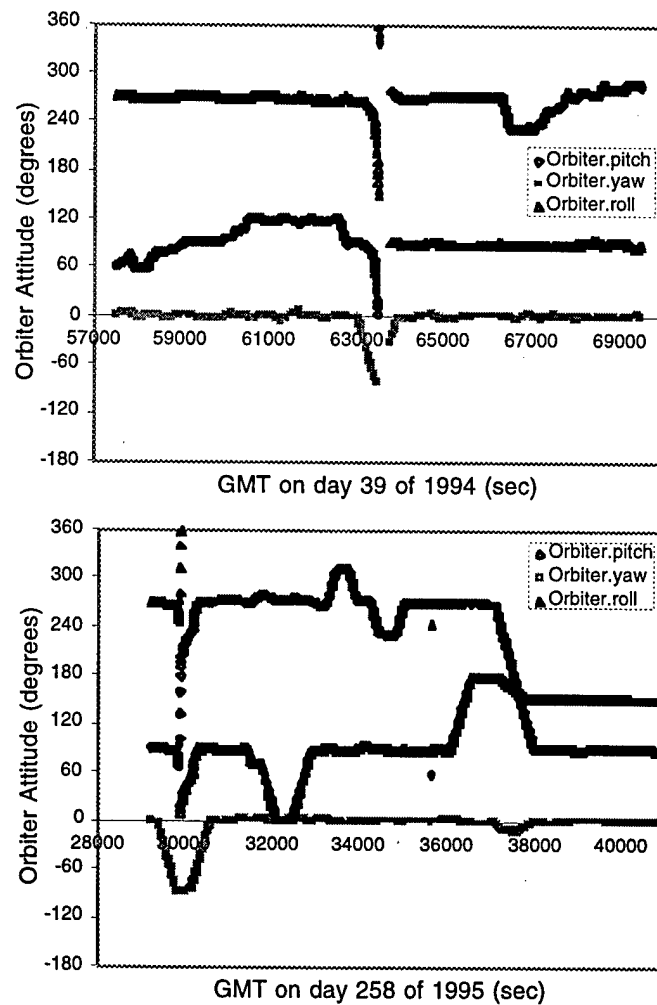


Figure 43. Orbiter attitude for Flight 1 and the attached portion of Flight 2.

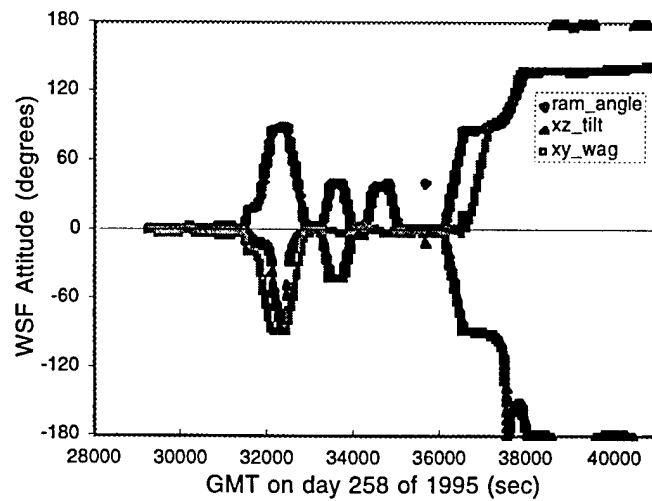
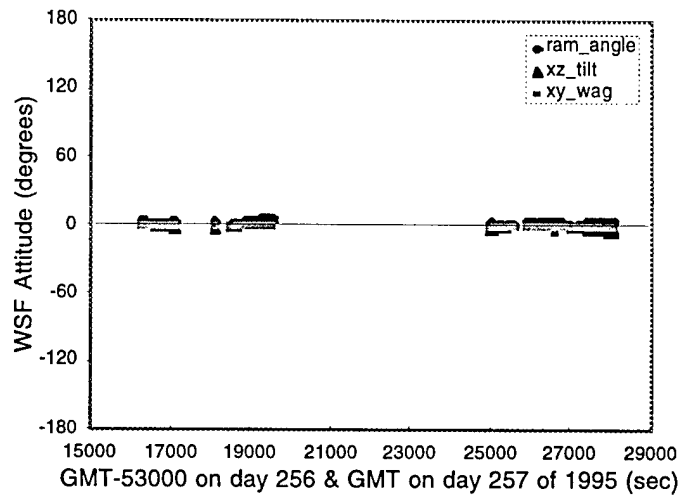
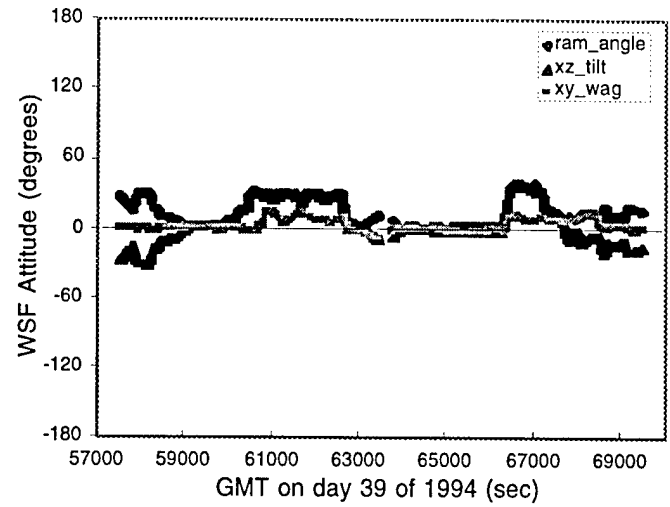


Figure 44. WSF attitude.

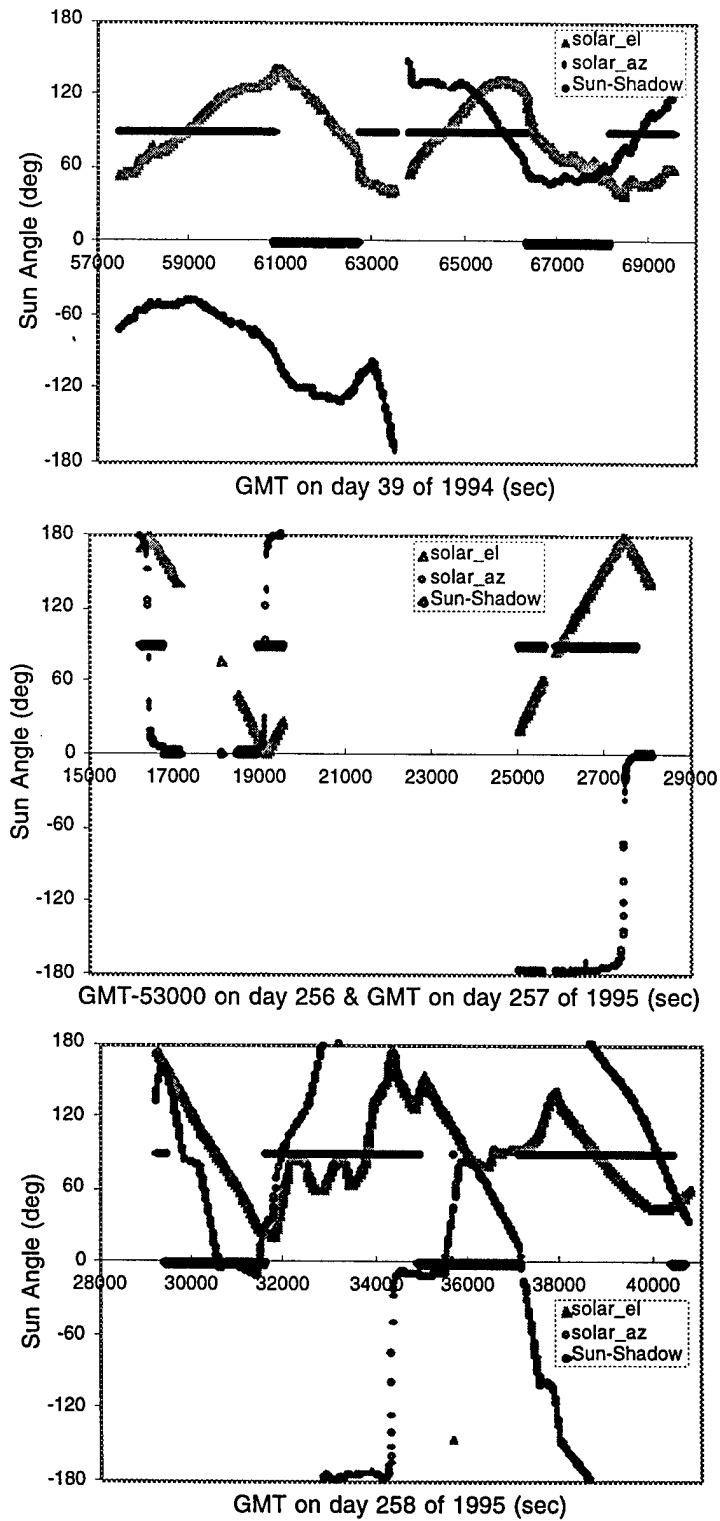


Figure 45. The sun angle.

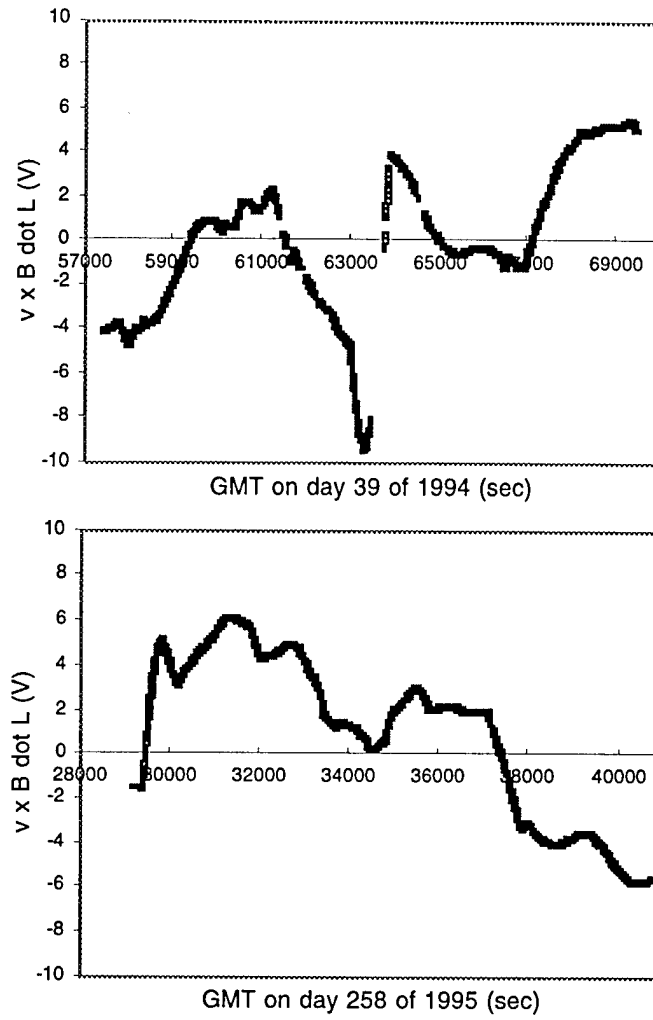


Figure 46. $\mathbf{v} \times \mathbf{B} \cdot \mathbf{L}$ for Flight 1 and the attached portion of Flight 2.

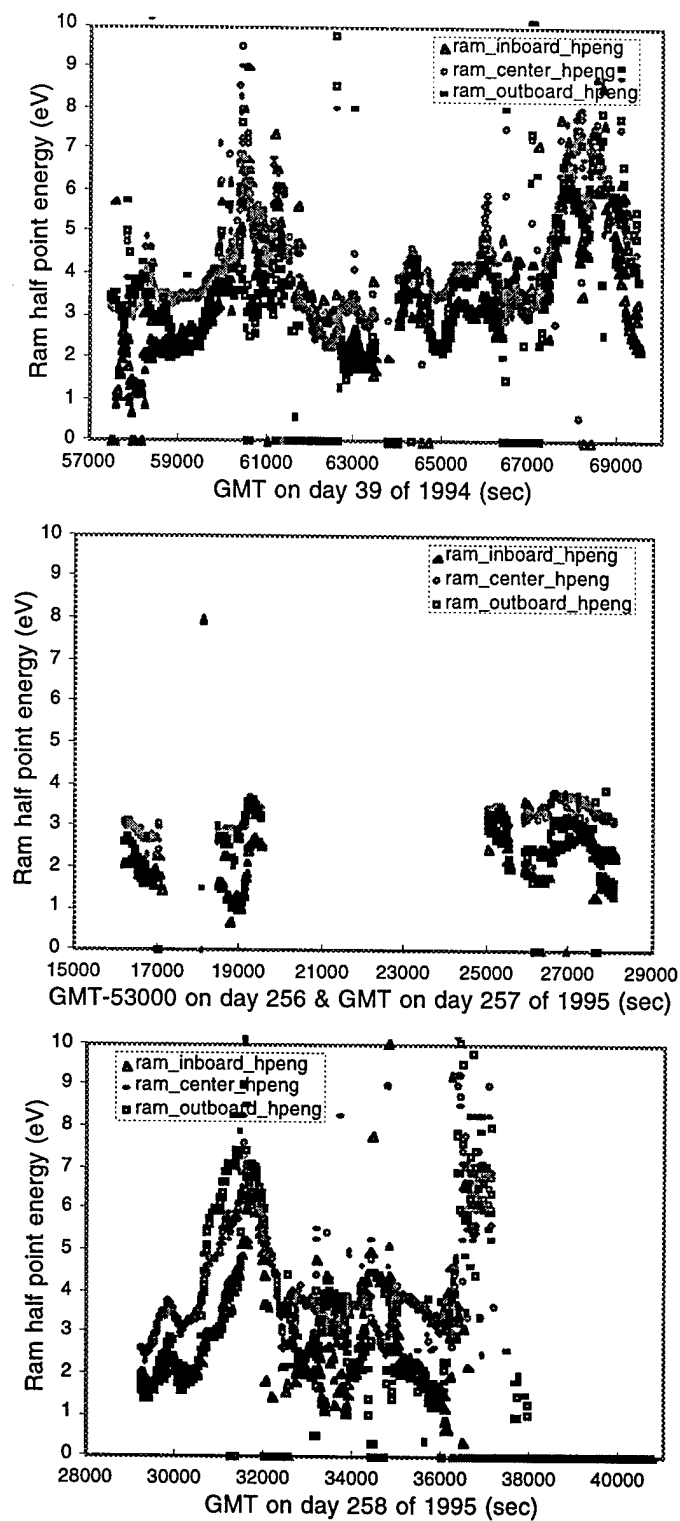


Figure 47. Potential at which one-half of the incident ram ions are repelled.

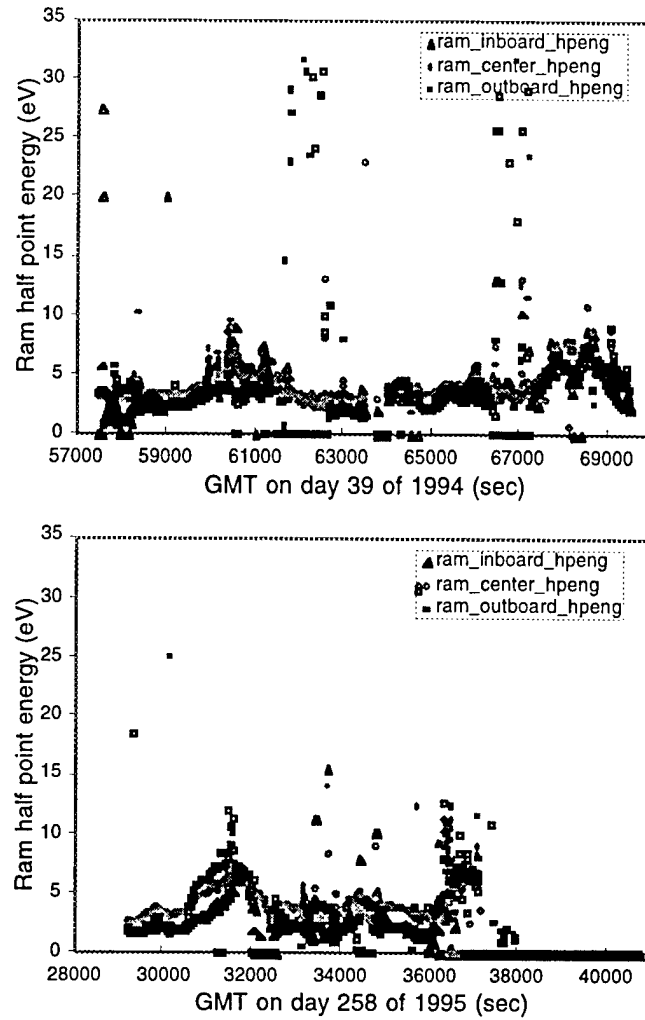


Figure 48. Potential at which one-half of the incident ram ions are repelled, full scale.

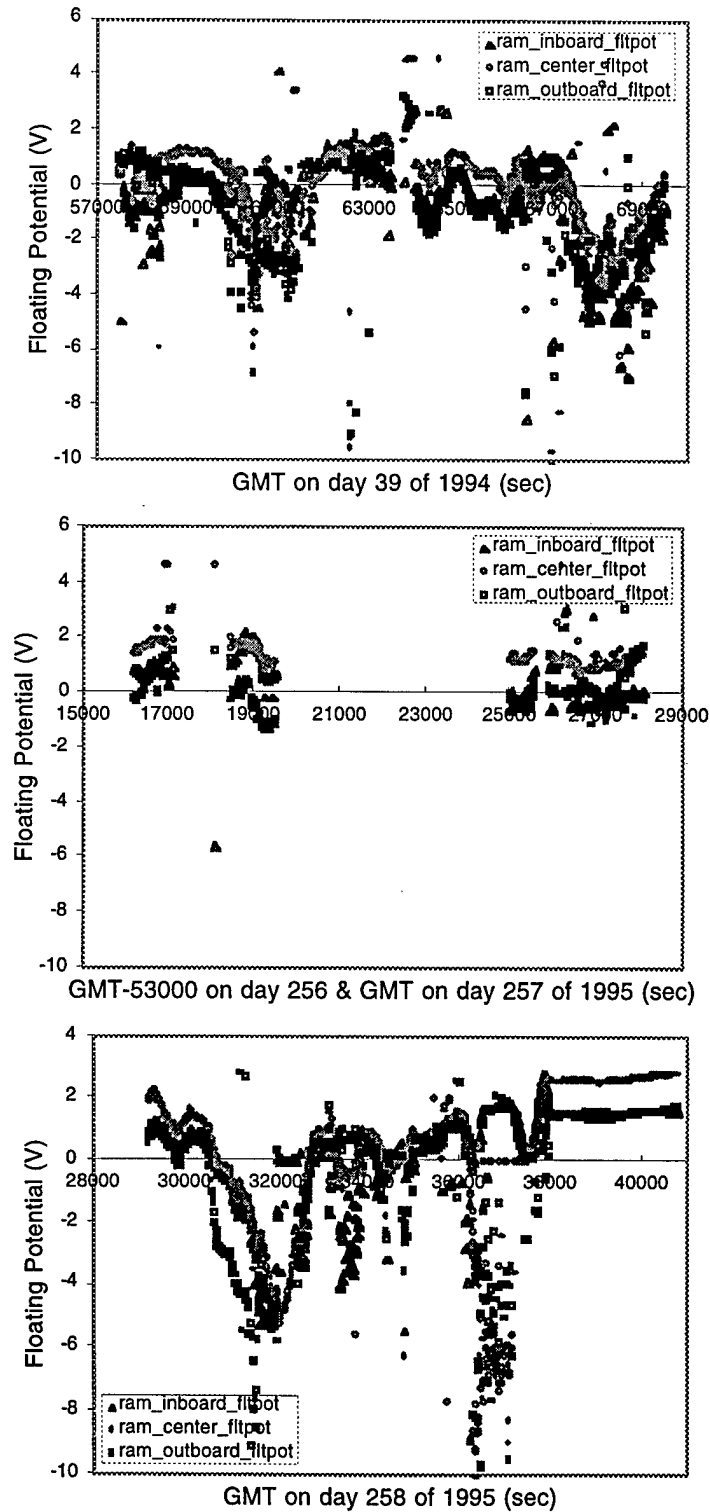


Figure 49. Estimated disk floating potential.

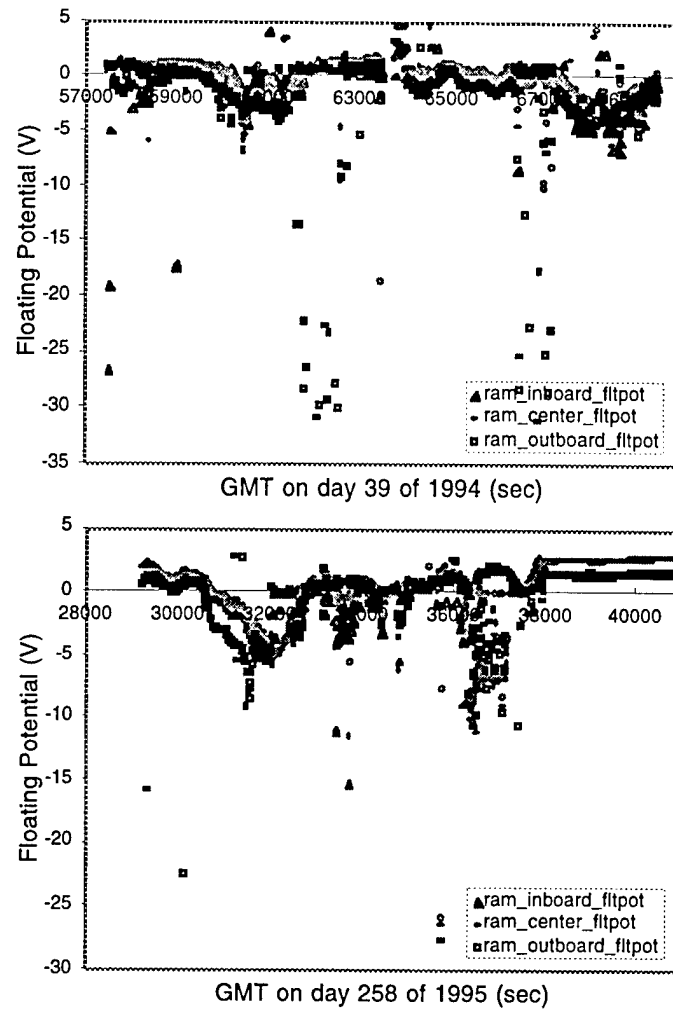


Figure 50. Estimated disk floating potential, full scale.

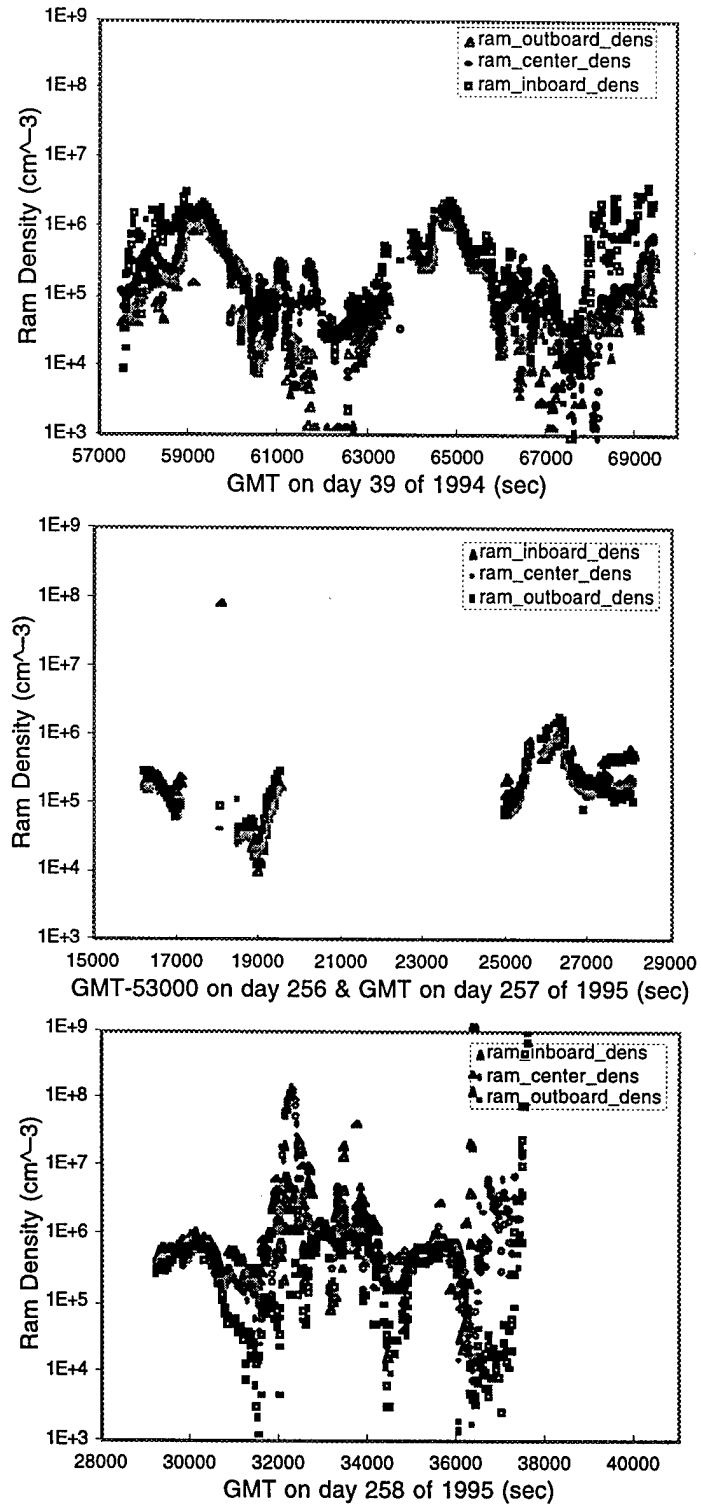


Figure 51. Density as measured by the ram side detectors.

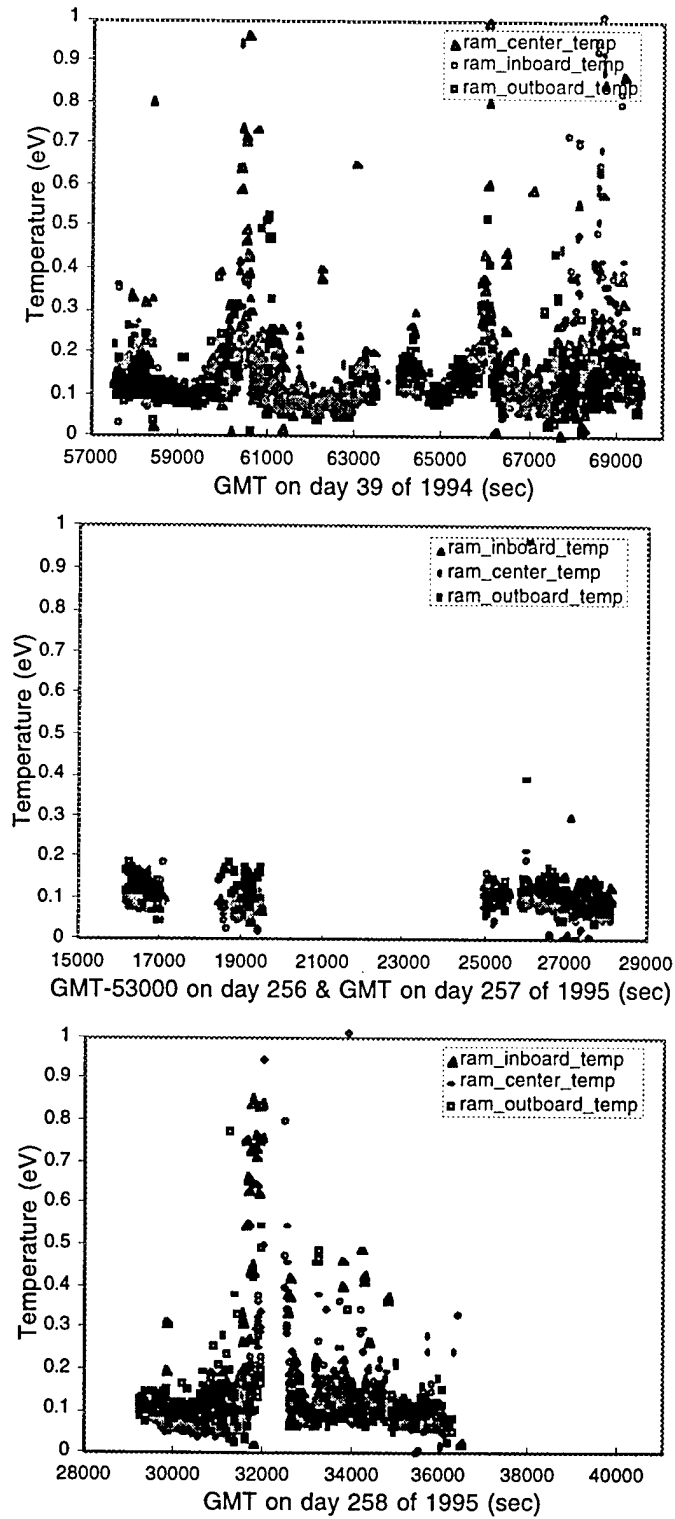


Figure 52. Ion temperature as measured by the ram side detectors.

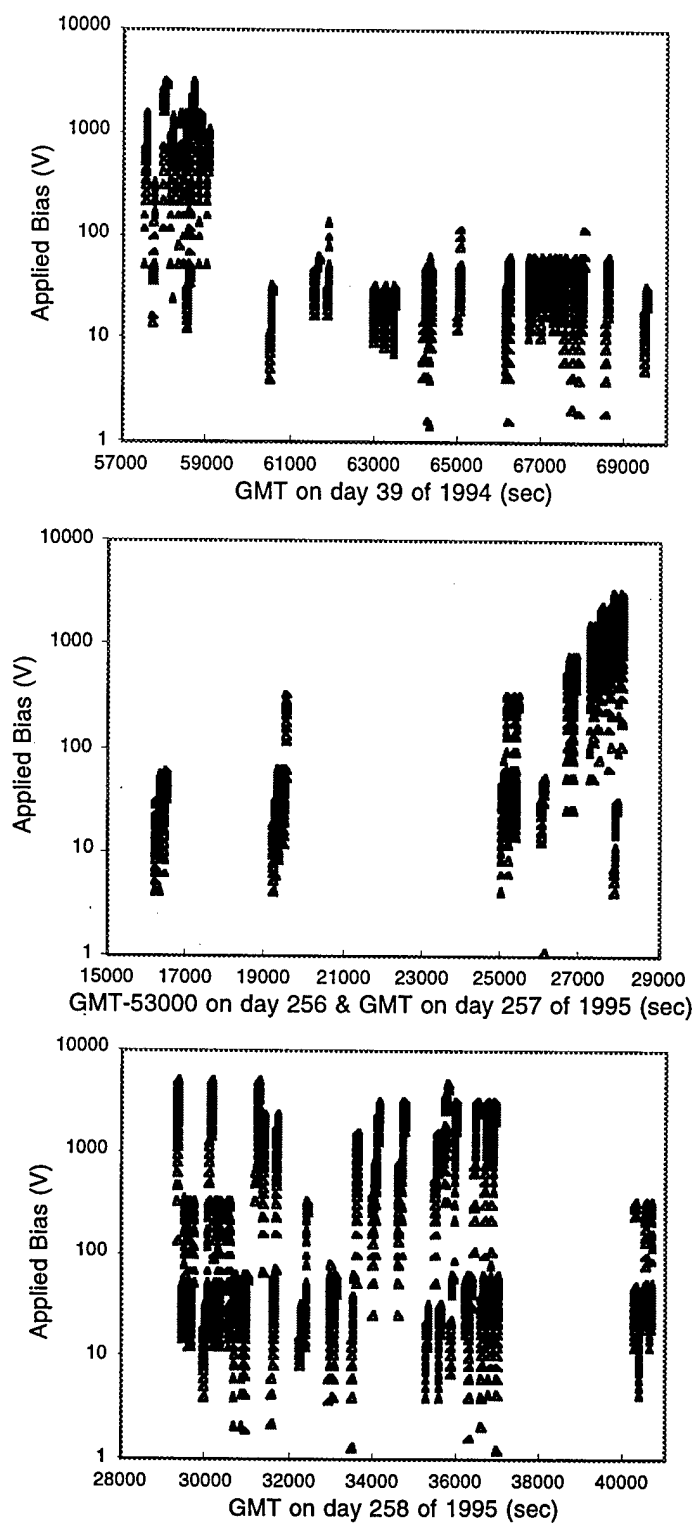


Figure 53. Applied potential.

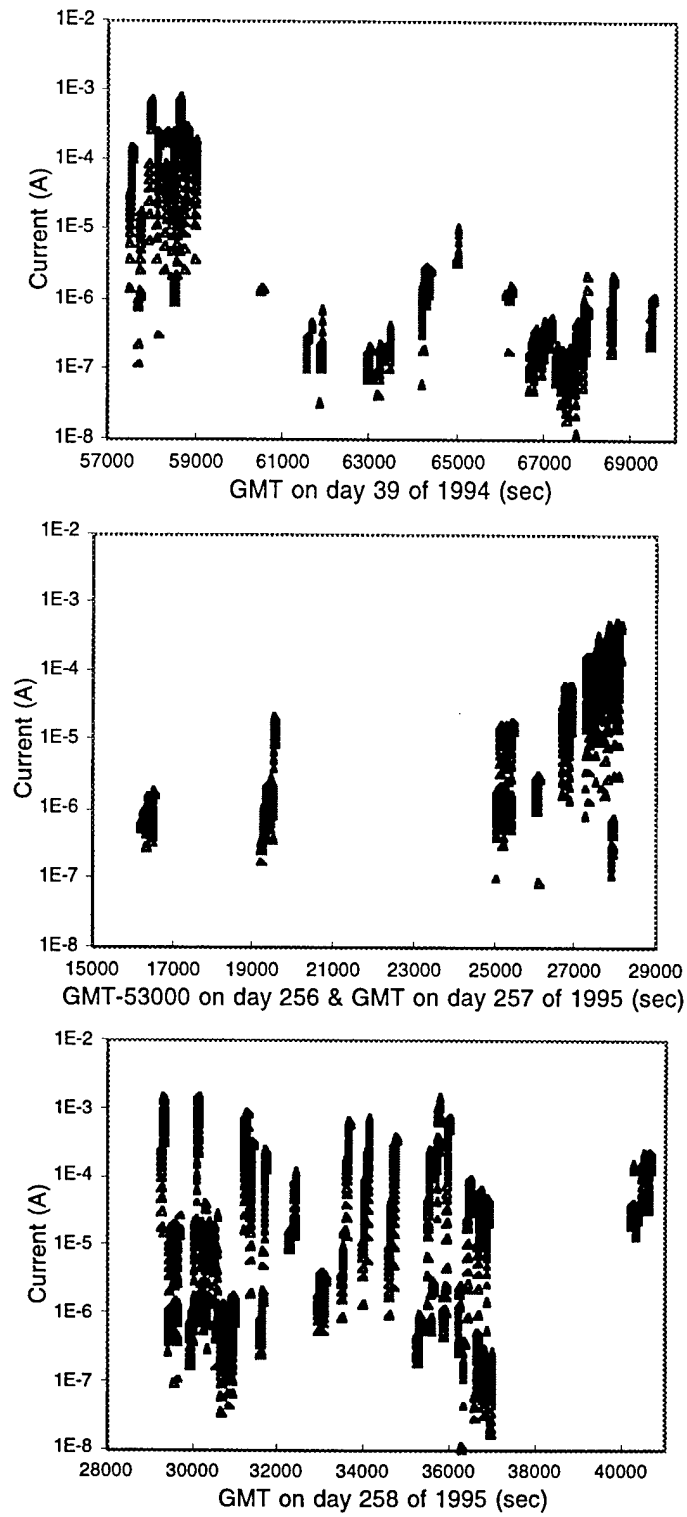


Figure 54. Collected current.

8.4 WSF Floating Potential

The floating potential is physically determined by $\mathbf{v} \times \mathbf{B} \cdot \mathbf{L}$ referenced to the shuttle, the plasma environment, the presence and direction of sunlight, the applied bias, and the attitude of WSF and the shuttle. Of these, the most important parameter in determining the floating potential is $\mathbf{v} \times \mathbf{B} \cdot \mathbf{L}$ referenced to the shuttle. This quantity is computed from the known shuttle velocity, the measured magnetic field, and the vector distance from WSF to the engine bells. While other surfaces may contribute to current collection, it is assumed that the one value adequately estimates the average. Variations in $\mathbf{v} \times \mathbf{B} \cdot \mathbf{L}$ across WSF are small enough that they can be ignored. If this understanding is correct, the floating potential would be a simple function of $\mathbf{v} \times \mathbf{B} \cdot \mathbf{L}$.

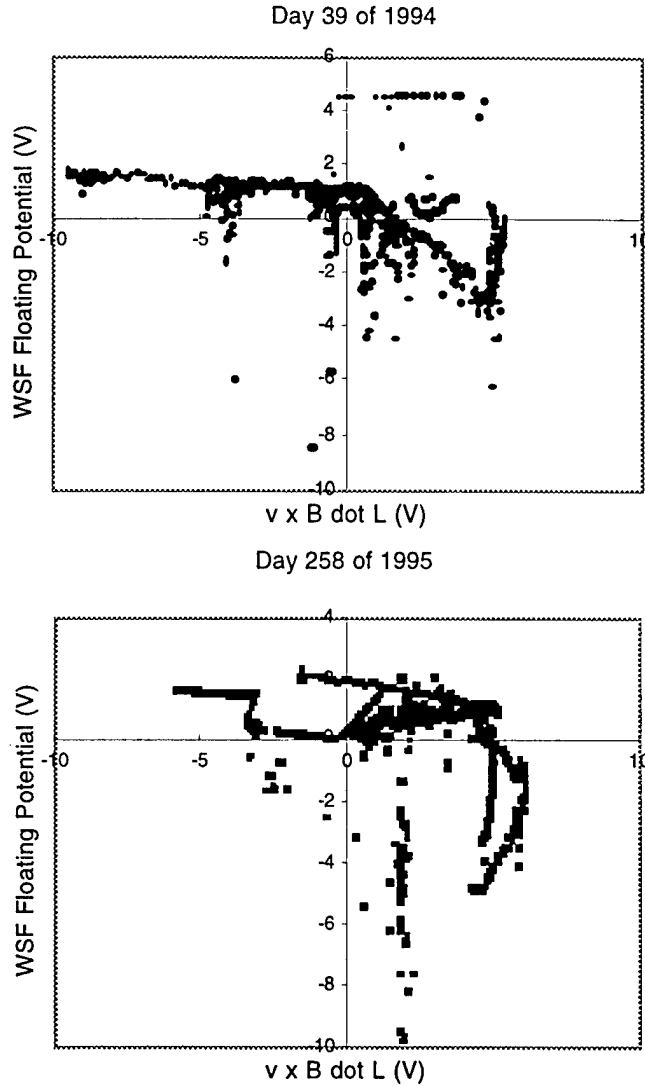


Figure 51. WSF floating potential as determined by CHUNKS from the half-point energy of the ions incident to the ram-side detectors as a function of $\mathbf{v} \times \mathbf{B} \cdot \mathbf{L}$.

8.5. Current Measurements

To gain a sense of the importance of each of the parameters, Figures 52 through 59 show the collected current as a function of the applied bias, plasma density, tilt, WSF floating potential and for the low potential measurements, sun-disk angle. 40 V is the dividing line between high and low potential measurements. From these figures, it is clear that the applied bias is the most important parameter. The potential measurements show a slight increase in current with plasma density. Dependence on tilt and WSF floating potential are much smaller.

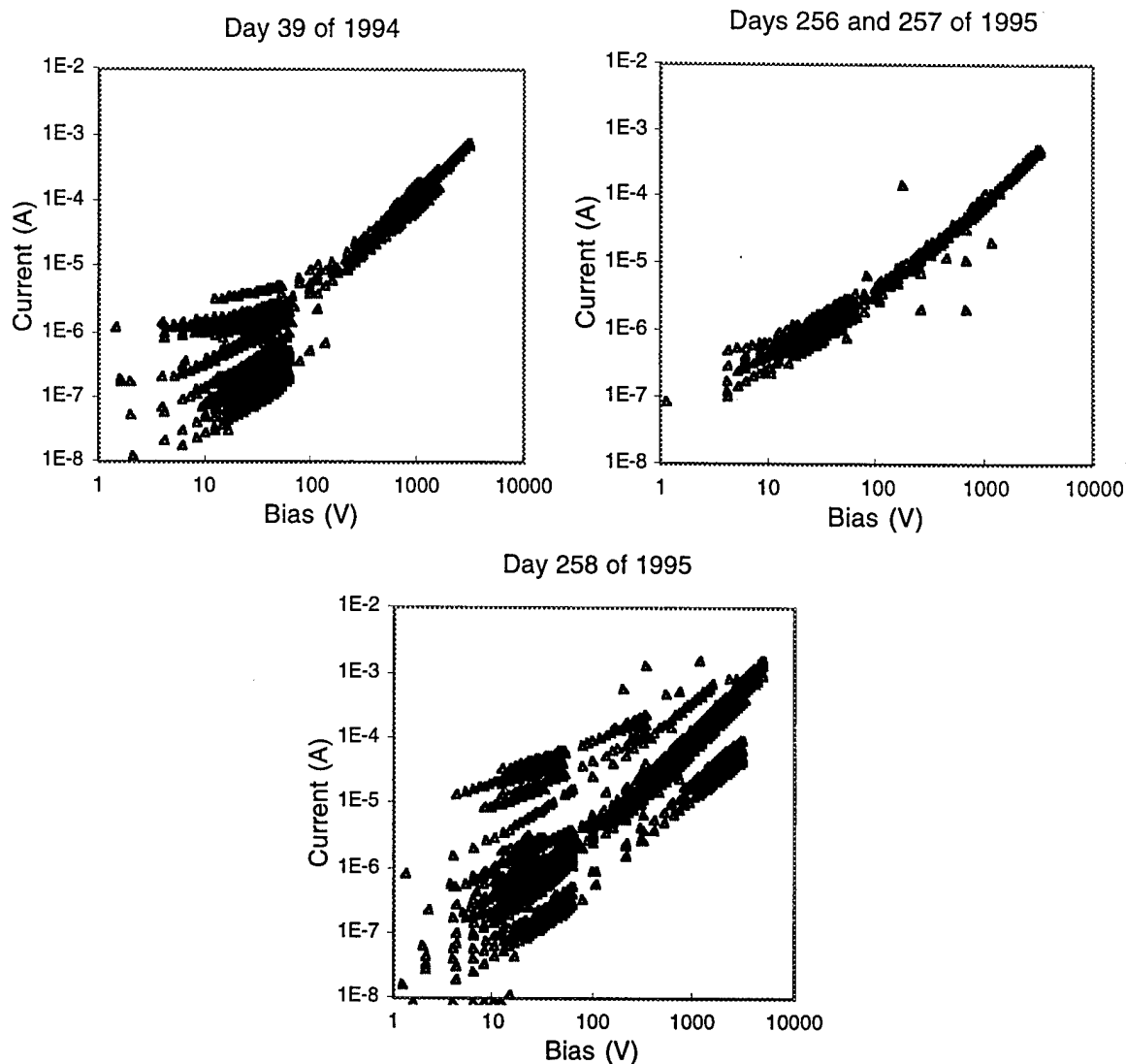


Figure 52. Collected current as a function of applied bias. The measurements for day 258 fall into three groups. The top set were taken while the probe was in the ram flow. The bottom set were taken while WSF was in the wake of the shuttle.

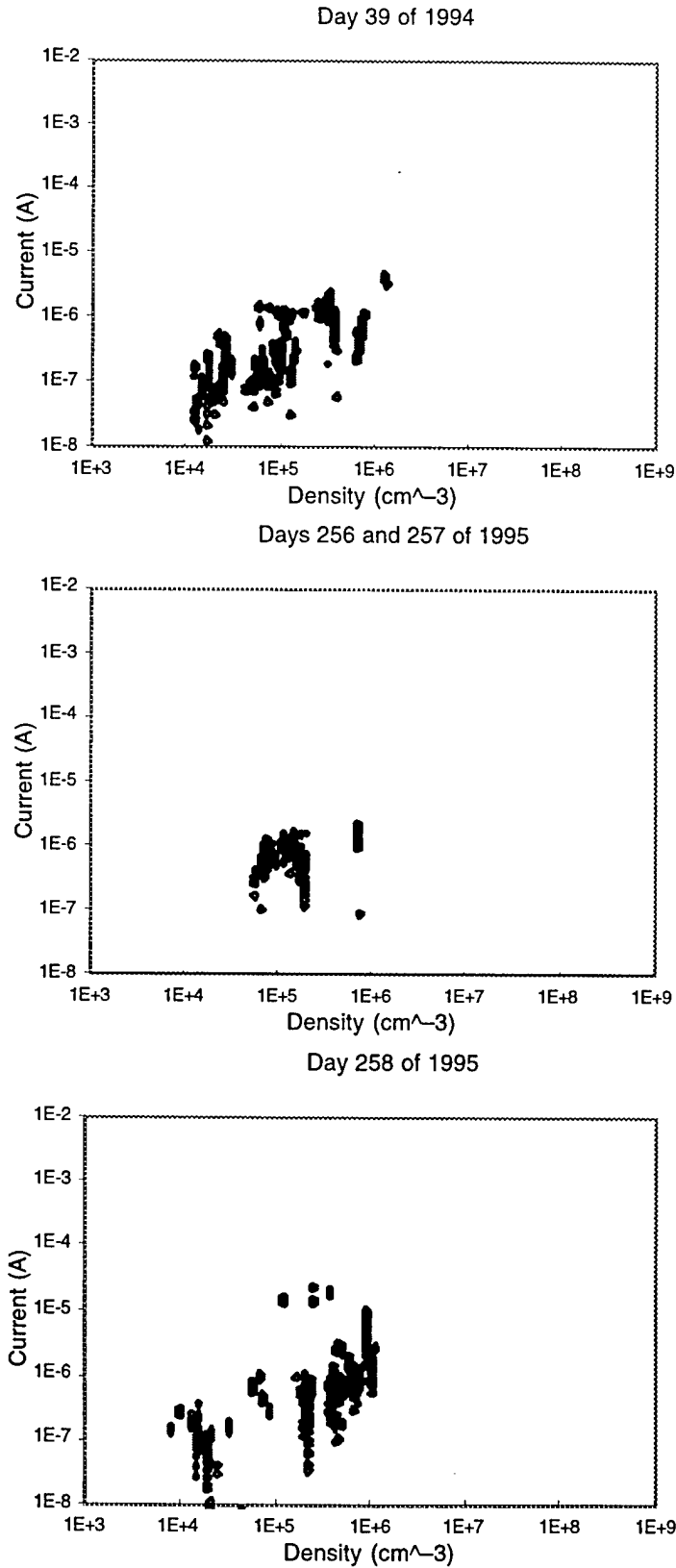


Figure 53. Collected current as a function of plasma density for low (under 40 V) potential measurements.

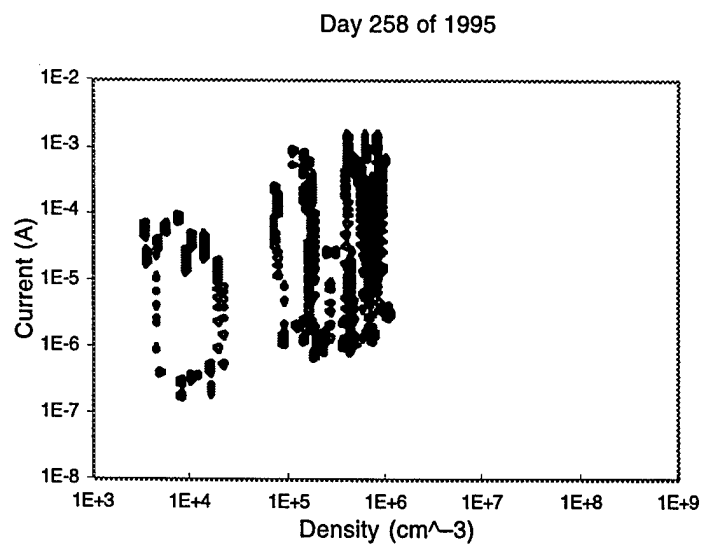
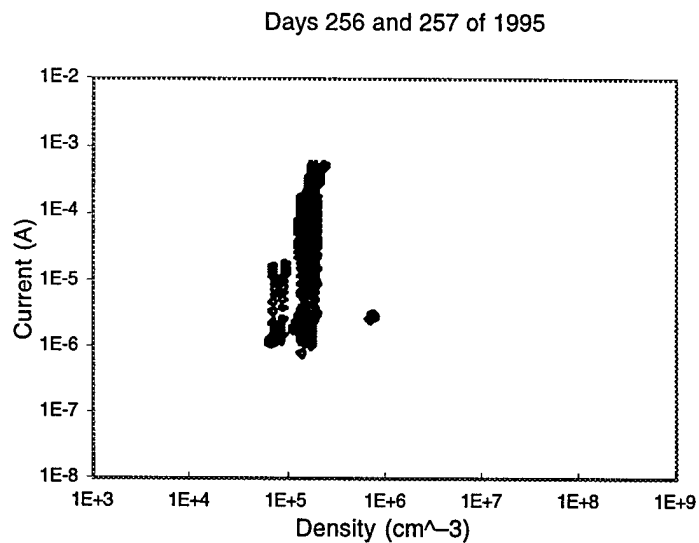
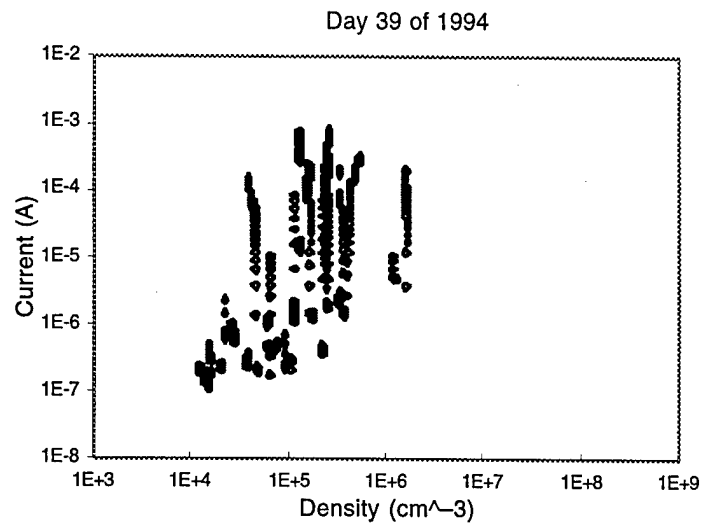


Figure 54. Collected current as a function of plasma density for high (over 40 V) potential measurements.

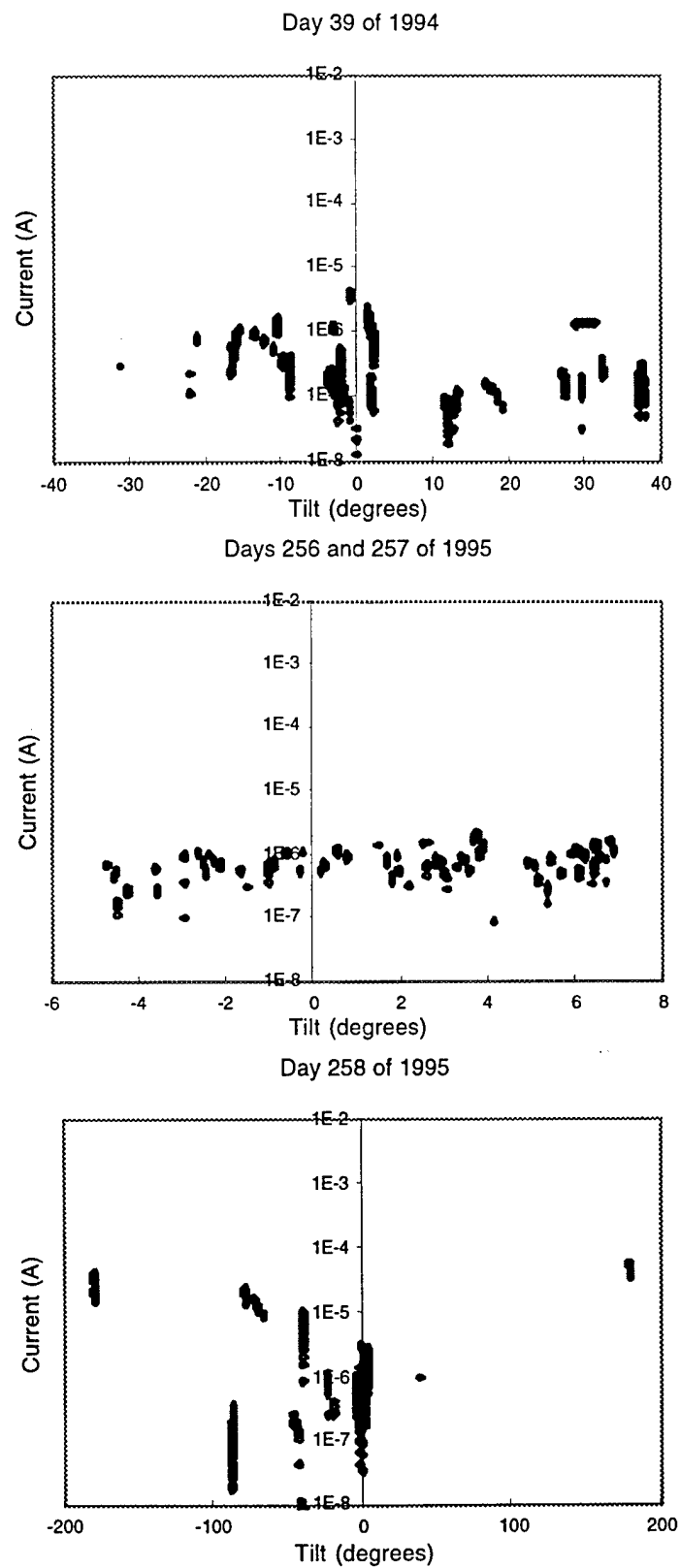


Figure 55. Collected current as a function of tilt for low (under 40 V) potential measurements. Note that the range of tilt values is different for each time period.

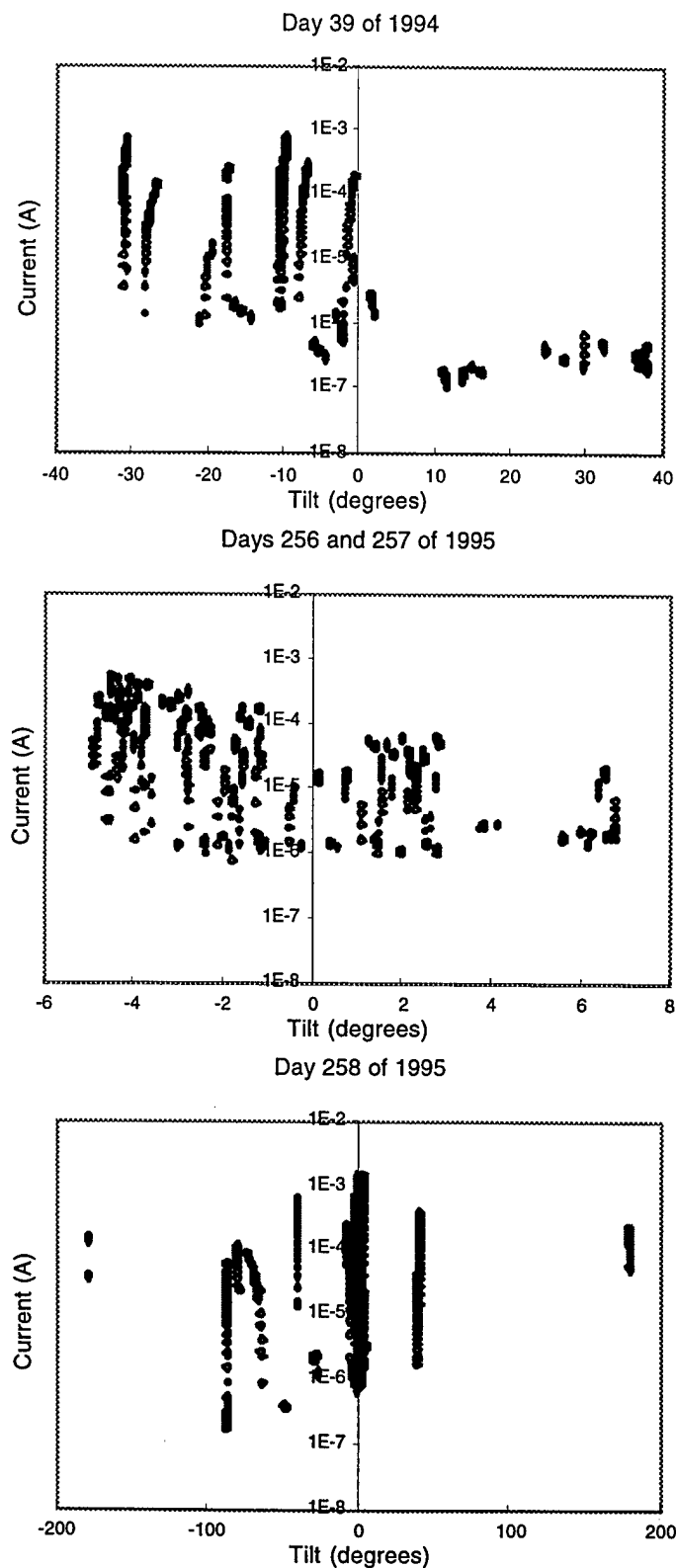


Figure 56. Collected current as a function of tilt for high (over 40 V) potential measurements. Note that the range of tilt values is different for each time period.

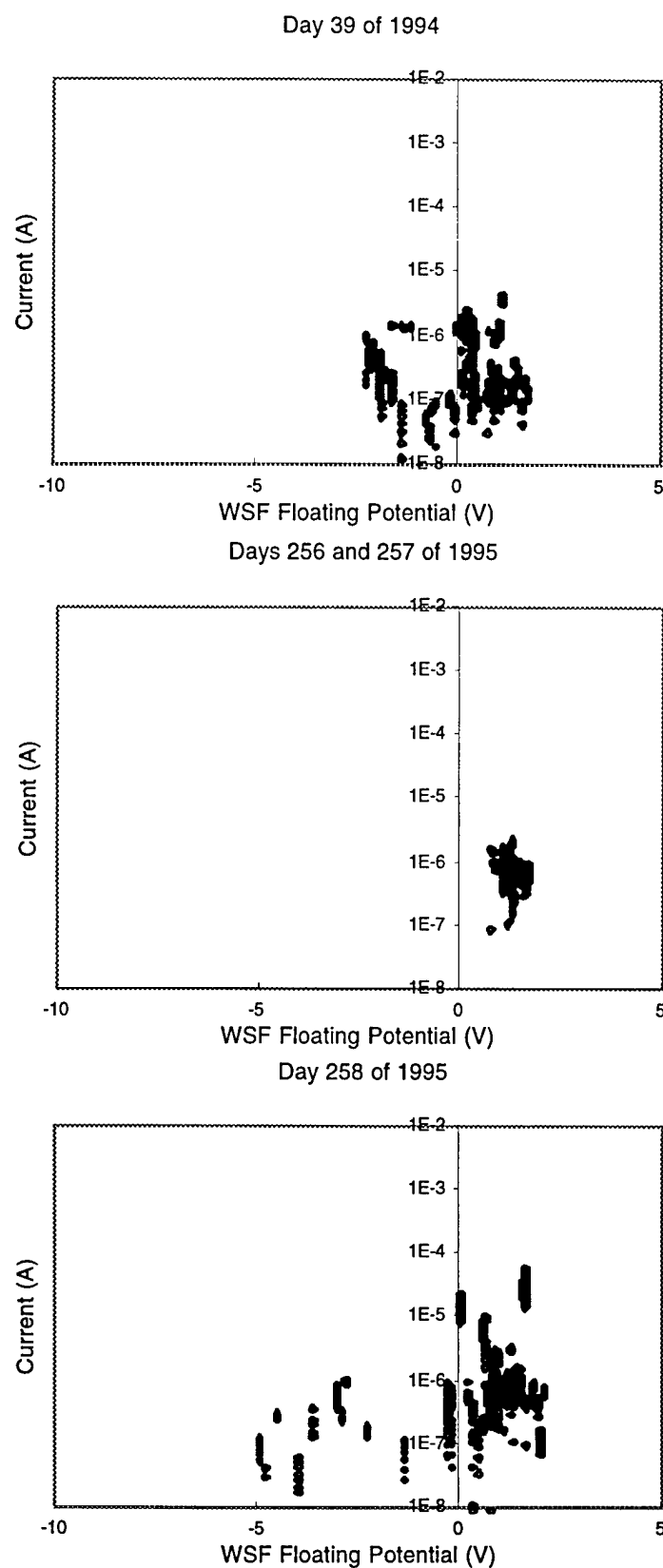


Figure 57. Collected current as a function of WSF floating potential for low (under 40 V) potential measurements.

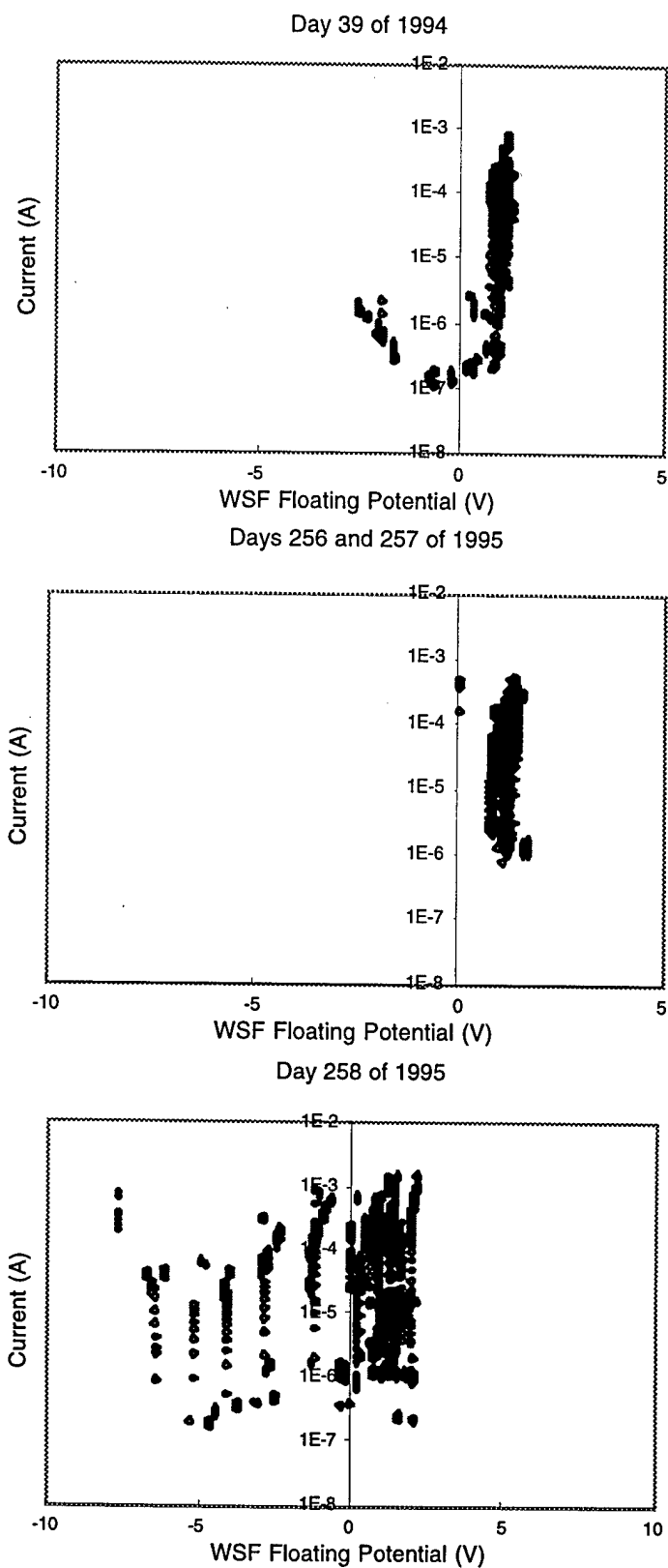


Figure 58. Collected current as a function of WSF floating potential for high (over 40 V) potential measurements.

A sunlit probe has more current than a dark one due to photoemission and the fact that plasma density is higher during the day. When the sun-disk angle is 90° , the sun is incident on the edge of the disk and the probe is fully illuminated. When the sun-disk angle is greater than 90° , the sun is illuminating the back of the disk. When the probe is fully illuminated the photocurrent appears to be approximately $1\ \mu\text{A}$. Since the distance from the probe to the edge of the disk is approximately equal to the length of the probe, the probe is entirely shadowed by the disk for a sun-disk angle of under 45° for any orientation. There is some angle between 45° and 90° at which just the tip of the probe is illuminated. This angle depends on the orbit and the disk orientation. It appears to be near 77° for the first flight and does not show clearly for the second flight. Figure 60 shows a model of the shuttle from the viewpoint of the sun as the tip of the probe comes into view. Between 77° and 90° , we approximate the photocurrent by linear interpolation between 0 and $1\ \mu\text{A}$.

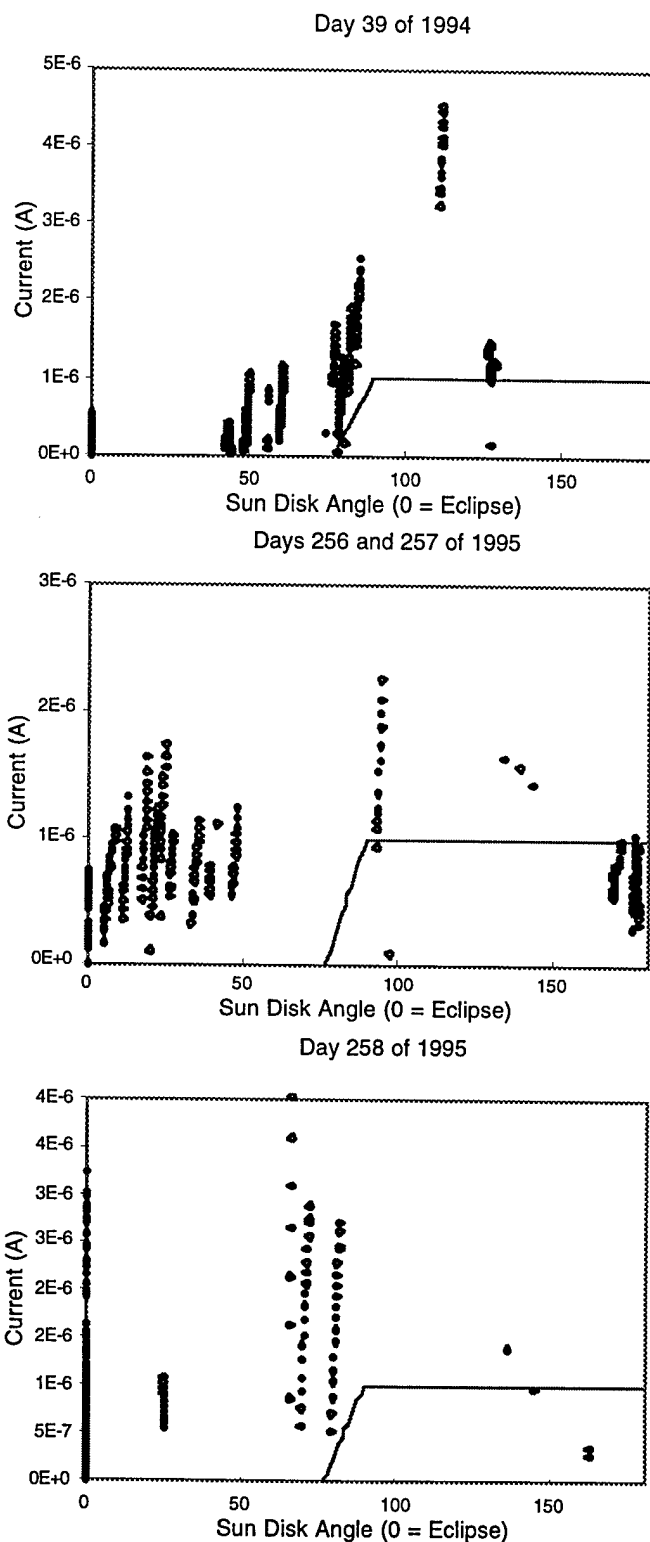


Figure 59. Collected current as a function of sun-disk angle for low potential (under 40 V) measurements. An angle of zero indicates eclipse. The solid line is the photocurrent estimate. There are measurements with even higher currents than shown during day 258.

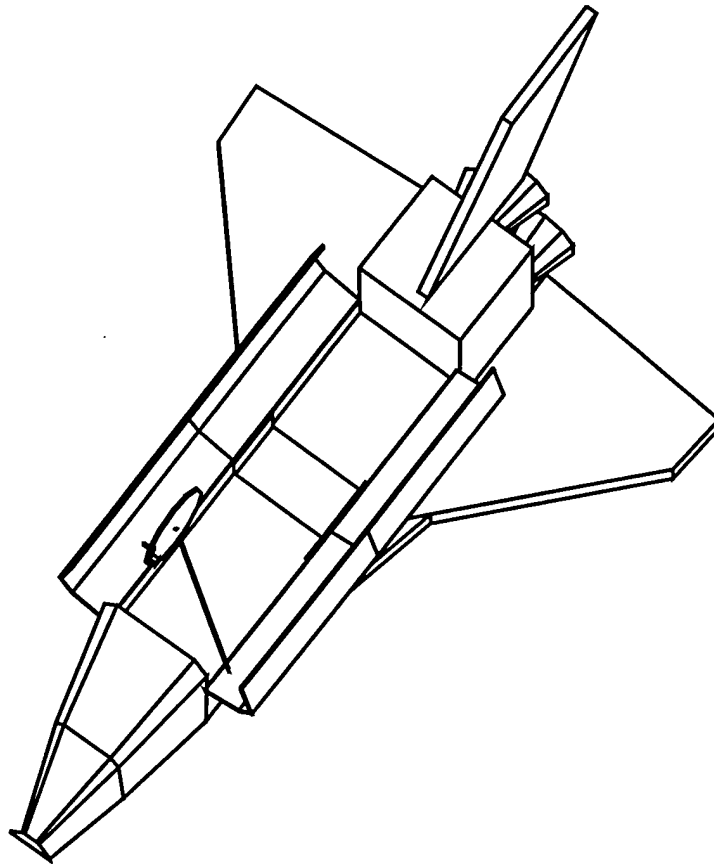


Figure 60. View of the shuttle and WSF from the point of view of the sun when the tip of the CHAWS probe comes into view.

The strong dependence on applied bias seen in Figure 52 suggests an examination of how current measurements vary for a few specific applied bias values might be useful. Figures 61 and 62 show how the current varies over times and with density for some specific bias values for the first flight. The highest current values occur with full sun. Figures 62 and 63 compare the CHAWS current with the atomic oxygen plasma thermal current to an unbiased probe for a plasma with the specified density and a 0.1 eV temperature for the first flight and during free flight. That this plasma thermal current is similar in magnitude to the measured current suggests that the density in the wake region is not significantly below the ambient plasma. That this occurs during free flight means that the shuttle environment is not entirely responsible for the wake density.

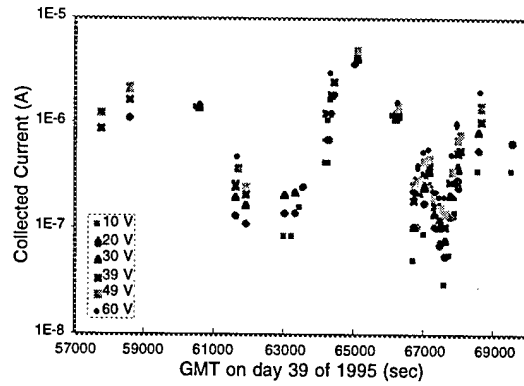


Figure 61. Collected current for specific applied bias values.

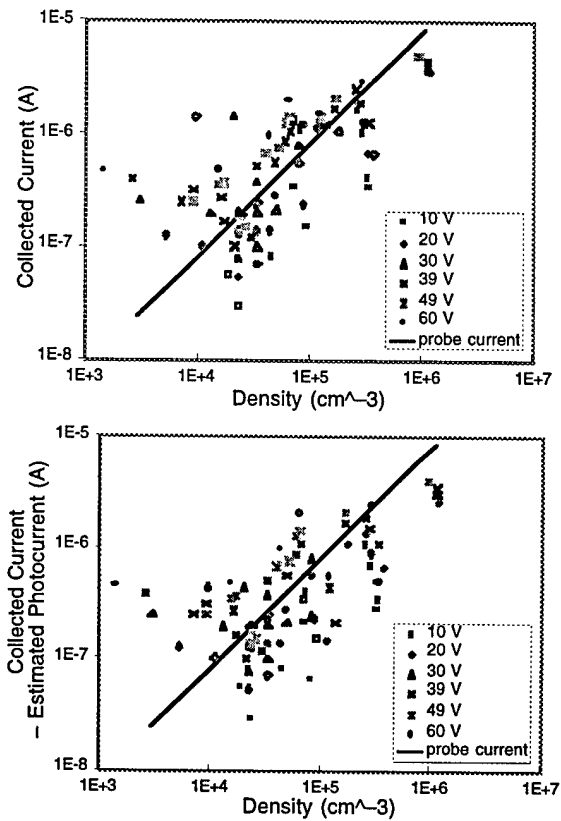


Figure 62. Collected current as a function of plasma density for a few specified bias values during the first mission. The measured current is compared with the atomic oxygen plasma thermal current to an unbiased probe for a plasma with the specified density and a 0.1 eV temperature. The bottom figure shows the same data points with the estimated photoemission subtracted.

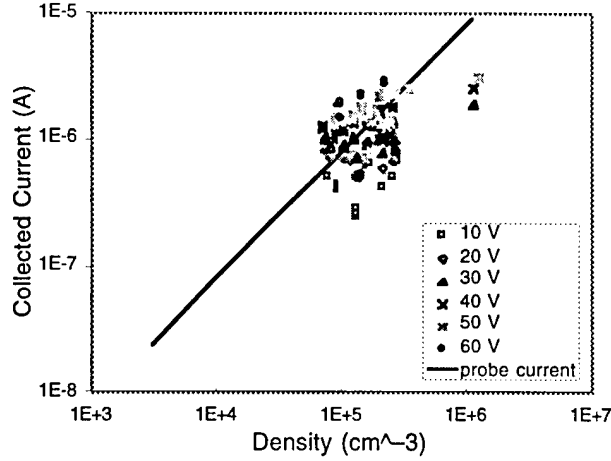


Figure 63. Collected current as a function of plasma density for a few specified bias values during free flight. The measured current is compared with the atomic oxygen plasma thermal current to an unbiased probe for a plasma with the specified density and a 0.1 eV temperature.

8.6 Fitting

The data was divided into three sets: low potential (10 V to 40 V), high potential (over 40 V), and large tilt (absolute value of tilt greater than 40°). The independent variables used are applied bias, density, tilt, WSF floating potential (WSF fp), and $g(\text{eclipse}, \text{sun-ram angle})$ where

$$g(\text{eclipse}, \theta_{\text{sr}}) = \begin{cases} 0, & \text{eclipse} = \text{true} \\ 0, & \theta_{\text{sr}} < 77 \\ (\theta_{\text{sr}} - 77)/13, & 77 > \theta_{\text{sr}} > 90 \\ 1, & \theta_{\text{sr}} > 90 \end{cases}$$

For the first flight and second flight day 258 data under 40 V, we did a least square linear fit to a function of the form

$$\ln(I - g(\text{eclipse}, \text{sun ram angle}) \cdot 1\mu\text{A}) = a + b \cdot \ln(\phi) + c \cdot \ln(n) + d \cdot \text{tilt} + e \cdot \text{WSF fp}$$

For the rest of the data we used

$$\ln(I) = a + b \cdot \ln(\phi) + c \cdot \ln(n) + d \cdot \text{tilt} + e \cdot \text{WSF fp}.$$

The terms can rearranged to write the current as

$$I = \exp(a) \phi^b n^c \exp(d \cdot \text{tilt}) \exp(e \cdot \text{WSF fp}) + g(\text{eclipse}, \text{sun ram angle}) \cdot 1\mu\text{A}.$$

This form was chosen because it accounts for photoemission, uses power laws to fit the primary variables, and varies slightly above and below the null values for variations in tilt and WSF fp. Also we know that

$$\exp(x) \approx 1 + x, \text{ for } x < 0.5$$

Table 9 shows the values of the coefficients for the fit of the high voltage data (over 40 V) when all the variables are used and when some coefficients are set to zero. Some points to be noted are as follows:

- (1) The voltage exponent is near 1.4, suggesting orbit-limited collection of whatever plasma is in the vicinity of the probe with an enhancement due to secondary emission.
- (2) The density exponent varies from 0.20 to 0.50. This could be due to accidental correlations or differences in the experiment. The lowest values are from the free flight period during which the variation in density was small, and therefore the fitting coefficient is less reliable.
- (3) The current shows no significant dependence on the disk potential.
- (4) The sign of the tilt dependence is consistent with an increased current when the probe is closer to the ram flow. The tilt change during free flight is so small that any dependence on this value is not physically relevant.
- (5) The coefficient of determination compares estimated and actual values and ranges from 0 to 1, where 1 indicates a perfect correlation. In these cases, the fit is good.

Table 9. Fit to Data over 40 V.

Parameter		Fit 1	Fit 2	Fit 3
Day 39 of 1994				
b	Potential	1.60 (0.02)	1.38 (0.02)	1.38 (0.01)
c	Density	0.50 (0.02)	0.50 (0.01)	0.49 (0.01)
d	Tilt	0	-0.026 (0.001)	-0.026 (0.001)
e	WSF fp	0	-0.01 (0.02)	0
η		0.961	0.985	0.985
Days 256 and 257 of 1995				
b	Potential	1.32 (0.01)	1.37 (0.01)	1.36 (0.01)
c	Density	0.25 (0.04)	0.20 (0.04)	0.22 (0.04)
d	Tilt	0	0.027 (0.005)	0.022 (0.005)
e	WSF fp	0	0.14 (0.06)	0
η		0.976	0.977	0.976
Day 258 of 1995				
b	Potential	1.44 (0.01)	1.44 (0.01)	1.45 (0.01)
c	Density	0.31 (0.02)	0.31 (0.02)	0.29 (0.02)
d	Tilt	0	-0.009 (0.001)	-0.009 (0.001)
e	WSF fp	0	-0.022 (0.004)	0
η		0.973	0.977	0.976
Attached (Day 39 of 1994 and Day 258 of 1995)				
b	Potential	1.50 (0.01)	1.465 (0.008)	1.469 (0.008)
c	Density	0.43 (0.01)	0.44 (0.01)	0.42 (0.01)
d	Tilt	0	-0.0175 (0.0007)	-0.0176 (0.0007)
e	WSF fp	0	-0.046 (0.009)	0
η		0.964	0.978	0.978

(η is the coefficient of determination.)

Table 10 shows similar fits to the low voltage data (10 V to 40 V):

- (1) The "coefficient of determination" is lower, indicating that other factors contribute significantly to the current.
- (2) The voltage exponent is near $6/7$, suggesting space-charge-limited collection of whatever plasma is in the vicinity of the probe. If the density in the wake is proportional to the ram density, this is consistent with the approximate square dependence seen on the ram density. The dependence on density is lower during the free fly period. As the density did not vary much during this period, the fitting coefficient is not accurate.
- (3) The tilt dependence appears to be much weaker than in the high voltage case. The inclusion of tilt does not improve the fit, except for the free flight period for which the coefficient is not reliable. The coefficient is always small and for the free flight period, the sign of the tilt dependence is consistent with an increased current when the probe is closer to the ram flow. Tilt is not a dominant variable, perhaps because the sheath remains entirely within the wake.
- (4) The dependence on WSF disk potential is larger than for the higher potential measurements. This indicates that the disk potential is more important at lower biases. The sign of the coefficient is such that when the disk is negative, the current increases.

Table 10. Fit to Data from 10 to 40 V.

Parameter	Fit 1	Fit 2	Fit 3	Fit 4
Day 39 of 1994				
b Potential	0.82 (0.08)	0.83 (0.07)	0.85 (0.08)	0.82 (0.07)
c Density	0.63 (0.03)	0.72 (0.02)	0.59 (0.03)	0.75 (0.02)
d Tilt	0	-0.004 (0.002)	-0.009 (0.002)	0
e WSF fp	0	-0.33 (0.02)	0	-0.33 (0.02)
η	0.627	0.756	0.646	0.751
Days 256 and 257 of 1995				
b Potential	0.74 (0.04)	0.72 (0.03)	0.74 (0.04)	0.71 (0.04)
c Density	0.15 (0.03)	0.21 (0.02)	0.15 (0.02)	0.23 (0.02)
d Tilt	0	0.032 (0.003)	0.040 (0.004)	0
e WSF fp	0	-0.53 (0.07)	0	-0.72 (0.07)
η	0.597	0.806	0.744	0.721
Day 258 of 1995				
b Potential	0.85 (0.08)	0.92 (0.07)	0.85 (0.08)	0.92 (0.07)
c Density	0.47 (0.04)	1.00 (0.07)	0.45 (0.05)	0.93 (0.06)
d Tilt	0	-0.011 (0.006)	0.005 (0.007)	0
e WSF fp	0	-0.40 (0.04)	0	-0.38 (0.04)
η	0.443	0.597	0.444	0.592
Attached (Day 39 of 1994 and Day 258 of 1995)				
b Potential	0.84 (0.06)	0.86 (0.05)	0.85 (0.06)	0.86 (0.05)
c Density	0.63 (0.02)	0.76 (0.02)	0.59 (0.02)	0.78 (0.02)
d Tilt	0	-0.004 (0.001)	-0.009 (0.002)	0
e WSF fp	0	-0.32 (0.02)	0	-0.33 (0.02)
η	0.687	0.787	0.700	0.785

(η is the coefficient of determination.)

8.7 Comparison with Calculation

For space charge limited collection and simple geometries

$$I \propto n \times \text{function} \left(\frac{\phi^{3/4}}{n^{1/2}} \right)$$

where function(x) varies from x^1 for one-dimensional systems to $x^{8/7}$ for three-dimensional systems. Orbit limited collection depends on density and potential as

$$I \propto n \phi$$

The signature of space charge limited collection in three dimensions is a density exponent of 3/7, which is close to the density dependence of the high voltage measurements. This is consistent with the preflight DynaPAC and POLAR calculations, which showed space charge to be important at high potentials, and that the current scaled approximately as three-dimensional space charge limited collection. The calculations showed a nearly linear voltage dependence at high potentials, above the 6/7 power expected for pure space charge limited collection. If we assume an approximate square root dependence of the secondary emission on the potential, the high potential flight measurements are consistent with the preflight calculations.

The preflight calculations with an oxygen plasma show a potential threshold. If 10 percent of the plasma is hydrogen, the threshold disappears. The size of the currents at low biases suggests that the shuttle plasma includes a large component of slow moving ions. The low potential measurements have potential and density dependencies in between space charge limited and orbit limited. Since the currents at the lowest bias values are below the theoretical plasma thermal current to the probe with no bias, the wake plasma must have a lower density than the ram plasma.

The preflight DynaPAC and POLAR calculations showed a threshold for ram oxygen collection at about 100 volts of negative bias. In the flight data, current was collected with only a few tens of volts. This might be due to either hydrogen or slow-moving spacecraft generated ions. Figure 62 shows that for the lowest (10 V) bias the collected current is consistently about one order of magnitude

below what would be collected by a stationary unbiased probe in the measured ambient plasma. Assuming orbit-limited collection, this implies a plasma density in the probe region about three orders of magnitude below ambient. Such a density is far higher than the theoretical values in a spacecraft wake, but may well be consistent with a plasma due to thrusters, outgassing, and other contamination sources.

8.8 Probe in Ram Measurements

Three sets of measurements were made with the wake side probe exposed to the ram flow on day 258 of 1995. We consider all measurements in which the absolute value of the tilt is above 40 degrees to be ram measurements. The measurements are shown in Figure 64. The first set were made at about 62300 s. The shuttle was rolled about its long axis with WSF above the bay and its edge toward the shuttle. During this period, the plasma density probably varied from about 10^5 to 10^6 cm^{-3} . The second set were made at about 33500 s. At this time the disk was at a tilt of 41 and 42 degrees. The plasma density was near 10^6 cm^{-3} . The third set were taken while the wake side of WSF was exposed directly to ram at the end of the measurement period. The IRI model gives a plasma density of about 2×10^5 for this period.

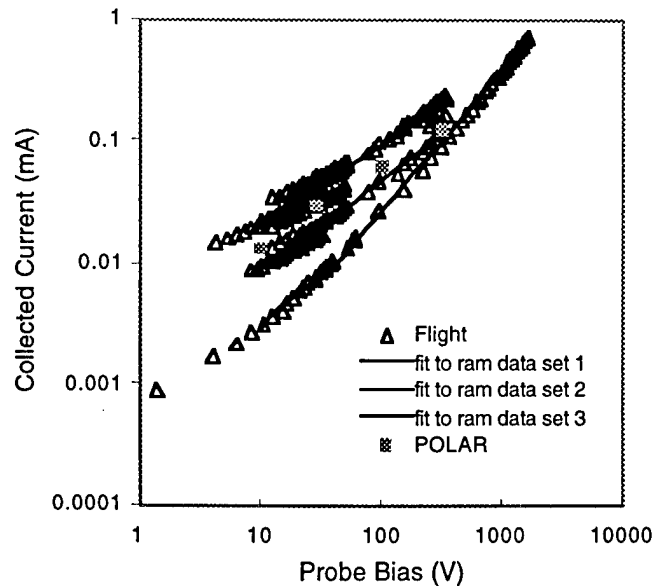


Figure 64. Current as a function of applied bias for measurements in which the absolute value of the tilt is above 40 degrees. (Probe in ram flow.)

If we fit the three sets of ram facing measurements to the function

$$I = a \phi^b$$

we get the coefficients shown in Table 11. The resulting curves are plotted in Figure 64.

Table 11. Fits to Ram Facing Data

	32300 s	33500 s	40500 s
a for $\phi < 40$ V	2.1×10^{-6}	0.37×10^{-6}	6.0×10^{-6}
b for $\phi < 40$ V	0.64	0.91	0.57
a for $\phi > 40$ V	1.5×10^{-6}	0.13×10^{-6}	3.9×10^{-6}
b for $\phi > 40$ V	0.75	1.1	0.69

Prior to the first flight of CHAWS, Dr. David Cooke of Phillips Laboratory used the POLAR code to compute the current collected by an isolated probe of the size and shape of the CHAWS probe in a 10^{11} m^{-3} , 0.1 eV, mach 7.1 atomic oxygen plasma. The results of these calculations are shown in Figure 64 for comparison. The calculations show a current of approximately the same magnitude, but a different slope than the flight results.

8.9. WSF in Shuttle Wake

A set of measurements were made while WSF was in the wake of the shuttle. For this time period IRI gives the plasma density as near 10^5 m^{-2} . These measurements are shown in Figure 65. The currents are lower than in any other measurements. Table 12 shows coefficients for a fit to these measurements using the same functional form as for the ram facing measurements. This fit is also plotted in Figure 65. We also did a single calculation at 2000 V using DynaPAC for a plasma density of 10^{10} m^{-3} and this geometry. The result of this calculation is also shown in Figure 65. The measured current is much higher than the calculated current indicating that the actual density in the shuttle wake is much higher than the calculated density. As both hydrogen and species originating at the shuttle are present this is not surprising.

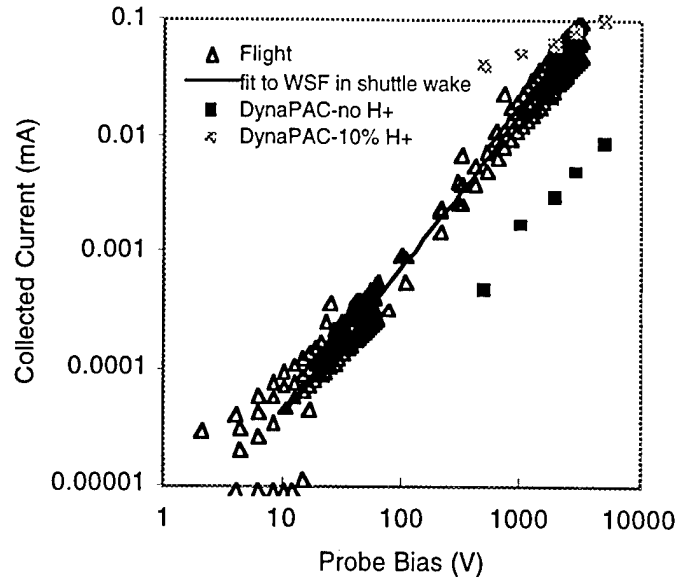


Figure 65. Current versus applied bias for WSF in shuttle wake.

Table 12. Fits to WSF in Shuttle Wake Data

a for $\phi < 40$ V	1.7×10^{-9}
b for $\phi < 40$ V	1.36
a for $\phi > 40$ V	1.70×10^{-9}
b for $\phi > 40$ V	1.33

8.10 Additional Material

The following describes how chunks, a couple of short specialized FORTRAN programs and EXCEL 5.0 can be used to create this report. It is assumed that the reader is fortran and unix literate.

Step 1 – Run Chunks

Documentation for chunks is available with the “official” version of this software. The following script and input files were used.

```
rm inputs
ln inputs.39early inputs
chunks > output.39early
mv output_CHA_current current.39early
rm inputs
ln inputs.39 inputs
chunks > output.39
mv output_CHA_current current.39
rm inputs
ln inputs.256 inputs
chunks > output.256
mv output_CHA_current current.256
rm inputs
ln inputs.257 inputs
chunks > output.257
mv output_CHA_current current.257
rm inputs
ln inputs.258 inputs
chunks > output.258
mv output_CHA_current current.258
```

Figure 66. Script used to run chunks.

start_date	39:03:30:00	day:hr:min:sec
stop_date	39:04:25:00	day:hr:min:sec
stdio_cas	1	stdio_switch
stdio_wsf	1	stdio_switch
stdio_chaws	1	stdio_switch
stdio_merge	1	stdio_switch
logical	0	on/off
output_CAS	0	on/off
output_CAS	1	GMT_ut
output_CAS	2	Orbiter.pitch
output_CAS	3	Orbiter.yaw
output_CAS	4	Orbiter.roll
output_CAS	5	latitude
output_CAS	6	longitude
output_CAS	7	sun_angle
output_WSF	0	on/off
output_WSF	1	ram_angle
output_WSF	2	xz_tilt
output_WSF	3	xy_wag
output_WSF	4	vxb_dot_L
output_WSF	5	solar_el
output_WSF	6	solar_az
output_CHA_frame	0	on/off
output_CHA_frame	1	ram_inboard_hpeng
output_CHA_frame	2	ram_center_hpeng
output_CHA_frame	3	ram_outboard_hpeng
output_CHA_frame	4	ram_inboard_temp
output_CHA_frame	5	ram_center_temp
output_CHA_frame	6	ram_outboard_temp
output_CHA_frame	7	ram_inboard_dens
output_CHA_frame	8	ram_center_dens
output_CHA_frame	9	ram_outboard_dens
output_CHA_frame	10	ram_inboard_fltpot
output_CHA_frame	11	ram_center_fltpot
output_CHA_frame	12	ram_outboard_fltpot
output_CHA_channel	0	on/off
output_CHA_current	1	on/off

Figure 67. Standard input for chunks execution.

start_date	39:15:55:00	day:hr:min:sec
stop_date	39:19:50:00	day:hr:min:sec
start_date	256:19:13:00	day:hr:min:sec
stop_date	256:20:10:00	day:hr:min:sec
start_date	257:06:27:00	day:hr:min:sec
stop_date	257:07:50:00	day:hr:min:sec
start_date	258:08:07:00	day:hr:min:sec
stop_date	258:11:20:00	day:hr:min:sec

Figure 68. Modified dates used for other chunks executions.

The stdio params control the print to standard output. The logical switch controls the column order of merged output. The output_CAS, output_WSF, and output_frame, output_CHA_channel commands control the generation of separate files of CAS, WSF, and single frame, and single channel data. The variables are GMT_ut, universal time in seconds constructed from the CAS data structure, Orbiter.pitch, Orbiter.yaw, Orbiter.roll (directly from the CAS data structure), latitude, longitude, (as computed by CHAPS), sun_angle, (negative value means eclipse) ram_angle, xz_tilt, xy_wag, vxb_dot_L, solar_el, solar_az, ram_*_hpeng, (the last energy at which the ram mcp distribution falls to 0.5 times the count for 0 V based on the summed contributions from the indicated detectors), ram_*_temp, (calibrated temperature for the ram side detectors using a mach number of 5), ram_*_dens (calibrated density for the ram side detectors using a mach value of 5), and ram_*_fltpot (WSF floating potential as computed from the half-point energy and the disk orientation).

The output_CHA_current controls the printing of the additional file output_CHA_current. It contains currents extracted from within a CHAWS 7.5 sec frame according to a fixed pattern. The pattern used is as follows. For step 1: volts is average of voltages 1 to 4; current is average of channels 60 to 68, for step 2: volts is average of voltages 5 to 6; current is average of channels 108 to 116, for step 3: voltage 7; current is average of channels 132 to 140, for step 4: voltage 8; current is average of channels 148 to 156. The contents are CHAWS time = day and total seconds (2 integers), langmuir voltage = lv or hv from stencil, depending on saturation (float), langmuir current = from stencil (float), langmuir sweep profile and status flag (2 integers), delta between stencil voltages (float), goodness flag: =1 if voltage > 2.5, =2 if also delta > 0.0 (integer), event and sweep

counters (2 integers). The event counter tries to flag "interesting" events. the event counter is incremented if there was a transition from goodness flag 0 to 2. It is printed until there is a departure from goodness = 2, then it shows 0. The sweep counter tries to flag good sweeps. Note that there are 4 steps per frame, and thus 4 goodness flags per frame. The sweep counter is incremented if there are more than 6 consecutive good ,where a good frame is one with 2 or more steps having goodness flags that are = 2

Step 2 – Filter Chunks Output

The standard output files from Chunks include lines indicating that WSF data is missing. As these lines are of no use to us (at least here and now) we use grep to eliminate them. We use a short fortran program called process to pick out the clean measurements (event counter has a nonzero value) from the i-v curves. The script used to do this and the program process follow. Then by hand we removed lines in the out* files at the beginning and end that correspond to times not represented in the ave* files. This is not necessary.

```
grep -v WSF output.39early > out.39early
process < current.39early > averaged.39early
grep -v WSF output.39 > out.39
process < current.39 > averaged.39
grep -v WSF output.256 > out.256
process < current.256 > averaged.256
grep -v WSF output.257 > out.257
process < current.257 > averaged.257
grep -v WSF output.258 > out.258
process < current.258 > averaged.258
```

Figure 69. Script used to prepare chunks output files for EXCEL.

```
print 1100
1100      format (' Time          Pot1          Current')
          do 20 i=1,400000
              read *, day,time,pot,cur,t1,t2,t3,t4,t5,t6
              if (pot.gt.1..and.cur.gt.5.87e-9.and.t6.gt.0)
                  & print 1200, time,pot,cur
1200      format (1x,g15.7,g13.5,lg12.4)
20        continue
999       continue
          stop
          end
```

Figure 70. Source code for program process.

Step 3 – Transfer files to EXCEL.

Once the files were transferred to EXCEL we examined the points for obviously incorrect measurements. The first point of a sweep often appeared to be incorrect. The first point was discarded if the product of the ratio of the second point current to the first point current and ratio of the first point potential to the second point potential was over four. We also discarded measurements with half-point energies of zero and tilt values with absolute value under 40 degrees.

9. References

1. M. J. Mandell, I. Katz, G. A. Jongeward, V. A. Davis, D. E. Parks, and D. L. Cooke, "Theoretical and Computer Modeling Support for SPEAR II," in *SPEAR II, High Power Space Insulation*, eds. H. A. Cohen and T. G. Engel, Texas Tech University Press, Lubock, Texas, 1995.
2. M. J. Mandell, T. T. Luu, J. R. Lilley, Jr., D. L. Cooke, "DynaPAC—A 3-D Finite Element Plasma Analysis Code," *Proceedings of the DNA Numerical Methods Symposium*, 1992.
3. M. J. Mandell, G. A. Jongeward, D. L. Cooke, W. J. Raitt, "Sheath Physics and Potential Mitigation on the SPEAR-III Rocket Experiment," AIAA Paper 94-0327, 1994.
4. V. A. Davis, B. M. Gardner, D. A. Guidice, P. S. Severance, "Parasitic Current Collection by PASP Plus Solar Arrays," in *Proceedings of the Fourteenth Space Photovoltaic Research and Technology Conference*, NASA Conference Publication 10180, p. 274, 1996.
5. V. A. Davis, B. M. Gardner, D. A. Guidice, "Modeling of Parasitic Current Collection by Solar Arrays in Low Earth Orbit," *Physics of Plasmas*, Vol. 3, No. 11, p. 4181, 1996.
6. V. A. Davis, B. M. Gardner, D. A. Guidice, "PASP Plus Solar Array Parasitic Current Collection Flight Results," in *Proceedings of the 31st Intersociety Energy Conversion Engineering Conference*, IEEE, Piscataway, New Jersey, p. 13, 1996.
7. M. J. Mandell, G. A. Jongeward, D. L. Cooke, W. J. Raitt, "SPEAR-3 Flight Analysis: (a) Grounding by Neutral Gas Release; (b) Magnetic Field Effects on Current Distribution", *Journal of Geophysical Research*, in press.
8. V. A. Davis, B. M. Gardner, D. A. Guidice, "PASP Plus Solar Array Parasitic Current Collection Flight Results", *IEEE Transactions on Plasma Science*, accepted for publication.
9. V. A. Davis, M. J. Mandell, D. C. Cooke, C. L. Enloe, "High-Voltage Interactions in Plasma Wakes: Simulation and Flight Measurements from the Charging Hazards and Wake Studies Experiment", to be submitted to the *Journal of Geophysical Research*.